University of Alberta

Nanolithography on H:Si(100)-(2 x 1) using combined Scanning
Tunneling and Field Ion Microscopy techniques

by

Cristian Vesa

A thesis submitted to the Faculty of Graduate Studies and Research
in partial fulfillment of the requirements for the degree of

Master of Science

Department of Physics

©Cristian Vesa
Fall 2011
Edmonton, Alberta

domnului profesor Branco Arsenov

Acknowledgements

I would like to express my gratitude to all those who have generously helped and supported me throughout my graduate studies and without whom this thesis would not have been possible.

I am very grateful to my supervisor, Prof. Robert Wolkow, for the support, patient guidance, and advice he has provided throughout my time as a Master's student and for giving me the opportunity to participate in an exciting and challenging scientific endeavor.

In addition to making my time as a graduate student very enjoyable, past and present members of the Molecular Scale Devices Group have also lent me a great deal of help throughout the years: they have patiently shared their time, knowledge and insights with me and have also offered thoughtful advice and encouragement on countless occasions. I would like to extend my thanks to all of them: Martin Cloutier, Dr. Gino DiLabio, Dr. Stanislav Dogel, Peter Legg, Dr. Lucian Livadaru, Josh Mutus, Dr. Jason Pitters, Dr. Paul Piva, Dr. Peter Ryan, Mark Salomons, Shoma Sinha, Marco Taucer, Dr. Radovan Urban, Dr. Janik Zikovsky.

Last but not least, I wish to also thank my family and friends for their kind words and unwavering support.

Abstract

This thesis reports on the combined techniques of ultra-high vacuum scanning tunneling microscopy (UHV-STM) and field ion microscopy (FIM). The apex structure of STM scanning tips correlates with their ability to yield highly-resolved images and to perform accurate hydrogen desorption on hydrogen terminated silicon, H:Si(100)-(2 × 1). The FIM permits not only tip apex characterization but also in vacuo tip reshaping by field evaporation and nitrogen etching. STM nanolithographic techniques are employed to perform hydrogen removal and thus create assemblies of dangling bonds. The thesis provides an overview of the mechanisms underlying hydrogen removal in various regimes and also calculations to estimate tip-induced field effects. The capabilities of the apparatus are explored and techniques are established to be pursued further for optimization. These techniques have the potential of advancing the production of novel computing architectures based on silicon atomic quantum cellular automata (SiAQCA). Such devices constitute promising, low energy-consuming alternatives to transistor-based architectures.

Contents

List of Figures

List of Tables

Chapter 1

Introduction

This thesis presents the apparatus, techniques and theoretical considerations required for nanostructure fabrication on hydrogen-terminated silicon. Specifically, the focus is on the lithographic techniques aimed at hydrogen resist removal from H:Si(100)-(2 × 1) in order to create configurations of uncapped silicon atoms with unsaturated bonds known as dangling bonds. Such configurations constitute silicon atomic quantum cellular automata (SiAQCA) and could serve as building blocks for revolutionary computing architectures.

Research avenues such as the one outlined above are actively pursued within the context of the current miniaturization trend in electronic devices. It is inevitable that this trend will proceed into the nano-scale: molecules exhibiting specific functions could be synthesized and manipulated with a scanning tip in order to create single-molecule devices and the capabilities of semiconductor surfaces could be enhanced by functionalization with organic molecules in order to achieve light detection or chemical sensing, for instance. [16]

However, another important consideration would be that despite the steady pace of microelectronics development, the industry will eventually face insurmountable obstacles when technological and fundamental limits are reached. The most pressing problem is power consumption per unit area. Unlike transistor-based architectures, novel technologies such as quantum cellular automata (discussed below) represent promising low power consuming architectures. Other important technological issues would be the interconnect problem, arising from the fact that interconnections would not scale in concert with the devices, and power dissipation, which becomes less efficient with decreasing feature size and the attendant increase in device density. But apart from that, if scaling down continues conventional technology will ultimately fail when quantum effects such as charge quantization become sizable enough to become disruptive to their operation. [17]

An alternate computational nanoelectronic achitecture wherein information is contained in the arrangement of charges and not in the flow of charges, has been proposed. [1] The

building blocks for such a scheme would be quantum dots arranged in cells interconnected to form cellular-automata-like arrays. The charge configuration of a quantum-dot cell would encode binary information. Assuming potential barriers high enough to preclude tunneling out of a cell, information would be transmitted from one cell to the next via classical cell-cell interactions such as Coulomb-coupling. Such a paradigm would require energy separations significantly above $k_B T$ and phase coherence only inside individual cells.

Although there are considerable hurdles to implementing such a computational paradigm
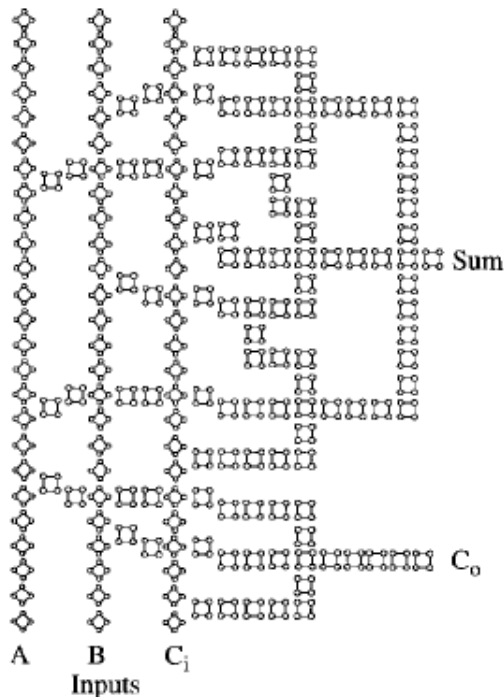
Figure 1.1: Implementation of logic gates using binary wires made up of four-site QCA cells. [1]

candidates for potential building blocks have been proposed. Semiconductor quantum dots operating at cryogenic temperatures in order to ensure the requisite wide energy spacings have been suggested as a basis for quantum cellular automata schemes. In 2009 tunnel-coupled silicon atom dangling bonds on a hydrogen-terminated Si(100) - 2 × 1 surface were reported. [2] They can serve as quantum dots by virtue of the fact that their energy levels reside within the bandgap of silicon which makes them electronically decoupled from the bulk states. Assemblies of them constitute very promising candidates for quantum cellular automata schemes chiefly because the charging and tunnel-coupling behavior can be controlled at room temperature. Another considerable advantage resides in the use of the Si(100) - 2 × 1 reconstruction, which is characterized by high structural and electronic uniformity. Also, this reconstruction is unaffected by hydrogen passivation and is the surface of choice for silicon integrated circuit fabrication which would thus allow for integration of

novel nanotechnologies with existing platforms. Hydrogen passivated silicon surfaces are inert and the removal of surface states as hydrogen atoms cap dangling bonds to form a monolayer of hydrogen resist, allows for the observation of subtle electronic effects. [18]

The silicon atomic quantum dot cell reported in 2009 comprised six dangling bonds of which four disposed in a rectangular arrangement were tunnel-coupled while the diagonally located remaining two acted as Coulombic perturbers breaking the symmetry of the charge distribution and thus creating an antipodal state.
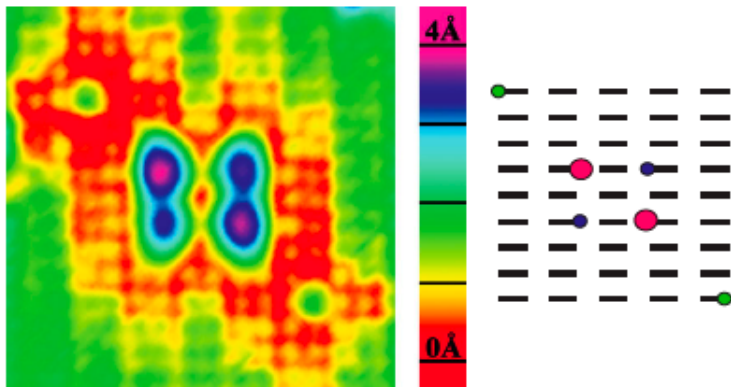
Figure 1.2: A color-mapped STM image of a rectangular 4-dangling-bond entity with 2 diagonally-placed electrostatically perturbing dangling bonds. [2]

To create the constituent dangling bonds of the above-mentioned assemblies an ultra-high vacuum (UHV) scanning tunneling microscope (STM) equipped with a field ion microscope (FIM) is employed. The FIM allows the characterization of the scanning tip apex structure, which represents a great advantage as the scanning probe's ability to yield highly resolved STM images and to perform accurate hydrogen desorption depends upon its structure. In addition to tip inspection, FIM also affords the possibility to reshape tips in vacuo within the FIM by means of field evaporation and nitrogen etching. Such tips can thereafter be transferred to the STM with virtually no further contamination.

The development of the scanning tunneling microscopy technique originated in the early 1980s. Over the decades, not only have STMs become very powerful surface analysis instruments, but they have also evolved the capability of manipulating matter at the atomic level, which renders them suitable for pursuing the highly-controlled fabrication of nanostructures required for the creation of SiAQCA.

In STM, a very sharp tip scanned over the sample under investigation senses the atomic corrugations in the surface electron distribution arising from the arrangement of surface

3

atoms. This is achieved by applying a voltage bias to the sample and bringing the tip into tunneling contact with it such that a current is established. The minute tunneling current established between the tip and the surface is very sensitive to their separation and since variations in the tunneling current correspond to variations in the surface electron density, current measurements collected over an area of the sample yield a two-dimensional topographic map of the surface. STM has enabled scientist to obtain atomically-resolved images of various surfaces, which led to a more in-depth understanding of surface reconstructions as well as the physical and chemical interactions between adsorbed atoms or molecules and substrates.

Among others, the structures of the Si(111) and Si(100) surface reconstructions were finally elucidated by using scanning tunneling microscopy. In the latter case such studies confirmed the dimer-based (dimers arise when pairs of adjacent atoms on a bulk-terminated silicon surface form a bond as the surface relaxes to lower its energy) model and also showed that the dimer itself was a bistable asymmetric species, with one atom of the dimer located higher than the other. [16, 19–21]

Dangling bond creation is achieved by applying either a voltage or current pulse to the surface under investigation. [22] While the hydrogen desorption mechanism has not been fully elucidated two different desorption regimes have been clearly identified: the high (above 5V) and low voltage regimes. [23] In the former desorption yield is dependent on electron dose, while in the latter desorption occurs only at high current and is independent of dose. The latter occurs while the tip is in tunneling with the surface and therefore affords enhanced patterning resolution. While in this regime patterning can be sporadic it is the preferred one for highly controlled hydrogen abstraction. Considerable effort still needs to be expended before reliable high yield patterning techniques are developed.

Successful dangling bond creation and thus patterning is heavily dependent on the characteristics of the scanning tip. This is why the fabrication of reliable and reproducible scanning tips is highly desirable. Control over the tip apex structure could offer a way to improve the ability of the tip to perform accurate hydrogen desorption as specific characteristics may prove to be better suited for hydrogen removal.

The primary purpose and outcome of the current study was to establish the apparatus and techniques to pursue controlled atom scale modifications, that is nanopatterning of hydrogen resist on H:Si(100)-(2×1). While initial attempts have been performed, these have served largely to check the capabilities of the instrument, a UHV STM system equipped with an FIM. Further excercising of the approach described here will be the subject of subsequent further study by others. If a reliable technique for accurately creating dangling bond assemblies were developed it would have a significant impact on the production QCA-

based devices.

Chapter 2

Scanning Tunneling Microscopy

2.1 Historical Overview

During the night of March 16th, 1981 using the scanning tunneling microscope (STM) they had developed over the past few years at IBM Zurich, Gerd Binnig and Heinrich Röhrer obtained the first unambiguous exponential dependence of the tunnel current on an externally and reproducibly adjustable vacuum gap (tip-sample separation) characteristic for tunneling. [24] After having adjusted the piezosensitivity calibration the data yielded a tunneling barrier of more than 4 eV in agreement with the expected barrier height of 5 eV. Months earlier they had obtained their first STM images showing sharp monatomic steps and thus they had finally confirmed the creation of a scanning microscope whose functioning principle was based on vacuum tunneling. [25]

Binnig and Röhrer had embarked on this project with a view to performing spectroscopy locally on areas less than 100 Å in diameter, not of developing a microscope. They had in mind the investigation of the electrical properties of thin insulating layers, specifically the inhomogeneities of thin oxide layers grown on metal surfaces. It was upon realizing that the tool for probing such properties did not exist that the thought of making use of vacuum tunneling resurfaced in Binnigs mind. Tunneling spectroscopy had been pioneered in the 1960s by Ivar Giaever who demonstrated the tunnel effect through a very thin oxide layer surrounded on both sides by metal in a normal or superconducting state. However, vacuum tunneling had not been attempted until later, in the mid-1970s by W. A. Thompson. [26] He developed a technique for bringing two electrodes to within 10 to 20 Å of each other by means of a thermal drive apparatus in order to perform direct tunneling experiments.

Upon more consideration Binnig and Röhrer also realized that the tool they had decided to develop would function as a microscope as well. In addition to performing local spectroscopic measurements it would also have the capability to collect spectroscopic and topographic images of the areas it would scan. In the latter respect this new technique would be akin to stylus profilometry yet unlike it, the scanning probe would not be in

contact with but would hover a few Ångstroms above the surface controlled by the tunnel current established between surface and probe. The instrument most deserving of being recognized as the precursor of the STM is the topografiner, the first successful scanning probe microscope. [27] It was invented by Russel Young in the early 1970s and it employs the phenomenon of field emission for acquiring microtopographic images of surfaces. The scanning tip of the topografiner could be brought to within 250 microns of a conducting specimen and when the voltage applied between them was high enough electrons would tunnel from the metal tip through the work-function barrier into nearby vacuum states and thus impinge upon the sample. The emission current is governed by the Fowler-Nordheim equation and is maintained constant by feedback control of the vertical position of the tip. Young did not attempt to operate the topografiner in metal-vacuum-metal tunneling mode (the form of tunneling employed in STMs) despite being aware of its advantages, because of vibrational noise and instability in the feedback electronics. It therefore fell well short of atomic resolution with an estimated lateral resolution of 400 nm.

Binnig and Röhrer first achieved atomically-resolved images with their new instrument for measurements on Au(110) when their attempts at resolving surface reconstructions came to fruition. On Au(110) they observed ribbons of the 1×2, 1×3, 1×4 reconstructions as well as step lines. Subsequently they performed their first spectroscopic measurements on gold and also chemical imaging of Au islands on silicon, which imaged as smooth, flat hills on a rough topography. In 1982, having honed their technique in previous experiments, they were able to acquire images of the Si(111)-(7×7) reconstruction which confirmed the adatom model (save the aspect relating to the number of adatoms) proposed by W. Harrison. In collaboration with other researchers they proceeded to do scanning tunneling spectroscopic measurements on silicon and gold.

These successes sparked theoretical research into the field of STM and the technique itself gained wider acceptance within the scientific community with a considerable number of groups worldwide adopting this powerful technique. For the design of the scanning tunneling microscope Binnig and Röhrer were awarded the Physics Nobel Prize in 1986.

2.2   The Scanning Tunneling Microscope *

Since the invention of the scanning tunneling microscope the scanning probe microscopy technique has known a rapid and sustained growth. The STM and other scanning probe microscopes have enabled us to probe the world at the nanoscale by allowing us to investigate the physical, chemical and electronic properties of surfaces and adsorbates. In addition to surface characterization they have also allowed us to manipulate atoms and molecules by means of lithographic processes or mechanical forces, depending on the tip-sample interac-

---

*Based on references: [3, 28, 29].

tion utilized.

The essential elements of any scanning probe micoscope are: the vibration isolation system, the coarse approach and the fine positioning systems, the interaction sensing and feedback control systems, and data acquisition and display.

In an STM the scanning tip is attached to a piezodrive usually consisting of three mutually orthogonal piezoelectric transducers, the x, y, and z piezos. Applying voltages to the piezos generates their motion. Scanning in the xy plane is achieved by applying a sawtooth waveform on the x piezo and a voltage ramp on the y piezo. As the range of motion for the piezos is limited to a few microns the coarse positioning mechanism is responsible for bringing the tip within a few microns of the sample without crashing it. As soon as the tip and sample are within a fraction of a nanometer of each other a finite tunneling conductance arises between them and upon applying a voltage bias to the sample a tunneling current is established.

Typically, the tip is a ground potential, as established through connection to the input of a current-to-voltage amplifier while the sample is voltage-biased in positive and negative polarities. It is at times convenient to reverse this connection scheme, connecting the sample to the amplifier and biasing the tip. In the most common connection scheme, if the bias voltage is positive, electrons tunnel from the occupied states in the tip into the empty states of the sample, while if it is negative, electrons tunnel from the occupied states in the sample into the empty states of the tip.

A current amplifier converts the tunneling current into a voltage and the feedback control extends or withdraws the tip so that the equilibrium position is established and thus the setpoint tunneling current maintained. A topographic image of the scanned sample area is thus generated by displaying a two-dimensional array of equilibrium z positions. In a grayscale image the bright features correspond to high z values while the dark ones to low z values. Usually the image is accompanied by a scale bar for more precise data presentation.

2.2.1   The Vibration Isolation System [†]

Early on in their endeavor to create the first STM, Binnig and Röhrer realized the chief importance of protecting their instrument against mechanical vibrations and acoustical noise in order to be able to achieve atomic resolution. It is noteworthy that the tip-sample gap needs to be maintained constant to within 1 picometer as greater deviations result in a 2 per cent error in the current reading. [29]

[†]Based on reference: [28].

The physics of vibration isolation in STM can be illustrated in analogy with a one-dimensional vibrating system composed of a mass connected to a frame by a spring and a viscous damper. The frame represents the floor and the mass the STM. The aim is to obtain the proper parameter values so as to minimize the vibration transferred from the frame to the mass. In this case it is useful to consider the dependence of the transfer or response function on the natural frequency of the system and the damping constant. The transfer function gives the ratio of the amplitude of the mass to that of the frame as a function of the excitation frequencies of the frame resulting from environmental vibrations:

$$K(\omega) = \left| \frac{x_0}{X_0} \right| = \sqrt{\frac{\omega_0^2 + 4\gamma^2\omega^2}{(\omega_0^2 - \omega^2)^2 + 4\gamma^2\omega^2}},$$

where ω_0 is the natural circular frequency and γ the damping constant. The smaller the value of the transfer function the better the isolation system performs.

At high frequencies the transfer function is inversely proportional to the excitation frequency, $K(\omega) \propto \omega^{-2}$, unless the damping constant is high in which case the dependence changes so as to significantly reduce vibration isolation, $K(\omega) \propto \omega^{-1}$.

If the excitation frequency is close to the natural frequency (resonance regime) the transfer function depends mostly on the ratio of the natural frequency to the damping constant, $K(\omega) \approx \omega_0/2\gamma$.

Consequently the damping constant must be chosen so as to appropriately balance the considerations above that is, suppressing both resonance and high-frequency vibrations.

In the laboratory setting vibration isolation may ideally be achieved by constructing a separate concrete foundation for the entire instrument. Most frequently however, a basement level laboratory with relatively low floor vibrations would ensure appropriate vibration isolation.

The STM base plate is vibrationally-isolated by a suspension spring system coupled with an eddy current damper. As most of the mechanical vibration originating in the laboratory are found between 1 to 100 H10.1063/1.92999z the lower the natural frequency of the springs the more effective the isolation is. Moreover, the natural frequency of the springs depends solely on the stretch of the springs due to the mass of the STM base plate:

$$f_0 = 2\pi\sqrt{\frac{g}{\Delta L}}.$$

The eddy current damping occurs when a conductive material is subjected to a varying magnetic flux. As the copper plates attached to the STM base plate oscillate with respect

to strong permanent magnets (secured to the frame) interposed half-way between them the time-varying magnetic flux induces eddy currents in the copper plates, which in turn generate a magnetic field of opposite polarity and with it damping forces.

Another way to extend the analogy above is to identify the mass on the spring with the STM scanner and the base plate with the frame. In this case it is advantageous for the scanner assembly to be rigid and thus have a high resonance frequency. The relative tip-sample motion is negligible for excitation frequencies, f, lower than the natural frequency of the scanner assembly as the ratio of amplitude difference to the amplitude of the base plate is $\propto (f/f_0)^2$.

In conclusion, the overall transfer function is given by:

$$K(f) = \left(\frac{f_I}{f_S} \right)^2,$$

where f_S denotes the natural frequency of the scanner and f_I the one of the vibrational isolation system. Therefore $f_I/f_S \approx 10^3$ ensures a good vibrational isolation for the system.

2.2.2   The Coarse Approach System

There are several coarse sample approach mechanisms each suited for the requirements of various microscope designs. Three of the most commonly used categories of coarse sample positioning techniques are [3]:

1. A walker which uses electrostatic, mechanical or magnetic clamping and is actuated by piezoelectric elements that expand or contract upon voltage application;

2. A differential screw micrometer pushing on a reduction lever which can be driven either manually or by a stepping motor;

3. A lead screw pushing against a differential spring.

The first type is best suited for vacuum chamber STMs and into this category fall the louse and the inchworm as well.

The louse was successfully used in the first STM designed by Binnig and Röhrer. It consists of a piezoplate equipped with the sample holder on top, standing on three metal feet separated by high-dielectric-constant insulators from three metal ground plates. The feet are clamped to the ground plates by applying a voltage. The louse can move in any direction in steps of 10 nm to 1 micron by alternatively activating the clamping voltage and the voltage on the piezoplate which elongates and contracts the body of the louse.

The inchworm developed by Burleigh Instruments is a piezoelectric linear walker. It consists of a shaft, having the scanning tip mounted at one end, resting closely inside a ceramic piezoelectric tube. The tube comprises three piezo sections: the middle one expands or contracts longitudinally depending on the voltage applied to it while the end ones act as clamps by contracting radially when a voltage is applied to them. The following sequence generates the motion of the inchworm:

1. end section 1 grips the shaft;

2. middle section extends;

3. end section 3 grips the shaft;

4. end section 1 unclamps the shaft;

5. middle section contracts;

6. end section 1 grips the shaft;

7. end section 3 unclamps the shaft.

The Omicron STM-1 employs a linear stepper drive as a coarse positioning device for the sample. However, unlike the inchworm, it uses slip/stick effects related to inertia forces when a piezo is driven in a fast/slow sequence. It is based on the design of Niedermann et al [30] and similar to the micropositioning device of Shih et al. [31] The slip/stick technique allows coarse movements along the x direction parallel to the sample surface, and along the z direction perpendicular to the sample surface for tip approach/retraction. The x and z sliders of the walker are located one above the other such that the tracks are orthogonal to each other thus eliminating undesired rotations. Both sliders of the walker slide on sapphire balls in tracks consisting of a groove containing two adjacent piezoelectric tubes and one rectangular-shaped groove. When the piezo tubes are polarized longitudinally they experience shear deformation and as a result the sliders undergo horizontal displacements. Transport of the sample is accomplished by applying a sawtooth voltage. Stepwise translation occurs as follows: when the voltage slope is low the slider sticks to the piezos via magnetic coupling, thus moving with them, and when the voltage slope is high the slider keeps its position by slipping due to its inertia. Single or multiple continuous steps can be made by applying single or continuous sawtooth cycles. The amplitude of the sawtooth voltage determines the size of the step while the frequency, the speed of translation.

2.2.3 The Piezoelectric Scanner [‡]

The heart of the STM is the piezoelectric scanner as this is the component that rasters the probe across the sample on subnanometer length scales while also controlling the tip-sample

---

[‡]Based on references: [3, 28].
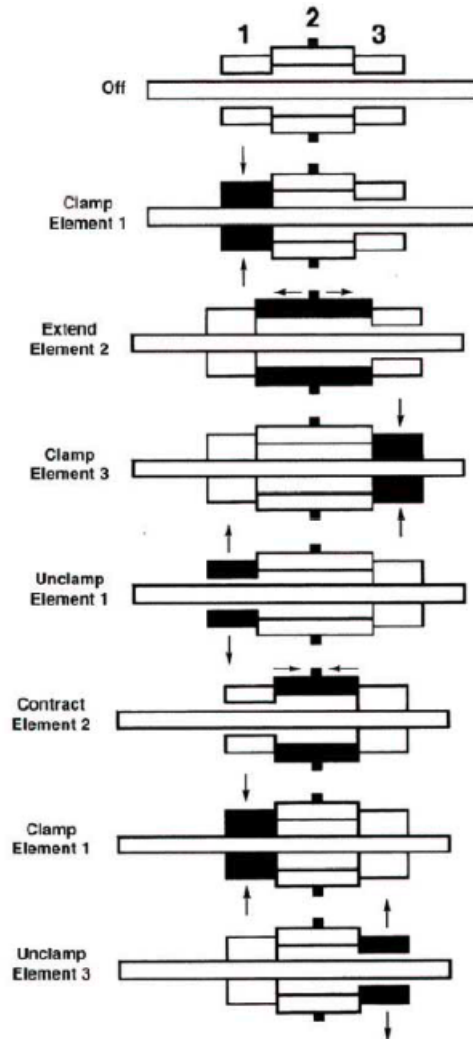
Figure 2.1: Diagram illustrating the sequence of applied voltages that generates the motion of the inchworm. (Image taken from a brochure on Inchworm Motor Technology of EXFO Burleigh Products Group.)

separation. It is made of piezoelectric materials, the frictionless link between electronics and mechanics.

A piezoelectric substance produces an electric field when stress is applied and conversely, a mechanical deformation occurs when an electric field is applied. The latter effect was predicted by Lippmann and is known as the reverse piezoelectric effect. This is the underlying working principle of STM scanners.

The piezoelectric materials used in STM are lead zirconate titanate ceramics (PZT). Ceramics are preferred over single-crystals as the former can be readily shaped and polarized along the desired axis. PZT ceramics are obtained from a mixture of $PbZrO_3$ and

$PbTiO_3$ and small amounts of additives. Firing this mixture produces a solid solution that is macroscopically isotropic because of the random orientation of the individual crystal dipoles. Finally applying a high electric field for the required length of time produces a permanent electrical polarization thus rendering the material macroscopically anisotropic along the desired direction. PZT ceramics retain their piezoelectricity up to temperatures in the range from 200° to 400° C. However over time microscopic relaxation occurs and the piezoelectricity declines. The efficiency of energy conversion between mechanical and electrical forms is higher for PZTs than it is for quartz, the model piezoelectric material, and therefore they exhibit piezoelectric constants 1 to 2 orders of magnitude higher than quartz (-2.25 pm/V).

The predominant types of scanners in use nowadays are the tripod and the tube scanner.

The tripod scanner is the earliest scanner design and also the one Omicron STM-1 machines are equipped with. The motion in the x, y, z directions is actuated by three independent orthogonal metallized PZT transducers.

The tube scanner, a later design, invented by Binnig and Smith in 1986 is fabricated from a single piezoelectric tube. It is simpler in design than the tripod scanner and has higher piezo constant and resonant frequency. In order to obtain full three-dimensional range of motion the electrode coating the dielectric is split longitudinally into four equal areas. Motion in the xy plane is achieved by controlling the voltages on two adjacent electrodes and the other two may be used as amplitude offsets. In the z direction a voltage applied to the inner electrode controls the overall axial deformation. There is a slight coupling between the x, y and z motions.

While for small and slow signals the relevant parameters are just the piezoelectric constants, at high frequencies the dynamic response of the piezo becomes considerable. Therefore the lowest resonant frequency constitutes the limiting factor of the scanning speed.

2.2.4 Tunneling

The operation principle of the STM is based on the quantum mechanical phenomenon of tunneling. Tunneling is the hallmark phenomenon of quantum mechanics. It has been applied to explain α decay in nuclear physics, the field-ionization of the hydrogen atom in atomic physics, field emission and the tunnel junction in condensed-matter physics.

Unlike in classical mechanics, in quantum mechanics it is impossible to simultaneously determine the spatial coordinates and the momentum components of a particle as required

by the Heisenberg uncertainty principle. A complex wavefunction, $\psi(z)$, is associated with the system in order to fully describe it. The wavefunction yields the probability density for position or momentum of the system under consideration. Therefore, a particle impinging upon a potential barrier of finite width has a non-zero probability of penetrating the barrier and tunneling through even if the total particle energy is less than the barrier height. In order to gain a basic understanding of metal-vacuum-metal tunneling it is instructive to consider the one-dimensional case of an electron of energy E in a piecewise-constant potential $U(z)$. The wavefunction describing the electron obeys the Schrödinger equation,

$$-\frac{\hbar^2}{2m}\frac{\mathrm{d}\psi(z)}{\mathrm{d}x} + U(z)\psi(z) = E\psi(z).$$

In the classically allowed region, where $E < U$, the electron travels with constant momentum $p = \hbar k$, and the solution takes the form:

$$\psi(z) = \psi(0)e^{\pm ikz},$$

where

$$k = \frac{\sqrt{2m(E-U)}}{\hbar}$$

is the wavevector.

In the classically forbidden region the wavefunction describing an electron penetrating the barrier decays exponentially:

$$\psi(z) = \psi(0)e^{-\kappa z},$$

where

$$\kappa = \frac{\sqrt{2m(U-E)}}{\hbar}$$

is the decay constant.

The probability density of finding the electron in the barrier region is thus non-zero and proportional to $|\psi(0)|^2 e^{-2\kappa z}$. As tunneling is bidirectional the electron can tunnel through the barrier in the opposite direction in which case the solution exhibits a positive exponential dependence.

Having established the exponential decay of the wavefunction in vacuum we proceed to the case of an electron tunneling from a metallic tip into a metal. Both the metal and the tip are supposed to have the same work function ϕ. Adopting the vacuum level as the reference level for energy, and neglecting thermal excitation, we have the Fermi level energy, $E_F = -\phi$. Applying a bias voltage V, such that $eV \ll \phi$, to the tip lowers the Fermi level of the tip with respect to the Fermi level of the metal by eV and electrons occupying sample states with energies in the range $E_F - eV$ to E_F tunnel across the vacuum. The transmission
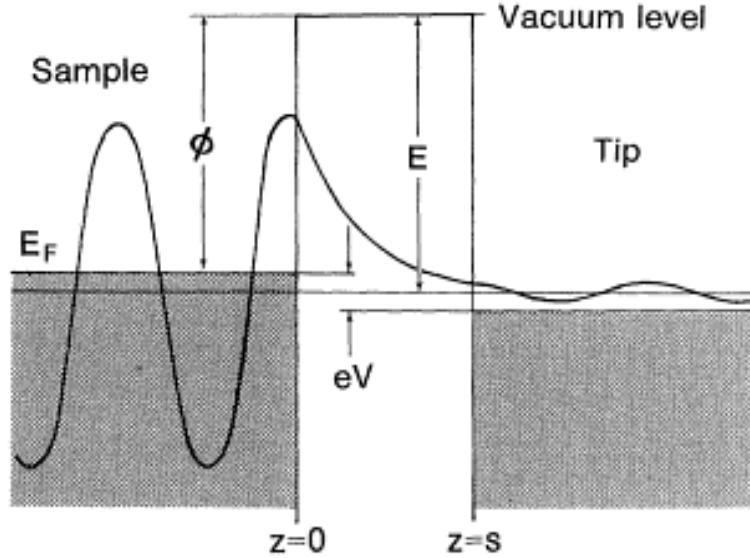
Figure 2.2: A one-dimensional metal-vacuum-metal tunnel junction. [3]

coefficient T is defined to be the ratio of the tunneling current at the tip surface, $z = s$, to the current incident on the barrier at $z = 0$.

$$T \equiv \frac{I(s)}{I(0)} = e^{-2\kappa s},$$

where

$$\kappa = \frac{\sqrt{2m\phi}}{\hbar}$$

is the decay constant. ϕ is used in the expression above as the electrons originate in the vicinity of the Fermi level. Substituting $\phi \approx 5$ eV, a typical value for the work function of metals used in STM, yields a decay constant value of about 11.4 nm^{-1} which is to say that the current decays roughly 10 times per 1 Å.

It is precisely the exponential dependence of the transmission coefficient on the vacuum gap width that allows atomic resolution in STM. The extreme sensitivity of the tunnel current on the barrier width selects the apical protrusion reaching closest to the sample to the exclusion of tunneling channels through minitips that may exist in the apex region. [3] High lateral resolution is thus expected even for moderately sharp tips. Additionally, the exponential dependence also ensures a strong signal for atomic scale control of the tip-sample separation in the z direction, as the tunneling current is exponentially sensitive to changes in z.

While the square-barrier tunneling problem offers an insight into the the working principle of the STM there is only a limited number of potential barriers for which the Schrödinger equation has analytic solutions. The semiclassical approximation is often used to deal with

general barriers. Moreover such approaches cannot provide a relationship between the absolute value of the tunneling conductance and the absolute tip-sample distance. Another aspect to consider is that an absolute tip-sample separation defined as the distance between the nucleus of the tip apical atom and the one of the nearest sample atom is difficult to determine experimentally. Experimentally only a relative, equilibrium tip-sample distance, z_e, can be determined, which approximately corresponds to the internuclear separation of a molecule made up of the topmost tip atom and the nearest sample atom. z_e has been determined with combined STM and AFM techniques to have an average value of 0.25 nm. [28]

Based on the assumptions that electrodes can be described by a one-dimensional square potential well and that the tunneling current is ballistic, Landauer developed a theory about the absolute tunneling conductance and predicted its quantization. The formula he found for the tunneling conductance G, for low bias voltages such that the electron density per energy unit varies negligibly within eV is:

$$G = \frac{2e^2}{h}T \equiv G_0 T,$$

where T is the transmission coefficient and G_0, the conductance quantum, is defined to be $\frac{2e^2}{h}$. Subsequent experiments using nearly free-electron metal electrodes confirmed the existence of a conductance quantum of about 77.48 μS in accordance with the formula.

A general expression for the vacuum gap conductance as a function of the tip-sample separation can be derived:

$$G = G_0 e^{-2\kappa(z-z_e)}.$$

2.2.5   Scanning Modes [§]

STM comprises several methods among which: constant-current or topographic mode, constant-height mode, and scanning tunneling spectroscopy (STS).

In constant-current mode at each measurement point the scanner height is adjusted by the feedback control such that the tunneling current remain constant. In order to ensure adequate response by the STM scanner it is desirable to set the feedback loop gain as high as possible without driving the system into oscillation, which may cause repeated tip crashes. When the system detects variations in current due to features (protrusions, depressions, or defects) on the sample surface it adjusts the voltage applied to the z piezo so the tunneling current setpoint can be re-established. The image maps the motion of the scanner along the z axis over the area scanned. These images almost never reflect the true height but rather the tip-sample separation as well as the spatial variation of the local density of states (LDOS). For rough surfaces this mode is preferred in order to avoid tip-sample collisions

---

[§]Based on references: [3, 29].

that could blunt the tip. A slight disadvantage of this mode would be that measurements require more time to acquire than in constant-height mode.

In constant-height mode the feedback loop is turned off and the tip scans the xy plane above the sample while remaining stationary in the z direction. The current varies with the topography (changes in the tip-sample separation) and the local surface electronic properties of the sample. An image arises as a data set consisting of the tunneling current variations across the plane of the surface sample. This mode is preferred when investigating atomically flat surfaces since rapid scanning is possible in the absence of feedback control.

In STS the feedback loop is interrupted and the bias voltage is ramped with the tip positioned over the feature of interest while recording the tunneling current. A current vs voltage (I-V) curve characteristic of the local electronic structure (LDOS) is obtained. Such spectra can be collected at every point within an area to map its electronic structure. They do not provide direct information on the sample density of states (DOS), but rather a convolution of the tip and sample DOS. However, to a good approximation, the LDOS is proportional to $\frac{\mathrm{d}I}{\mathrm{d}V}$ when the tip is far from the substrate and the tip DOS is reasonably smooth. Therefore it is desirable to employ tips whose DOS is not strongly dependent on the energy levels, ideally tips with a flat DOS that exhibit free-electron-metal behavior. However, sharp tips yielding atomically-resolved images have DOS that are highly structured, which is attributed to the fact that electrons tunnel from the localized states of the apex atom rather than from the Fermi sea into vacuum.

2.2.6   Bardeen Theory [¶]

In STM, the theory most widely employed for tunneling is Bardeen's first-order perturbation theory. Within this theory the tunneling current is viewed as arising from numerous independent tunneling events that transfer electrons across the barrier. Arriving at the expression for the total tunneling current requires an adequate evaluation of tip and sample wavefunctions. The underlying assumptions of Bardeen theory are:

A1 tunneling is weak enough that the first-order approximation is valid;

A2 tip and sample states are nearly orthogonal;

A3 the electron-electron interaction is negligible (single-electron charging effects cannot be accounted for);

A4 occupation probabilities for the tip and sample are independent of each other, and do not change, despite the tunneling;

[¶]Based on references: [28, 32, 33].

A5 the tip and sample are in electrochemical equilibrium.

In order to estimate the current through the tip-sample tunnel junction two separate subsystems are considered: the tip and sample. Their Hamiltonians are:

$$H_s\psi(r) = -\frac{\hbar^2}{2m}\Delta\psi(r) + V_s(r)\psi(r)$$

$$H_t\chi(r) = -\frac{\hbar^2}{2m}\Delta\chi(r) + V_t(r)\chi(r),$$

where $\psi(r)$, $\chi(r)$ are the eigenfunctions of the sample and tip, respectively, and V_s, V_t the potentials of each electrode.

A barrier surface within the junction divides it into the sample region and the tip region. $V_s(r) = V(r)$ inside the sample region and is zero elsewhere, while $V_t(r) = V(r)$ inside the tip region and is zero elsewhere. In a small area in the vicinity of the tip apex the potential barrier is considerably lowered. In accordance with assumptions **A4** and **A5**, the tip and the sample are considered to be large systems equipped with large electron reservoirs.

Employing first order perturbation theory and making use of **A2** in the limit of low bias voltages one arrives at the following expression for the tunneling current:

$$I = \frac{2\pi e^2}{\hbar}|M_{\mu\nu}|^2\rho_s(E_F)\rho_t(E_F)V,$$

where $M_{\mu\nu}$, the matrix element is $\frac{\hbar^2}{2m}\int_{barrier}\left[\psi_\mu\frac{\partial\chi_\nu^*}{\partial z} - \chi_\nu^*\frac{\partial\psi_\mu}{\partial z}\right]dxdy$ and $\rho_s(E_F)$, $\rho_t(E_F)$ are the sample and tip DOS at the Fermi level.

At low temperatures the occupation statistics of electrons in both electrodes are those of Fermi-Dirac equilibrium at temperature τ and chemical potential μ, and are given by the Fermi-Dirac distribution, $f_{\mu,\tau}(E) = \left[1 + e^{(E-\mu)/(k_B\tau)}\right]^{-1}$.

The tunneling matrix has dimensions of energy and it represents the interaction energy due to the overlap of two unperturbed states. The fact that the formula for the tunneling matrix is symmetric with respect to tip and sample wavefunctions forms the basis for the reciprocity principle in STM. The principle states that the image remains invariant under the interchange of tip and sample states, that is, whether we probe the sample with a tip state or vice versa. The most commonly used method to compute the tunneling matrix elements is by expansion of the tip wavefunctions in the gap region into their spherical-harmonic components.

2.2.7 STM Imaging [‖]

The data necessary to form a topographic STM image is typically acquired with a 512×512 grid so, mathematically, the images are matrices. The variables x and y are discrete and the size of the step in the xy plane sets the lateral resolution of the scanner, that is, the size of the grid and the magnitude of the area under investigation determine the lateral resolution limit for the image.

The resolution of the STM spans about four orders of magnitude from a fraction of a micron to a fraction of an Ångstrom. There are two imaging mechanisms at play: one governing the higher range and the other the lower one. On the nanometer scale the mechanism is much simpler and is well described by the Tersoff-Hamann model. However, this model does have considerable limitations as it fails to account for effects encountered in atomic-scale images and erroneously predicted that the corrugations of atomic-scale features would be on the order of a picometer.

A complication inherent in interpreting STM images, more pronounced in atomic-scale images, resides in the fact that the imaging mechanism is always a convolution of the tip and sample energy states, and the tip electronic states are challenging to compute exactly. Tersoff and Hamann realized that an ideal STM would measure an intrinsic property of the unperturbed surface rather than a joint property of the tip-sample system. Such a tip could be modeled as a geometrical point, that is a tip whose potential and wavefunctions were arbitrarily localized. The model is predicated on the central assumption that the tip wavefunction is spherically symmetric with respect to its center curvature.

This approach yields:

$$G \equiv \frac{I}{V} \propto \rho_s(E_F, r_0),$$

where G is the tunneling conductance and $\rho_s(E_F, r_0)$ is the LDOS at the Fermi level, E_F, at the center of curvature of the tip, r_0. The expression above states that all tip wavefunctions except for the s-wave can be neglected, as the conductance G is solely dependent upon the LDOS of the unperturbed sample. Within this framework the images are interpreted to be contour maps of the constant Fermi level LDOS of the bare surface. While this model has been shown to be accurate for single-atom tips by Lang, [35] and is likely adequate for small clusters of atoms too, the effect of the wavefunctions with non-zero azimuthal quantum number l does become important when:

$$a = \frac{\pi}{|\mathbf{q}|} \gg \frac{\pi}{\kappa} \approx 0.3\,\mathrm{nm},$$

where $|\mathbf{q}|$ is the Fourier component of the feature size a of the sample, and κ, the decay constant. This is because the contribution of higher angular momentum wavefunctions

---

[‖] Based on references: [28, 32, 34].

($l > 0$, $m = 0$) can be approximated by using a modified tunneling matrix obtained by taking z-derivatives of the solution $\chi(r)$ to the tip Schrödinger equation in the vacuum region:

$$-\frac{\hbar^2}{2m}\Delta\chi(\mathbf{r}) = -\phi\chi(\mathbf{r}),$$

where ϕ is the work function.

This introduces a factor modifying the tunneling matrix as follows:

$$\left(1 + \frac{\mathbf{q}^2}{\kappa^2}\right)^{l/2} M,$$

where M is the tunneling matrix, $\mathbf{q}$ and κ, the reciprocal space primitive vector and the decay constant, respectively.

In addition to imaging surface reconstructions, the Tersoff-Hamann model is also amenable to the interpretation of surface states (standing or scattered waves formed at step edges or local structures), and images of heterogeneous surfaces. Surface states can be modeled provided that their amplitudes at the solid surface are large. For flat surfaces and free-electron metals such states would not meet this criterion. In the case of heterogeneous surfaces, substitutional atoms and adsorbates create disturbances in their vicinity much greater in extent than single atoms which renders the tunneling currents from $m \neq 0$ tip states small. Imaging at the atomic scale is heavily dependent upon the tip electronic state probing the surface. In this mode corrugation amplitudes from 5 pm to 50 pm are routinely achieved for a variety of materials (from soft to hard metals, rare-earth metals, doped semiconductors) and on all crystallographic orientations. Evidence in support of the hypothesis that tip-state effects are responsible for obtaining atomically-resolved images consists in spontaneous changes (on the order of less than one millisecond) in image quality and contrast (corrugation amplitude and polarity). For instance, a commonly observed effect attesting to spontaneous tip restructuring and thus tip state switching is corrugation inversion, that is, atomic sites formerly imaging as protrusions appearing as depressions. Zhang et al [36] reported the observation of three different images of the same Ag/Si(111)-$\sqrt{3} \times \sqrt{3}$ sample surface corresponding to different tip states.

As the corrugation amplitude decays exponentially with tip-sample separation it is also essential that the tip be within about 0.2 nm of mechanical contact. However corrugation amplitude ceases to increase exponentially after the onset of the interaction between tip and surface states.

In the case of silicon investigations it has been found empirically that the highest resolution can often be achieved after prolonged periods of scanning and gentle controlled tip

crashes in order that silicon become adsorbed to the tip apex. The tentative explanation Demuth et al [37] put forward to explain the improved imaging ability of the tip subsequent to a controlled crash was that the adsorbed silicon cluster terminated in an apical sp^3 dangling bond better suited for observing the corrugation than an s-wave state. The earliest conjecture regarding favorable tip electronic states dates back to 1984 and attributes the high corrugation observed on Si(111)-7 × 7 to the existence of the d_{z^2} state at the apex of a tungsten tip.

The phase of the tip orbitals has been found to play a role in imaging. In the case of the spherically symmetric s-wave tip state the wave-nodes are located radially for $n > 0$ and therefore phase changes cannot occur. p states exhibit lobes of different polarities and therefore the tunneling amplitude is related to the derivative with respect to the axial direction of the sample wavefunction. For a d_{z^2}, state the tunneling matrix elements are a function of the second derivative of the sample wavefunction with respect to z. Thus, tips states other than s-waves amplifies the corrugations by being more sensitive to the variations in the sample wavefunction.
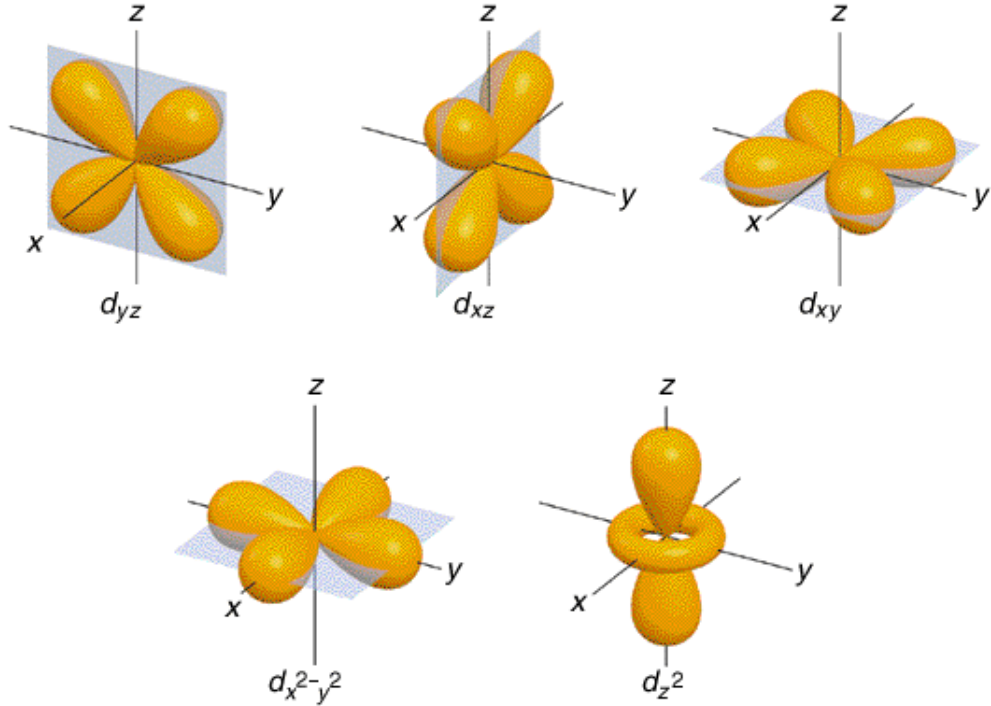
Figure 2.3: Images of d atomic orbital shapes. [4]

Corrugation inversion can also be explained in light of the considerations above. $l = 2$, $m = 1$ (d_{xy} and d_{yz}) and $m = 2$ ($d_{x^2-y^2}$ and d_{zy}) tip states, unlike $l = 2$ $m = 0$ and s

states, exhibit a ring-shaped LDOS. For a surface made of atoms with only s-wave states near the Fermi level the tunneling current is the tip-state LDOS measured at the sample atom. A d_{z^2} state having a sharp peak at the atom site would image the atom as a protrusion, whereas a ring-shaped state would image it as a depression due to the decreased tip LDOS of such a tip centered on a sample atom. Moreover, $m = 1$ states are more effective in generating inverted corrugation than $m = 2$ states because of their much sharper rim.

In conclusion, first principles numerical studies on transition metal tips have shown that d states dominate the tip DOS at the Fermi level, with s states constituting a few percent of the DOS and p states about 10%. p and d (d_{z^2}, sp^3) states protrude most into the vacuum, thus interacting most strongly with the sample surface. The latter states are responsible for enhancements of up more than one order of magnitude in the tunneling conductance corrugation.

Chapter 3

Silicon

3.1 Introduction

Silicon (Si) is the second most abundant element in the Earth's crust, after oxygen, and the most widely used material in semiconductor devices. Following the invention of the transistor in 1947, silicon and germanium semiconductor materials as well as the technological processes involved in their production developed at a steady pace driven by the desire of engineers to build smaller, ever more advanced circuits. While the first point-contact transistor consisted of a germanium crystal placed on a metal plate, germanium only remained the preferred semiconducting material during the 1950s whereafter it was supplanted by the more abundant silicon. Therefore, it is not surprising that the most significant advances in the semiconductor industry are linked to silicon. [38] The silicon crystal plane that constitutes the foundation for the silicon microelectronics industry is the one designated by the (100) Miller indeces, that is, Si(100).

At the same time as the semiconductor industry was taking off, Schlier and Farnsworth embarked on the first atomic-level studies of silicon and germanium. The surface structure characterization technique they employed was low-energy electron diffraction (LEED). This technique relies on the interpretation of electron diffraction patterns from the topmost few atomic layers of the crystal and furnishes information on the long-range atomic order on a crystal surface. However, LEED cannot reveal nanometer scale short-range crystalline order. [39, 40] Schlier and Farnsworth managed nevertheless to correctly infer the dimer model for the Si(100) surface reconstruction based on their observation of the (2×1) LEED pattern. [41] The existence of the dimers has been unequivocally established by STM images showing the atomic arrangement of the Si(100) surface reconstruction. [42]

3.2 Bulk versus Surface

Like the other semiconductors in group IV silicon also exhibits covalent bonds with a strong directional character. In bulk it crystallizes into the diamond structure, that is, the atoms are sp^3 hybridized. Each atom is bonded to its four nearest neighbors at tetrahedral angles of 109° 28′. In hybridizing the distribution of outer electrons for a silicon atom changes from [Ne]-$3s^2 3p^2$ to the NsNp^3 configuration. [43] Thus, two electrons of opposite spin reside between two bonded atoms. The energy released in bond formation more than compensates for the energy of promoting one s electron to the p orbital. The covalent bond length is 2.35 Å and its strength 226 kJ/mol (about 2.3 eV). [6] In order to analyze the molecular model of silicon bonds, a bulk crystal can be viewed as consisting of diatomic silicon molecules with bonding and anti-bonding orbitals.

Two types of bonds can form between silicon atoms. σ-bonds result from the overlap of a pair of sp^3 orbitals along the direction of the bond. In this case atoms are free to rotate about the axis of the bond. π-bonds result from the overlap of p-orbitals whose axes are perpendicular to the bonds. While considerably weaker than σ-bonds, π-bonds are rigid, that is, they resist rotation about the bond axis. Atoms sharing two pairs of electrons form both σ- and π-bonds, known as double bonds. [43]

When the crystal is cut or cleaved unsaturated bonds, i.e. dangling bonds (DB), are created at the surface, their orientation and density being dependent on the resultant crystal surfaces. Various surface reconstructions of silicon arise when rebonding occurs at the surface in order to reduce the surface energy. In addition to this, atomic relaxations also occur as the coordination number of surface atoms changes and atoms move away from the equilibrium positions they would occupy in the bulk. This results in bond length and bond angle changes. [44] The elastic strain surface atoms experience is roughly two orders of magnitude smaller then the bond energy so only minute deviations from the bulk structure take place. In view of the energetics involved in surface reconstructions, such reconstructions can be categorized as either activated or activationless. The activated ones have energetic barriers ($\Delta E > kT$) that must be overcome in order to obtain them, while the activationless ones have no or small barriers ($\Delta E < kT$). [43]

The surface reconstruction of element, E, is designated by E(hkl)-($m \times n$), where (hkl) refers to the crystal plane and m, n are the ratios of the unit surface vectors to the corresponding unit vectors of the substrate.

3.3 Si(100)

Si(100) has the simplest reconstruction of all the other silicon surfaces and is therefore, the most commonly used substrate for silicon devices. Rows of dimers arise as pairs of surface atoms come together to form dimers in order to lower the surface energy. Each surface atom bonds with its neighbor along the [110] direction thus halving the surface density of unsaturated bonds with one dangling bond per atom remaining. Two of the four degenerate dangling bonds overlap so as to give rise to a bonding configuration with a lower energy σ-level, and an anti-bonding one with a higher energy σ^*-level. π-bonding between the remaining two dangling bonds lifts their degeneracy by lowering the π-bonding level and raising the π^*-level. [43]

This (2×1) periodicity was first observed in 1959 by Schlier and Farnsworth in their LEED studies of silicon. In the 1970s Hamann et al carried out a series of self-consistent calculations of the electronic potential, charge density, Fermi energy, and surface density of states for the two competing models of the Si(100)-(2×1) reconstruction. On the basis of comparisons with experimental data they concluded that the dimer model was the more probable. [45–47] They showed that the dimer bond length was slightly shorter than the bond length for atom pairs in the bulk as well as that surface dimerization produced elastic distortions of the first 4 to 5 subsurface layers. [48]

Building upon the Levine model, a modification of the one put forward by Schlier and Farnsworth, Chadi proposed that the most energetically stable reconstruction of Si(100) would be the asymmetric (buckled) dimer surface and not the symmetric dimer one [49]. An asymmetric dimer consists of a pair of bonded surface atoms such that one atom relaxes away from the bulk while the other towards it. The raised atom adopts a puckered sp^3 configuration and its dangling bond takes on a more pronounced s-state character, while the lowered atom adopts a trigonal planar sp^2 configuration and its dangling bond takes on a more pronounced p-state character. [43] The altered character of the orbitals translates into elastic strain which slightly modifies the geometric arrangement of the underlying layer as follows: the two atoms attached to the raised atom are drawn together, while the two atoms attached to the lowered atom are pushed apart. This results in adjacent dimers in a row buckling in the opposite sense. These distortions lower the energy of the higher dangling bond and raise the energy of the lower one. Charge is thus transferred between the dangling bonds causing one to become filled and one empty, thus increasing the ionic character of the bond. The resulting splitting in the π and π^* energy bands of the asymmetric dimer leads to the formation of an energy gap that explains the semiconducting surface bands observed, as opposed to the electronic metallic structure predicted for symmetric dimers. [6]

While various experimental techniques yielded results suggestive of dimer buckling (in

STM both types of dimers were observed to coexist), Wolkow resolved the controversy by employing low-temperature STM to show that dimers have an innate bistable asymmetric character which makes them appear symmetric at room temperature. [50] Room temperature STM images thus only show an average of the two buckled dimer configurations flipping between each other because the image acquisition time is much slower than the timescales associated with surface dynamics.

As was noted in the early STM experiments on semiconductor surfaces, the images acquired depend significantly on the polarity and magnitude of the bias applied to the probe. A telling example of this is provided by Si(100)-(2 × 1). STM images of symmetric dimers do not map charge density distributions corresponding to either σ or σ^* bonds, as it would be facile to assume, because these states are too far below the Fermi level to be accessible. Instead such images show charge density distributions associated with π bonding and anti-bonding states which are very close to the Fermi level. In occupied state imaging a maximum is observed between the nuclei which is at odds with the expected pair of prominent features localized at the nuclei predicted by the charge density model. In unoccupied state imaging one observes a pair of separate protrusions localized at the nuclei which agrees with the charge density contours of the π^* anti-bonding state. [43]

The distance between two adjacent dimers in a row is 3.84 Å, and the spacing between adjacent dimer rows is 7.68 Å. Because of the tetrahedral bonding structure of silicon the dimerization direction rotates by 90° from terrace to terrace. The existence of terraces separated by steps of single-layer height caused room-temperature LEED patterns to have (1 × 2) patterns superimposed on the (2 × 1) ones.

Surface defects quench dimer dynamics at room temperature giving rise to rows of buckled dimers. The strongest buckling occurs near the defect and decays away from it with a decay length of about 10 dimer units. Rows of buckled dimer appear to zigzag because the direction of buckling alternates. At room temperature defects stabilize buckled dimers and become nucleation sites for domains of asymmetric dimers that expand with decreasing temperature.

Different types of asymmetric dimer arrangements give rise to various reconstructions of which the most stable are the p(2 × 2) and c(4 × 2) reconstructions. For the p(2 × 2) structure the direction of buckling alternates only along the dimer rows, whereas for the c(4 × 2) it alternates both along and perpendicular to the dimer rows. Buckled dimers first appear extensively below 120 K and at about 4 K a transition occurs from the p(2 × 2) to the c(4 × 2) reconstruction such that the area occupied by the latter is the greater of the two. [51] The energy barrier associated with a dimer flip is about 0.1 eV. [52] The surface
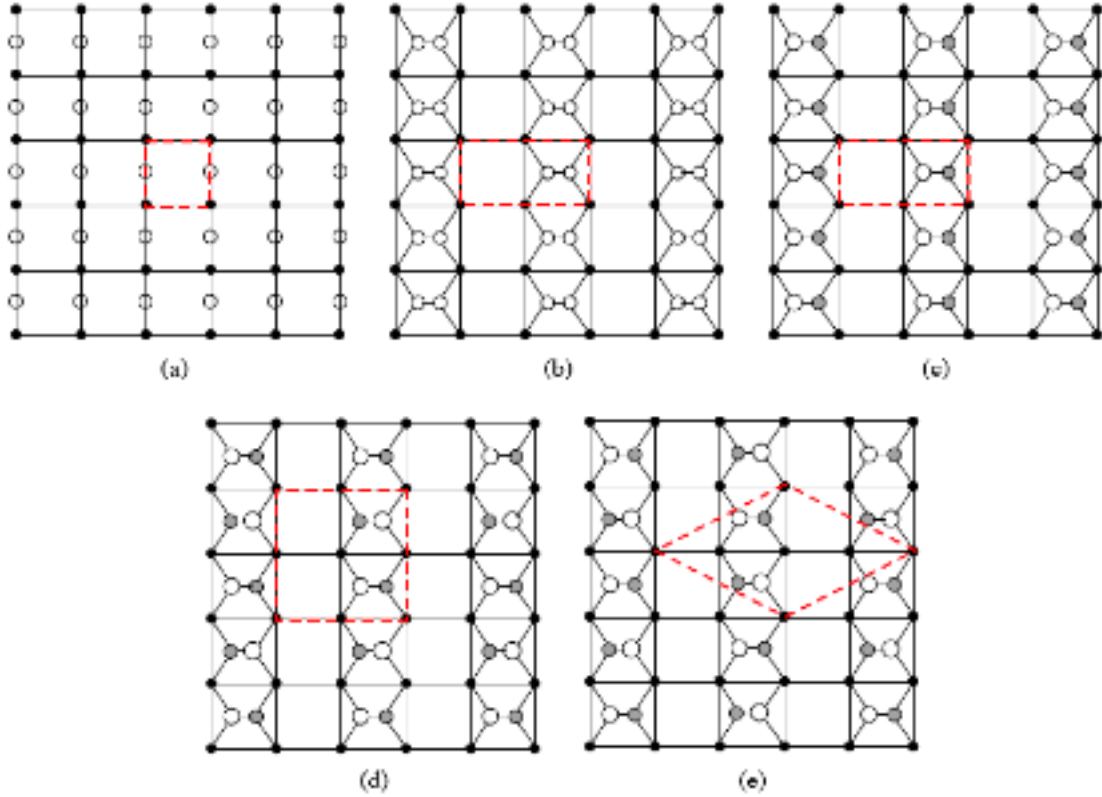
Figure 3.1: Top view of various unit cells of the Si(100) reconstructions. Small black circles indicate atoms in the second layer, small white ones surface atoms, while big white and small gray circles designate upward and downward buckled dimer atoms on the surface: (a) the non-reconstructed surface, (b) the (2 × 1) symmetric dimer reconstruction, (c) the p(2 × 1) buckled dimer reconstruction, (d) the p(2 × 2) alternating buckled dimer reconstruction, (e) the c(4 × 2) reconstruction. [5]

energy of the c(4 × 2) reconstruction is reported to be a few meV/dimer lower than the one of p(2 × 2). [53]

3.3.1 Step Edges

Chadi proposed a useful categorization of step edges comprising four groups [6]:

S_A, a monolayer height step such that the dimerization direction on the upper terrace is parallel to it;

S_B, a monolayer height step such that the dimerization direction on the upper terrace is perpendicular to it;

D_A, a double-layer height step such that the dimerization direction on the upper terrace is parallel to it;

D_B, a double-layer height step such that the dimerization direction on the upper terrace is perpendicular to it.

The S_A step was found to have the lowest formation energy. S_B steps exhibit kinks, that is, local sections of the more energetically favorable S_A step.

Of the double steps the, the D_B ones are more favored. Their formation energy exceeds the sum of the formation energies for one S_A and S_B step. Increasing temperatures causes a shift in the distribution of steps towards the monolayer height steps.

3.4 Si(111)

The Si(111) surface is obtained by cleaving a crystal such that the covalent bonds along the [111] direction are cut. Two possible types of terminations exist for Si(111) [5]:

T1 the shuffle-terminated face, Si(111)-(1×1), which has one single dangling bond per atom;

T2 the glide-terminated face, Si(111)-($\sqrt{3} \times \sqrt{3}$), which is a double-layer termination consisting of the shuffle-terminated face such that each previous dangling bond is capped with a silicon atom.

It is thought that only **T1** can be obtained by cleavage as breaking one bond per atom within the double layer is much less energetically-costly than breaking the three dangling bonds required for **T2** . The three dangling bonds per singly coordinated atom render **T2** unstable, and therefore reconstructs in order to minimize its surface energy. Both **T1** and **T2** are metallic. There are two different types of reconstructions for **T2**: the annealed (7×7) surface and the cleaved (2×1) surface. The latter reconstruction requires extensive displacement of the atoms in the top layers as well as further bond breaking. However, calculations by Northrup and Cohen showed that the barrier for transition from the bulk terminated to the chain bonded geometry of the Si(111)-(2×1) is very low. [54] Annealing this reconstruction to 870 K causes an irreversible phase transition to the (7×7) reconstruction, and further heating to 1120 K leads to Si(111)-(1×1). [40]

The imaging of Si(111)-(7×7) was the first great success of STM although it did not completely elucidate the structure of the reconstruction. Si(111)-(7×7) is amenable to the study of site-selective adsorption because of its large unit cell and variety of dangling bond sites. Its study could also shed light upon the formation of metal/semiconductor interfaces. [6]

The starting point for the structural model of this surface is to be found in 1959, when Schlier and Farnsworth reported a (7×7) LEED pattern for the clean Si(111). The currently accepted model is known as the dimer-adatom-stacking fault (DAS) model first proposed by Takayanagi et al in 1985. [55] According to this model the 7×7 unit cell consists of two triangular sub-unit cells one of which has a stacking fault (one layer interruption in the stacking sequence of the face-centered cubic structure). The 7×7 reconstruction can be thought of as three layers of different reconstruction stacked on top of a (1×1) unreconstructed surface. The layers, starting with the bottommost one, are as follows:

L1 the dimer layer; is an almost unperturbed layer of the $(\sqrt{3} \times \sqrt{3})$ reconstruction except that the four corner atoms of the unit cell are missing and that a string of dimers borders both triangular halves of the unit cell; all atoms have three unsaturated dangling bonds but the dimer atoms, which have two;

L2 the restatom layer; the restatoms saturate the dangling bonds of three underlying dimer layer atoms and in order to do so occupy normal sites in one half of the unit cell and stacking fault sites in the other;

L3 the adatom layer; twelve adatoms, six in each sub-unit cell, occupying sites of a local (2×2) structure, saturate 36 of the 42 nearly-perpendicular dangling bonds of the restatom layer.

This structure reduces the number of dangling bonds per unit cell from 49 to 19: one on each of the 12 adatoms, one on each of the uncapped restatoms, and 1/4 for each of the 4 corner holes. Compared to the unreconstructed Si(111)-$(\sqrt{3} \times \sqrt{3})$, which has 98 atoms, the (7×7) surface has 102.

Subsequent to the resolution of the (7×7) reconstruction, a series of less stable ones with similar structure were discovered. These have $(n \times n)$ unit cells, where $n = $ odd, obtained by varying the number of dimer in the strings. Changing the number of dimers does not significantly affect the energetics of the structure as most important in lowering the unit cell surface energy are the formation of dimer strings and the stacking fault. Additionally, varying the number of dimer rows preserves the triangular shape of the sub-unit cells, hence the similarity in structure.
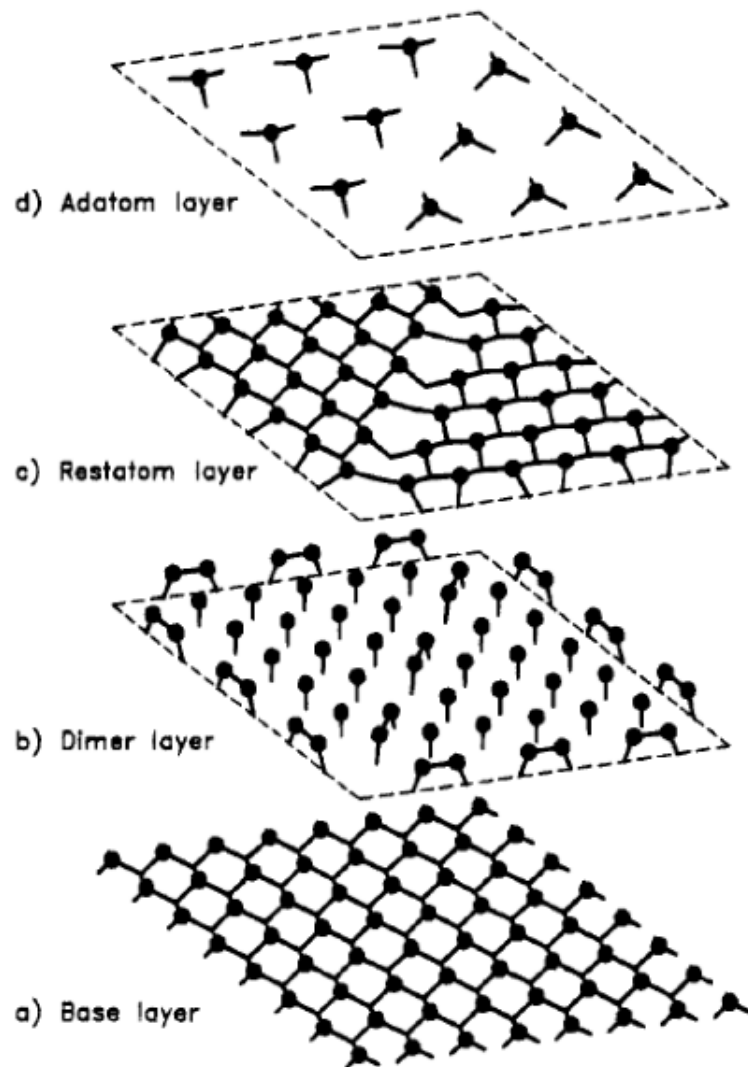
Figure 3.2: Layer-by-layer of the Si(111)-(7 × 7) reconstruction. [6]

3.5 Hydrogen-Terminated Silicon, H:Si(100)

The hydrogen-terminated silicon (100) surface is one of the most promising substrates for the fabrication of nanoscale devices as it readily lends itself to patterning and chemical modification (functionalization with various compounds). A monolayer of hydrogen capping the dangling bonds on Si(100) acts as resist because the very strong silicon-hydrogen (Si-H) bond ensures a high degree of passivation of the surface chemistry. In UHV systems hydrogen-covered silicon surfaces are usually obtained by exposing the single crystals to atomic hydrogen, as the reactivity of molecular hydrogen towards silicon surfaces is very low. Si-H bonds are energetically preferred as they are stronger than both Si-Si bonds in dimers and in bulk. A good understanding of the processes underlying Si-H bond formation and destruction is essential in atomic hydrogen manipulation with a UHV-STM.

Three different terminations have been observed on H:Si(100). Initially, Ibach and Rowe suggested that the (2×1) reconstruction is preserved as hydrogen interacts with the one remaining dangling bond per surface Si atom to yield a (2×1):H monohydride surface. [56] Sakurai and Hagstrom subsequently suggested that exposure beyond the formation of the (2×1):H monohydride surface causes bond breaking in the Si dimers and thus, the formation of a (1×1):H dihydride surface. [57] The existence of a (3×1):H phase consisting of what they supposed to be alternating monohydride and dihydride units was demonstrated by Chabal and Ragavachari. [58] The terminations depend both on the coverage and adsorption/annealing temperature of the crystal. The general consensus is that H:Si(100)-(2×1) forms after saturation exposure to atomic hydrogen of a surface maintained at about 600 K. The dihydride phase was believed to occur at saturation for temperatures below the monohydride formation temperature (295 K). The initial (3×1):H structure was obtained after saturation hydrogen coverage at about 400 K. In IR studies both (3×1):H and (1×1):H were found to exhibit similar hydrogen coverages consisting of alternating rows of monohydride and dihydride subunits, which are disordered in the latter case. While in the case of (3×1):H STM confirmed the alternating structure, in the case of (1×1):H, regions of bulk-like termination were found suggesting dihydrides result from hydrogen insertion in surface dimers.

An STM study conducted by Boland of H:Si(100) disambiguated the previous views on the relationship between the three above-mentioned phases. The (3×1):H phase was found to be a well-defined one. Exposure of a surface exhibiting this phase to atomic hydrogen at 295 K resulted in a surface that had local (1×1):H structure susceptible to etching. The (1×1):H surface was found not to be well-defined as no uniform dihydride phase was observed. Furthermore, coverage was found to vary with exposure conditions. The dominant aspect governing hydrogen on Si(100) was shown to be the enhanced reactivity of strained surface bonds. It is the steric interaction between dihydride units that leads to strained bonds, and thus stabilizes (3×1):H and destabilizes (1×1):H over the range of tempera-

31

tures from about 380 to 420 K. The steric interaction lowers the Si-Si backbond reaction barrier and the bond is rendered susceptible to further attack and etching by hydrogen atoms during exposure to atomic hydrogen, causing the creation of etch pits. Therefore, etching occurs to relieve the strain in the backbonds of the dihydride units on (1×1):H.

The weakening of the Si-H bonds of dihydride units results in an anomalously low threshold to hydrogen thermal desorption which renders (3×1):H stable at about 400 K. In conclusion, the formation of the monohydride surface at 600 K is due to the instability of the (3×1):H dihydride units at this temperature, just as the formation of the (3×1):H surface at 400 K is due to the instability of the (1×1):H dihydride units. [7]
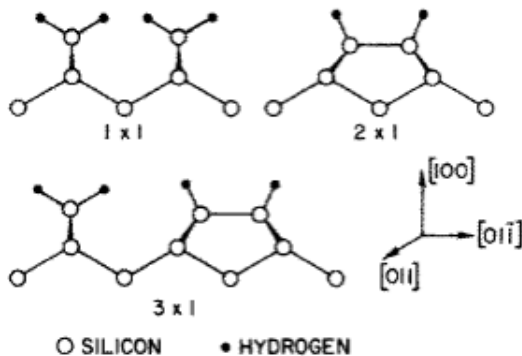
Figure 3.3: Hydrogenated structures associated with Si(100). [7]

3.6 Hydrogen Desorption in Scanning Tunneling Microscopy Experiments

The H:Si(100)-(2×1) has a high structural and electronic uniformity, and is preferred to H:Si(111)-(7×7) for hydrogen manipulation experiments because of its technological relevance. H:Si(111)-(1×1) reverts to a 2×1 reconstruction upon hydrogen removal and, moreover, Si(111)-(2×1) accommodates three equivalent domains rotated by 120° relative to each other and also exhibiting disordered domain boundaries. [18]

Hydrogen-terminated Si(100)-(2×1) is most commonly prepared with the dry etching process, which entails heating the silicon surface to approximately 650 K in an atmosphere of atomic hydrogen (UHV chamber backfilled to 10^{-6} Torr) produced by decomposition of molecular hydrogen on a incandescent tungsten filament. The sample surface is heated in order to prevent the formation of higher hydrides and surface etching. At this temperature, only the surface π bond of each silicon dimer atom reacts with hydrogen, forming the uniform monohydride surface. Pairwise dimer occupation is energetically favored by the fact that the repulsive interaction between the two hydrogen atoms on the same dimer is

lower than the π-bond interaction. [22] While the 2×1 structure of Si(100)-(2×1) and H:Si(100)-(2×1) looks similar, the latter has a noticeably lower density of states in the gap region.

Hydrogen ablation can be achieved both by scanning an STM tip over the surface while applying a continuous bias of several volts and by applying pulses of several volts between the tip and the surface. Both nanometer- and atomic-scale patterning were demonstrated on H:Si(100)-(2×1). [22]

The first attempts at controllably modifying silicon surfaces, while demonstrating nanometer resolution, were perturbative to both the surface and the tip. They did not involve removing hydrogen atoms but individual or small clusters of adatoms from Si(111)-(7×7). This was done by applying voltage pulses to the tip while in tunneling mode. [59] Subsequent techniques also employed atom extraction but to pattern grooves on Si(111)-(7×7). [60]

Prior to selective desorption experiments on H:Si(100)-(2×1), the first STM depassivation experiments were carried out in UHV by Becker et al. [61] and Boland on H:Si(111) surfaces. The former reported atomic resolution STM images for wet chemically passivated H:Si(111)-(1×1) surfaces and also mentioned the ability to depassivate areas as small as 40 Å in diameter with an STM tip. The latter observed that using scanning parameters they had previously employed for tip sharpening (+5 V, 1 nA) on H:Si(111)-(7×7), that is, operating the STM in field emission mode, resulted in electron stimulated desorption (ESD) of hydrogen from the surface. [62]

It was Lyding et al [22] who first successfully performed STM nanolithography experiments on a UHV-passivated H:Si(100)-(2×1) surface. The patterns they created were a 23 nm $\times$ 32 nm square using a 1.0 nA current at a tip bias of -5.5 V with respect to the sample, as well as a series of 1- and 5-nm-wide lines using a 2 nA current at a -4.5 tip bias, and a 0.1 nA current at a -7 V tip bias, respectively. The patterns appear brighter as depassivation causes the clean surface π-bonded state to be restored, which increases the efficiency of electron transfer between the probe and surface. The absence of subsequent repassivation of the patterned areas suggested that associative recombination occurs whereby H_2 is evolved. Assuming a realistic, nontrapezoidal barrier shape, they deduced that depassivation takes place for tip voltage biases in the range -5.5 to -6.5 V, that is, only when the classical electron energy exceeds the Si-H bond strength, $E_{\text{Si-H}} = 3.5 - 3.8$ eV. In the case of the lower voltages a higher patterning resolution was observed, as the tip was brought closer to the sample thus reducing the beam divergence. The desorption mechanism was found to have a strong dependence on the magnitude and polarity of the tip voltage bias.

Initially, depending upon the polarity of the bias voltage applied between the tip and the sample two desorption mechanisms were put forward: the electron-induced excitation model and the electric field effect model. [63] When the sample is positively biased, that is, electrons are tunneling from the tip into the surface, the fraction of the impinging electrons involved in inelastic tunneling induce excitations that can lead to the breaking of the Si-H bond. The first to explore the desorption processes involved in the electronic excitation regime were Shen et al in 1995. [64] They proposed two distinct mechanisms for positive sample bias hydrogen removal:

M1 direct electronic excitation of the Si-H bond by electrons field-emitted from the tip, in the high-bias regime ($V_{sample} > 6.5$ V);

M2 resonantly-enhanced multiple-vibrational excitation/heating of the Si-H bond induced by multiple inelastic tunneling events, in the low-bias regime ($V_{sample} < 6.5$V).

The dependence of the desorption yield on the applied voltage revealed that the onset of the field emission regime occurs at the threshold of roughly 6.5 V. For energies in excess of the threshold the yield was found to remain nearly constant, while for energies below the threshold the yield dropped several orders of magnitude and became strongly current- and voltage-dependent. This suggests that below the threshold many electrons are involved in the excitation process. The threshold was consistent with electron energy loss spectra which associated 6 to 8 eV to the electronic excitation of the Si-H group. Furthermore, calculations also corroborated that this corresponded to the σ(Si-H) to σ^*(Si-H), bonding to antibonding transition.

In the case of the multiple-vibrational excitation, the degree of vibrational heating is determined by the interplay between excitation and relaxation processes: while electrons drive the vibrational excitation, coupling to phonons dissipates the energy into the bulk. Compared to the very short vibrational lifetimes of hydrogen adsorbed on a metal (about 10^{-12} s), the much longer vibrational lifetimes of hydrogen on silicon: about 10^{-9} s for H:Si(111), and 10^{-8} s for H:Si(100) favor vibrational excitation. Two different mechanisms were proposed to lead to multiple-vibrational excitation:

M21 dipole excitation, which only involves the interaction between the field of the incident electron with the transition dipole moment μ of the transition mode;

M22 resonance excitation, which relies on the electrons being temporarily trapped in an unoccupied or partially occupied adsorbate level.

M21 is independent of the electron energies provided that the energy requirement for the excitation is met, in which case the ratio of the inelastic to elastic tunneling f_{in} is solely dependent on μ. On the other hand for **M22** the excitation probability is energy-dependent and roughly proportional to the DOS of the resonance evaluated at the Fermi energy of the

tip.

Modeling the Si-H bond as a truncated harmonic oscillator, and employing the steady-state solution of the master equations describing the population levels of the oscillator yielded $f_{in} = 10^{-3}$, which was the expected order of magnitude for inelastic tunneling. Shen et al concluded that the hydrogen desorption mechanism in the range from 2 to 5 V proceeded via the resonantly-enhanced multiple-vibrational mechanism based on the fact that the strength of the tip field does not vary significantly in constant-current mode and that the voltage dependence of the yield was related to the energy dependence of the excitation cross-section. They also succeeded in writing a pattern of parallel lines consisting of both single and adjacent dangling bonds located on the same dimer, at a sample voltage bias of 3 V, using a 4.5 nA current. [64]

When the sample is negatively biased, that is electrons tunnel from the occupied states of the sample into the tip, a field-induced mechanism was hypothesized to dominate. In this case the strong electric field created by the tip lowers the binding energy of the tip resulting in hydrogen ablation. This model was supported by STM experiments carried out using hot tips on both H:Si(100)-(2 × 1) and H:Si(100)-(3 × 1), at both sample bias polarities. The following observations, garnered within those experiments, were all consistent with the electric field mechanism. The extraction probability P increased with increasing tunneling current, I, which led to a decrease in tip-sample separation and also an increase in the electric field. A higher I was required for a negative sample bias than for a positive one, as negative ions are more energetically-costly to produce. P decreased at high temperature as the field at the surface of a semiconductor also decreases with temperature. Finally, hydrogen extraction on a H:Si(100)-(3 × 1) occured preferentially at the dihydride units rather than monohydride units because, in accordance with thermal desorption results, hydrogen atoms on dihydrides are extracted at a lower electric field than on monohydrides.

Yamamoto et al also showed hydrogen extraction from H:Si(100)-(2 × 1) using 50 to 300 ms long voltage pulses of ±8-9 V while maintaining a constant current of 2 nA for positive sample polarity, and 10 nA for negative polarity. They found hydrogen extraction equally likely to occur in both cases, but redeposition to be more likely for negative pulses. In an attempt to fabricate a chain of dangling bonds employing three consecutive 50 ms wide, 8 V pulses they observed that in the field-emission regime extraction occurred mostly in a pairwise fashion from the dimers just as in the thermal desorption process. Furthermore, others reported the creation of a hydrogen-free in the case of negative sample bias (−7.0 V).

Unlike in the case of thermal desorption in which the thermal energy is uniformly distributed among all surface hydrogen atoms, in the case of tip-induced desorption energy

transfer may be localized to only the hydrogen atom below the tip. This implies that even though there is no direct bond between the hydrogen atoms on a dimer, energy is nevertheless transferred via a nonlinear harmonic system comprising the H-Si-Si-H bonding system. Since energy transfer entails a certain energy expenditure, it was argued that hydrogen pair extraction from a single dimer depends on the energy applied to the hydrogen atom directly below the STM tip. For small energies the pairing effect may be attenuated. A more energetically-costly scenario would entail energy transfer from a hydrogen atom below the STM tip to a hydrogen atom on an adjacent dimer. It has been confirmed experimentally that hydrogen atoms on adjacent dimers may not be simultaneously removed, and therefore that hydrogen pair extractions mostly occur on the single dimers .

On the other hand, in the inelastic scattering regime two-hydrogen desorption most often involves pairs of dimers, in the same or adjacent rows, and desorption of paired hydrogen atoms from individual silicon dimers is rarely observed. This therefore favors single atomic precision in creating dangling bond patterns on H:Si(100)-(2×1). Tong and Wolkow found that there may be multiple channels for pairwise hydrogen desorption (intradimer, interdimer and interrow desorption pathways), by gathering statistics on the populations of multiple dangling bond configurations created by current-volatge pulses in the vibrational excitation regime.

Subsequent to the first attempts at describing the extraction mechanism on H:Si(100)-(2×1), Avouris et al put forward a more in-depth experimental and theoretical analysis of individual bond breaking via STM-induced excitations. They argue that regardless of the nature of the excitation, for it to bring about a local material modification it has to remain localized on site for the required length of time. Localization is frustrated by such phenomena as excitation quenching (energy transfer to the substrate), and excitation delocalization (energy transfer to the surrounding adsorbates). In order to ascertain whether or not the electric field of the STM could sufficiently shift the excitation field energy of the adsorbate to de-couple it from its neighbors and thus inhibit energy transfer away from it, they performed first principles electronic structure calculations which incorporated the electric field. The theoretical findings reveal that the effect of the field depends critically on its direction with respect to the bond axis. Increasing fields directed from H towards Si monotonically decrease the Si-H bond strength, while negative fields first increase then slowly decrease the bond strength. The Si-H stretch energy is affected in the same fashion by the field as the Si-H dissociation energy. So normal STM-induced fields were deemed sufficient to cause appreciable Stark shifts (averaging about 50 cm^{-1}), which would significantly reduce coherent and incoherent energy transfer by 2 and 3 orders of magnitude, respectively.

As regards desorption by direct electronic excitation they pointed out that under writing

conditions the field is much too low to influence the desorption process, and that desorption from a hot ground state can occur because of the strongly repulsive excited state and fast quenching.

In the low energy tunneling regime the Stark shift is considered responsible for aiding desorption by inducing excitation localization. The voltage dependence of the desorption yield in this regime suggests that the vibrational excitation is enhanced by a temporary negative ion resonance, predicted by electronic structure calculations to reside about 2 eV above the Fermi level.

In order to further test and clarify aspects of the STM-induced hydrogen desorption mechanism for positive sample bias, Avouris et al carried out experiments investigating the isotope effect on H(D):Si(100)-(2 × 1). While the experiments confirmed the existence of a bias threshold of about 6 V they also highlighted the importance of the dynamics of the desorption process. The desorption yield depends upon the interplay of two competing effects: motion of the Si-H(D) monohydride species on the excited state potential energy surface and quenching of the electronic excitation. In addition to the atoms that undergo direct desorption by surviving on the excited state curve, others acquire sufficient kinetic energy to escape the remaining attraction of the ground state potential, and desorb thus.

The experiments showed that the desorption thresholds were the same for both the hydrogenated and deuterated surfaces, suggesting identical desorption mechanisms. However they also observed a marked suppression of the desorption yield (by a factor of about 50) for the latter surface as compared to the former. By ab initio self-consistent field calculations they obtained the potential energy curves of the ground and σ^* excited states of the Si-H bond. As the center of the Gaussian wavepacket generated by the excitation process moves out, away from the stable bonding position, its amplitude diminishes by 5 orders of magnitude for hydrogen, and more than 6 for deuterium, in about 4 - 5 fs. Therefore desorption is arrested more readily for deuterium as it is more likely to fall back into the bonding potential well and reform the bond. This additional quenching of deuterium due to its slow motion engenders the giant isotope effect.

In 1998, Avouris et al. presented results obtained by studying the temperature dependence of STM-induced hydrogen and deuterium desorption from Si(100). [65] A strong dependence of the desorption yield on temperature was found in the tunneling regime, namely that hydrogen was easier to desorb at 11 K than at 300 K by a factor of about 300, and that deuterium removal, unlike at 300 K, was possible at 11 K . The low temperature results are consistent with the following facts: the high frequency of the Si-H oscillator is high enough that the excitation spectrum should be weakly dependent on temperature,

and the excited state lifetime (1 fs) is short enough that temperature effects arising from phonon-assisted energy transfer processes are minimized. An unusually high isotope effect was also noticed at 11 K the desorption yield for deuterium being suppressed by a factor of about 50 with respect to the hydrogen yield, which once more confirmed that an allowed electronic transition was involved and that no thermal activation was needed.

In the tunneling regime, the desorption rate acquires temperature dependence by being a function of the phonon-assisted energy transfer rate, λ, and the vibrational decay rate (the inverse of the vibrational lifetime), ω_{vib}. Upon cooling, in the presence of the tip-induced electric field, λ was calculated to change by less than a factor of 2. Therefore, the main factor determining the desorption rate was judged to be ω_{vib}. By analogy to the Si-H relaxation on Si(111), whose decay involves three quanta of the Si-H bending mode and a 200 cm^{-1} Si phonon [66], they argued that, given the very high stretching frequency of the Si-H mode 2000 cm^{-1}, the preferred decay channel would be a multiphonon process involving the least number of vibrational quanta. ω_{vib} was found to decrease by a factor of 2 by cooling to 11 K, leading to a 300-fold increase in the desorption rate at 11 K, in good agreement with the experimental results. This highly nonlinear character of the excitation process was invoked to explain the temperature dependence of the desorption yield in tunneling regime. The frequencies of the Si-D modes are lower than those of Si-H by a factor of $\sqrt{2}$, which changes the efficiency of the vibrational up-pumping process, and thus would explain why deuterium desorption is only observable at cryogenic temperature.

Desorption occurring for negative sample biases was also explored more in depth, and in 1998, hole resonance was reported to be responsible for the desorption mechanism on H:Si(100)-(2 $\times$ 1). Also, significantly higher bias and tunnel currents were found to be required in negative bias than in positive. [67]

In addition to performing hydrogen desorption at negative sample bias, desorption rates were also obtained theoretically. The method employed for obtaining inelastic scattering rates was one based on first principles electronic structure calculations. Desorption rates were obtained as in previous papers by solving the Pauli master equation for a truncated harmonic potential well.

For desorption events occurring at sample biases of -5 V and -7 V a power-law dependence of the desorption rate upon the current was derived:

$$R = R_0 \left(\frac{I}{I_{des}} \right)^{\alpha},$$

where $\alpha \approx 6$, and I_{des} is the current that gives rise to a fixed desorption rate R_0.

The voltage dependence of the desorption rate was extracted from measurements of the I_{des} for V_b in the range from -10 V to -4 V. The measurements entailed scanning 30 nm along a single dimer row at the I_{des} required such that 50% of the hydrogen be removed from the line. I_{des} as a function of sample bias voltage was found to display a minimum at about -7 V and increase below that value. [67]

The conjectured negative-bias desorption mechanism is analogous to the vibrational heating one caused by scattering with an electron resonance in positive bias, only in this case the 5σ hole resonance transfers energy to the hydrogen atom upon deexcitation. The calculations, which were in good agreement with the experimental results, revealed that the minimum of $I_{des}(V_b)$ corresponds to the onset of the field emission regime. The letter concluded that in the 0 V to -6.5 V range $I_{des}(V_b)$ was mainly determined by the shape of the resonance wave function, while below -6.5 V it arises from the competition between polarization of the hole resonance, and increasing Fermi level conduction as the tunnel barrier to the 5σ state increases with decreasing bias.

A subsequent paper [68] focuses on the temperature by investigating hydrogen desorption at negative sample biases from -10 V to -4 V and temperatures from 300 K to 610 K. The desorption rate, R, was found to decrease by a factor of 200 at $V_b = -7$ V for a temperature increase of 80 K, and by a factor of 3 at $V_b = -5$ for the same temperature change. In the former case the temperature dependence of R is attributed to the temperature dependence of the 5σ hole resonance lifetime, while in the latter, to the temperature dependence of the vibrational excitation lifetime. As in the previous paper good agreement was reported between experimental and theoretical curves of R as a function of the tunneling current for -7 and -5 V, at 300, 380, and 450 K. In modeling the desorption process the diffusion of the excitation into the hydrogen overlayer through incoherent exciton motion is negligible due to the anharmonicity of the Si-H bond potential.

For extracting the relationship between I_{des} and V_b the same procedure as above was employed. For all temperatures the curves retain the same features as the one at 300 K. Also, for all voltages, R was found to decreases with temperature. However, for $V_b < -5$ V the coupling constant between energy relaxation and phonon modes does not fully account for the temperature dependence. Therefore, the temperature dependence of the 5σ hole resonance lifetime is considered via electron-phonon couplings and electronic coupling with substrate eigenstates. The theoretical curves were in good agreement for the $I_{des}(V_b, T)$ data set.

The table below summarizes the findings to date of desorption experiments performed at positive sample bias:

Table 3.1: Summary of experimental findings related to hydrogen desorption at positive voltage bias.

	11 K	300 K
Deuterium	- desorption is detectable in vibrational heating regime - desorption yield about 2 orders of magnitude lower in electronic excitation regime (compared to hydrogen)	- no desorption in vibrational heating regime - desorption yield about 2 orders of magnitude lower in electronic excitation regime (compared to hydrogen)
Hydrogen	- desorption yield 300 times higher than at 300 K in the vibrational heating regime (strongly current dependent)	- desorption yield comparable to the one at 11 K in the electronic excitation regime

3.7 Hydrogen Desorption Revisited

In 2003 Dujardin and his collaborators [69] conducted hydrogen desorption experiments on H:Si(100) - (2×1) in order to elucidate the exact mechanism underlying this phenomenon in the low-bias regime, $V_{sample} < 3.5$ V. The findings of their experiments would contradict the belief that Si-H bond dissociation occurs after inelastic tunneling interactions with a large number of electrons (about 10).

Throughout their experiments the sample voltage was maintained at 2.5 V, below the Si-H bond energy, $E_{Si-H} = 3.5$ eV. In order to investigate the extraction yield as a function of the tunneling current and the doping of the silicon sample (highly As-doped n-type and medium B-doped p-type), they employed two methods, that is, they performed desorptions in stationary mode as well as in scanning mode (both parallel and perpendicular to dimer rows).

In stationary mode the tip is positioned over a selected hydrogen atom while the feedback loop is on whereafter a voltage pulse is applied and the current is raised from 0.5 nA to 1 to 10 nA for the amount of time required to engender a desorption event (on the order of ms). In scanning mode the desorption parameters are applied while scanning. It is worth pointing out that in scanning mode there is the possibility that the existence of dangling bonds in the vicinity of the newly created ones may influence the desorption yield, while in stationary mode desorption sites can be selected such that they are far enough away from defects to eliminate their influences. The advantage of the former over the latter is the more facile collection of large data sets.

In stationary mode for the p-type sample the desorption yield was found to be proportional to the power law I^{α}, where I is the tunneling current and $\alpha = 0.3$. In scanning mode

no difference in yield was observed between dimer-parallel and dimer-perpendicular scans. However, for p-type samples $\alpha = 0.8$, whereas for n-type samples $\alpha = 1.3$. This is consistent with the fact that electron in n-type silicon possess an available dissipation energy higher than electrons in p-type silicon do.

(a)   (b)
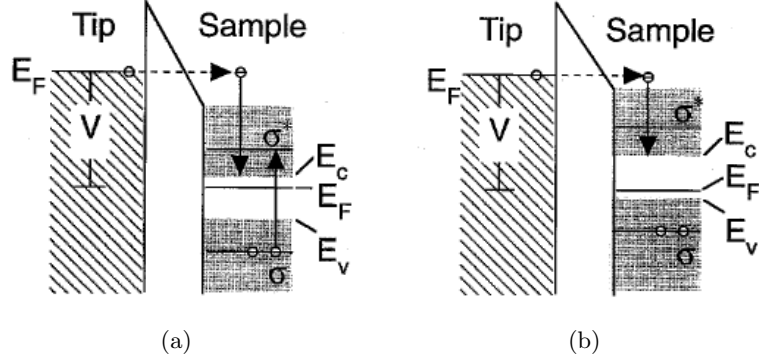
Figure 3.4: Diagram showing the available dissipation energies for tunneling electrons in (a) an n-type Si sample (about 2.5 eV) and (b) a p-type Si sample (about 1.7 eV). E_C, E_V, and E_F denote the conduction band minimum, valence band maximum, and Fermi level respectively (band bending is neglected). [8]

These values were derived from the larger statistical ensemble (each data point represents the average of about 100 events) afforded by the scanning mode. Large variations were observed between experiments performed at the same tunneling current which indicates a large variability in tip properties.

The results above contradict the values of α found in previous studies which were in the 10 to 15 range. These discrepancies were ascribed to:

1 the large error bars inherent in desorption experiments,

2 the inadequacy of the data sets utilized in previous studies to derive a power law.

The inadequacy above refers to data scarcity (sets of only 2 data points) and narrow tunneling current ranges (2 to 3 nA). Unlike previous studies, this study bases its findings on numerous sets of 4 data points in the range 1 to 10 nA obtained from experiments with many different tips.

The study concludes that while it is true that hydrogen desorption occurs by inelastic energy dissipation of tunneling electrons, the low α they found favors a desorption model similar to the coherent multiple excitation model involving resonant scattering off the σ^* unoccupied orbital. Moreover, a value of α close to 1 suggests a one- or two-electron process wherein the electrons impart a large number of vibrational quanta to the bond.

3.8 Alternate View on Hydrogen Desorption

In a letter published in 1991, Tsong [70] discusses a mechanism whereby STM tips may enable atom manipulation, cause surface atom desorption, or tip-to-sample atom transfer. His approach to investigating the tip-sample interactions in STM stems from his expertise in field ion microscopy and phenomena closely related to this technique.

While the bias voltage used in STM experiments is too low to trigger the field evaporation of surface atoms or the field desorption of adsorbates the proposes that the theoretical models developed for these phenomena in field ion microscopy be adapted to the tip-sample configuration in STM.

He considers the following scenario wherein an adatom, initially bound to the tip, interacts with both the tip and the sample in an STM. The tip can be assumed to terminate in a facet parallel to the sample surface and large relative to the range of the atom-surface interaction and the tip-sample distance. At large distances the overlap between the tip-atom and the sample-atom interaction potential energy curves, U_{at} and U_{as} respectively, is negligible. However, as the distance is reduced the overlap increases. While at room temperature the adatom chemisorbed to the tip cannot overcome the binding energy Λ_t, as the tip-sample separation decreases the potential energy curve describing the interaction of the atom with both he tip and the sample $U_a = U_{at} + U_{as}$ changes to exhibit two humps. Viewed from the tip side the hump height is Q_0, and $Q_0' = Q_0 + (\Lambda_s - \Lambda_t)$ from the sample side, where Λ_s represents the binding energy of the atom to the sample. The transfer rate from the tip side to the sample side for a thermally activated atom is $\kappa = \nu \exp(-Q_0/kT)$ while the reverse transfer rate is $\kappa = \nu \exp(-Q_0'/kT)$. Taking a hump height of 0.772 eV and $\nu = 10^{13}$ s^{-1} yields a transfer rate of 1 s^{-1}.

The probabilities of finding the atom on the tip side and the sample side are given by:

$$\frac{\exp(Q_0')}{\exp(Q_0') + \exp(Q_0)} \text{ and } \frac{\exp(Q_0)}{\exp(Q_0') + \exp(Q_0)} \text{ respectively.}$$

Nearly equal binding energies for tip and sample would yield nearly equal probabilities of finding the atom adsorbed onto either tip or sample. Also, adequate substrates and metal tips can be chosen such that for a given adsorbate transfer is favored in one direction over the other depending on the greater of the two binding energies. It is also conceivable that inelastically tunneling electrons may provide the requisite energy for adsorbates to undergo transfer.

In conclusion, the act of bringing the tip and the sample in very close proximity (which is the case for high current settings on the order of a few nA in the low-bias desorption
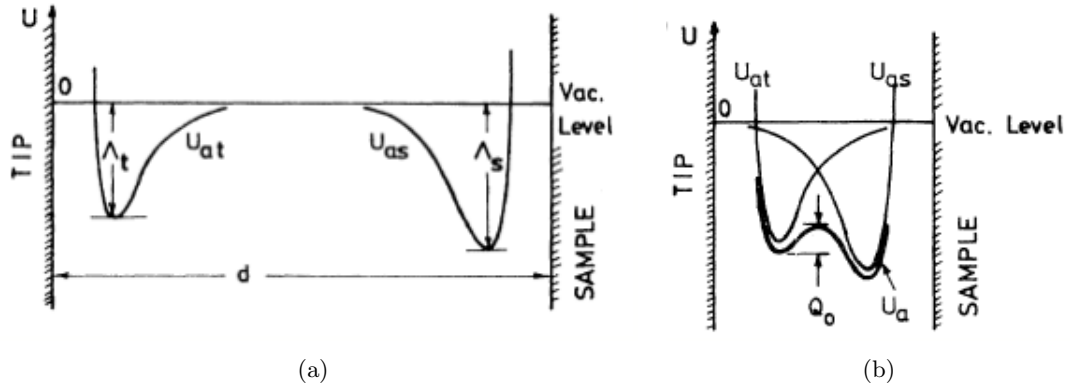
Figure 3.5: Diagrams of the tip-atom and sample-atom interaction potential energy curves for (a) large tip-sample separations when the overlap is negligible and (b) small separations when the potential takes on a double-well structure which effectively lowers the desorption barrier to the value of Q_0.

regime) can considerably reduce the effective barrier to atom desorption and thus enable atom transfer from tip to sample or vice versa.
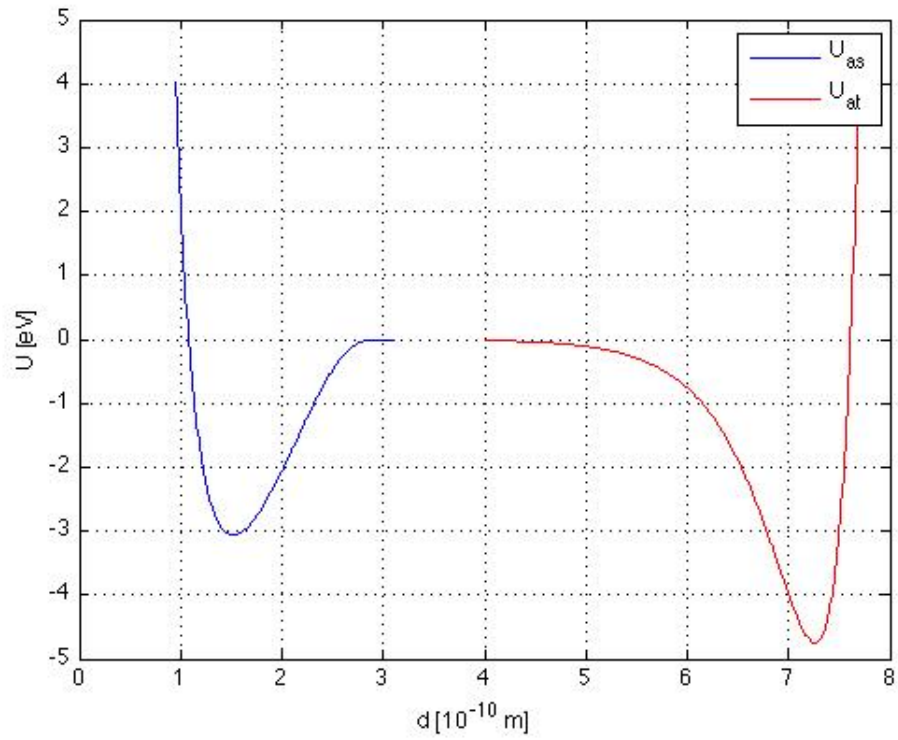
Figure 3.6: Diagram of the tip-atom and sample-atom interaction potential energy curves for a system comprising a silicon substrate, a hydrogen adatom, and a tungsten tip. The overlap between the two curves is virtually zero for a separation of about 5 Å. [9]
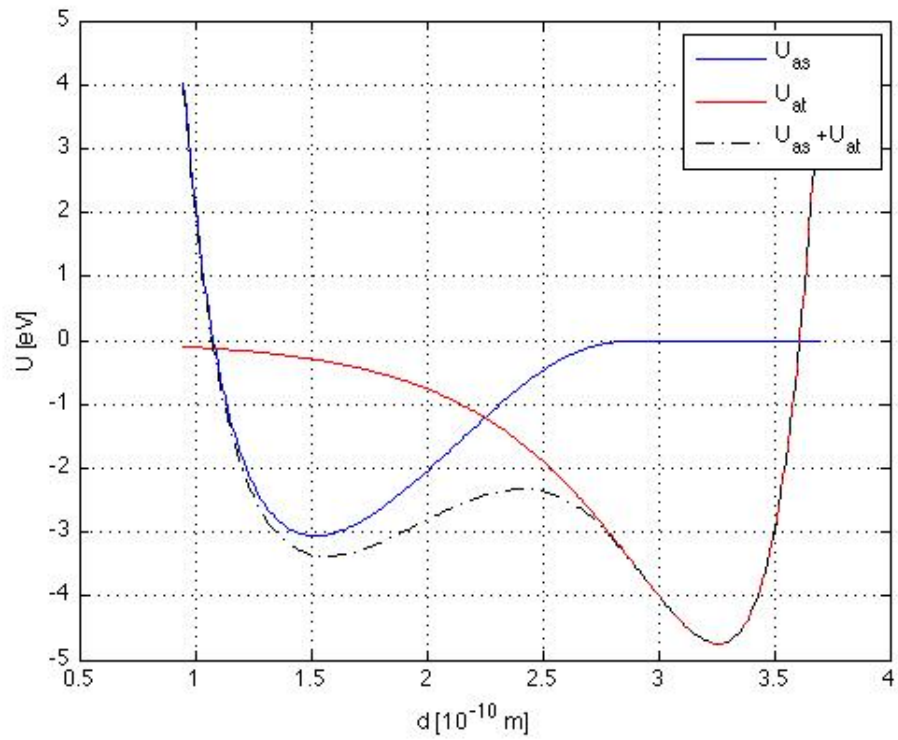
Figure 3.7: Diagram of the tip-atom and sample-atom interaction potential energy curves for the same system as above only for a separation of about 2 Å. The overlap between the two curves is considerable causing an effective lowering (from 3 to about 1 eV) of the desorption barrier for a hydrogen atom chemisorbed onto the sample. As the W-H bond is stronger a hydrogen atom is more likely to be found adsorbed onto the tip. [9]

45

3.9 Computation of STM Tip-Induced Stark Shifts in the Si-H Bond

As part of this thesis calculations were performed to estimate the tip-induced field shifts in the energy levels of the Si-H bond. This chapter outlines these calculations. First the tip-induced fields were evaluated for two types of tips (terminating or not in apical tungsten atom) of three different radii: 4 nm, 20 nm, and 40 nm. To perform these calculation the finite element Electrostatics Toolkit developed by Field Precision was employed. The component programs of the toolkit are Mesh and EStat. The former is used to generate the finite element mesh for the system while the latter solves the differential equations for the electrostatic system.

The tip was assumed to be axially symmetric and therefore the system under consideration was modeled as a cylindrically symmetric system. The system consists of four regions: the tip, modeled as an electrode to which a voltage of ± 3.5 V was applied, the silicon crystal, modeled as a 150 Å thick dielectric ($\epsilon_{Si} = 11.68$), the vacuum, and a grounded conductor located below the dielectric in contact with it.The grounded conductor accounts to some extent for the mobile charge carriers of a medium As-doped, n-type silicon crystal ($R = 0.1$ Ωcm, dopant concentration $N_d = 7.77 \times 10^{16}$ cm^{-3}). The tip apex is located 4 Å above the dielectric, a reasonable estimate for the the tip-sample separation for high tunneling currents (on the order of 1 nA). Within a region encompassing the tunneling gap and a portion of the dielectric below the vacuum interface the mesh size along the radial direction is 0.1 Å, while along the height it is 0.05 Å, sufficient for obtaining an accurate estimate for the electric fields. The calculations yielded two values for the electric field: one within the vacuum gap and one inside the dielectric. The fields obtained were averaged over a narrow region below the apex of the tip.

The values of the tip-induced fields obtained by finite element methods are tabulated below:

Table 3.2: Tip-induced electric field inside dielectric.

Tip radius (nm)	Field (V/Å)	
	no apical atom	with apical atom
4	0.095	0.075
20	0.074	0.062
40	0.062	0.054

The time-independent Schrödinger equation for the Morse-like potential associated with the Si-H bond was solved numerically in Matlab by discretizing the differential equation using the three-point finite difference scheme. [71] The time-independent Schrödinger equa-

Table 3.3: Tip-induced electric field within vacuum gap.

Tip radius (nm)	Field (V/Å)	
	no apical atom	with apical atom
4	0.48	0.54
20	0.35	0.41
40	0.29	0.36

tion,

$$-\frac{\hbar^2}{2m}\frac{d^2}{dx^2}\psi(x) + V(x)\psi(x) = E\psi(x) \text{ thus becomes:}$$

$$-\frac{\hbar^2}{2m}\left(\frac{\psi_{i+1} - \psi_i}{h^2} - \frac{\psi_i - \psi_{i-1}}{h^2}\right) + V_i\psi_i = \lambda\psi_i,$$

where m is the reduced mass of the system in the limit where the Si atom is considered fixed, the index i identifies the grid point on the one-dimensional mesh, and h is the grid size between two adjacent points x_i and x_{i+1}. The mesh spacings h are all uniform, which therefore generates a tridiagonal symmetric matrix. Matrix diagonalization yields the energy eigenvalues corresponding to the eigenstates of the Si-H bond. The energy eigenvalues were computed for the unperturbed Morse-like potential as well as the potential modified by superposition of the tip-induced electric field, and the energy shifts were obtained thus. The fields obtained are too low to significantly alter the electron distribution of the Si-H bond and therefore its polarizability is neglected. For these calculations the approximation that the bond dipole energy depends linearly upon the separation of the atoms is also employed. The two-body interaction potential of the Si-H bond employed in these calculations takes the following form in units of kcal mol^{-1} and Å [72]:

$$V(x) = \begin{cases} \alpha_{SiH}(\beta_{SiH}x^{-p} - 1)\exp\left[\frac{\gamma_{SiH}}{1-a_{SiH}}\right], & \text{if } x < a_{SiH} \\ 0, & \text{otherwise} \end{cases}$$

where $\alpha_{SiH} = 428.902380$, $\beta_{SiH} = 1.359978$, $\gamma_{SiH} = 2.537884$, $a_{SiH} = 3.2$, and $p = 4.0$.

In order to evaluate the effect of the electric field on the Si-H bond dipole the partial charges of the Si and H atoms were used to calculate the potential energy of the dipole as a function of the bond length. The partial charge of the Si atom used in these calculations is $0.04e$, while the one of the H atom is $-0.15e$, where e is the elementary charge. [73] The Si atom is assumed to lie inside the dielectric whereas the H atom in the vacuum gap, therefore experiencing electric fields of different magnitudes. There are two cases depending on the polarity of the voltage bias: in filled state imaging the tip-induced field and the bond dipole are aligned, while in empty state imaging the field and bond-dipole are anti-aligned. The unperturbed and field-perturbed bond potentials are displayed in the graphs below.

The ground state eigenenergy computed for the unperturbed bond potential was -2.936 eV. In the aligned configuration, for a tip of radius 4 nm the ground eigenenergy shifts to
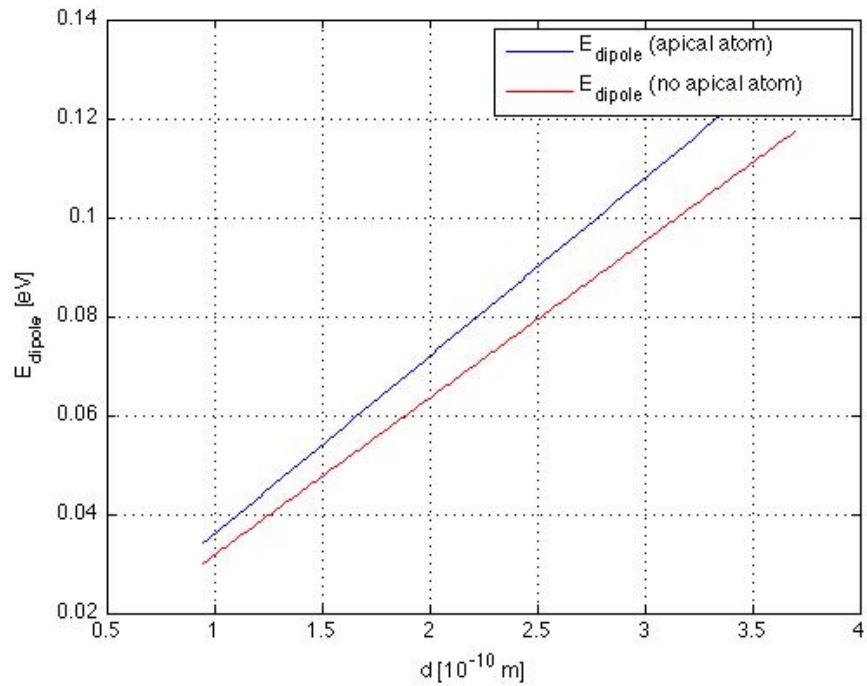
Figure 3.8: Diagram illustrating the linear dependence of the Si-H bond dipole energy upon the Si-H separation for a tip of radius 4 nm. (anti-aligned configuration)

-2.991 eV if the tip terminates in an apical atom and to -2.985 eV if it does not. In the anti-aligned configuration for a tip of radius 4 nm the ground eigenenergy shifts to -2.887 eV if the tip terminates in an apical atom and to -2.881 eV if it does not. The shifts are on the order of up to tens of meV which is consistent with density functional theory estimates of Stark shifts.

These studies [74, 75] have found that modest fields similar to the ones obtained above can lead to the formation of split-off, localized states, which could substantially reduce both coherent and incoherent vibrational energy transfer away from the initially excited site under the STM tip.
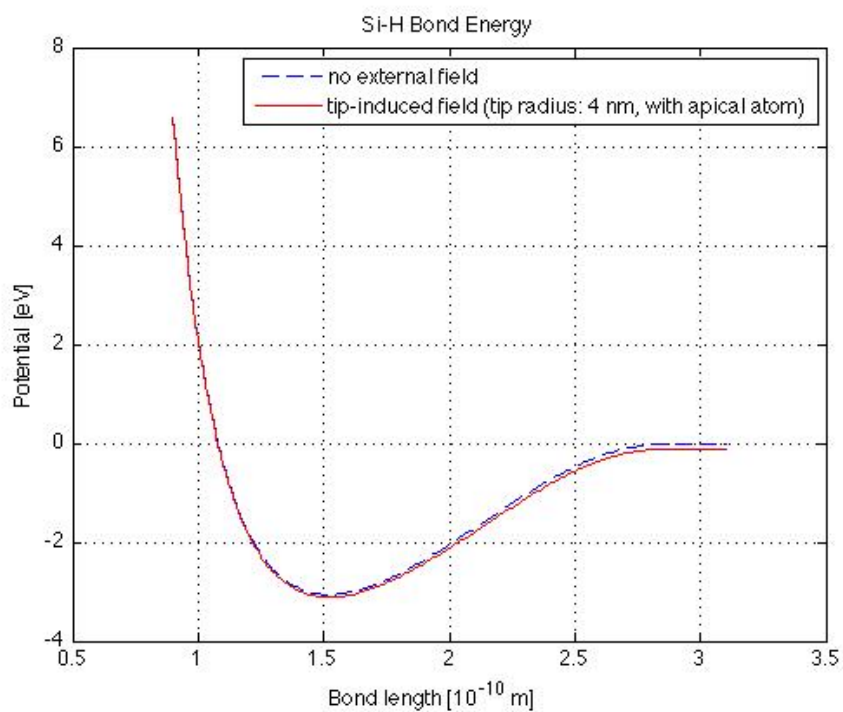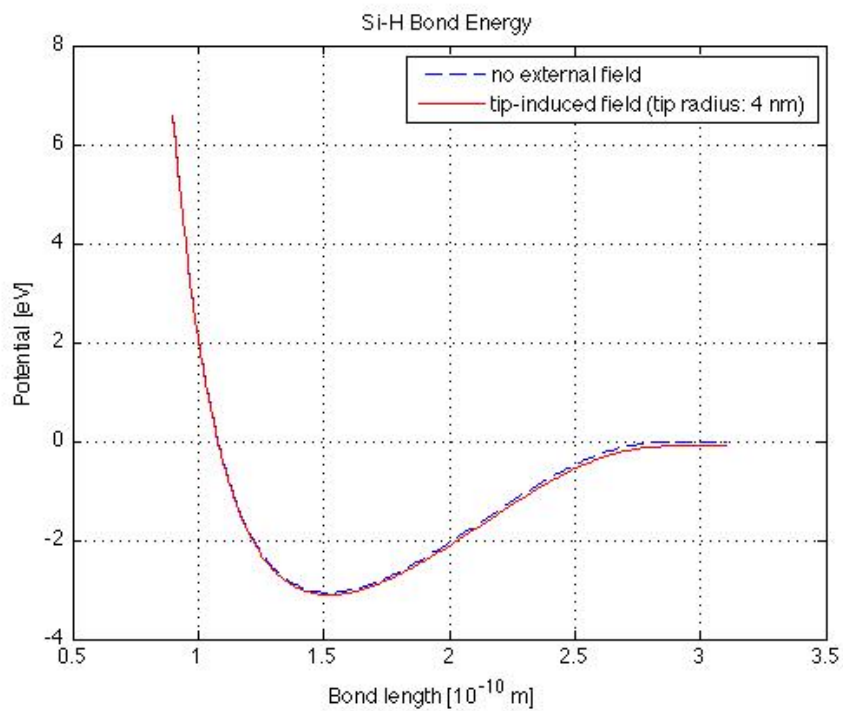
Figure 3.9: Si-H bond energy for aligned bond dipole moment and tip-induced field.
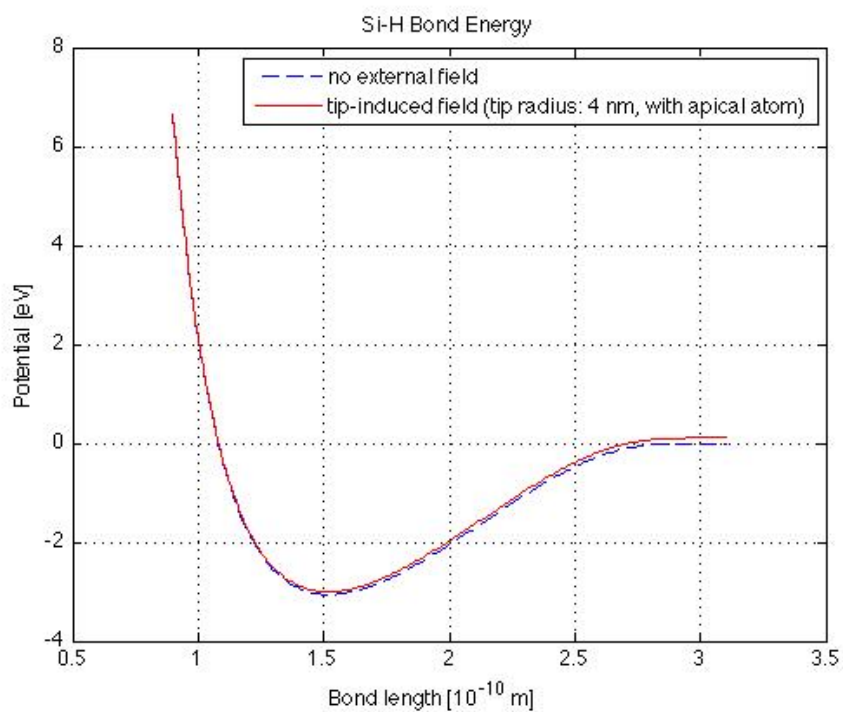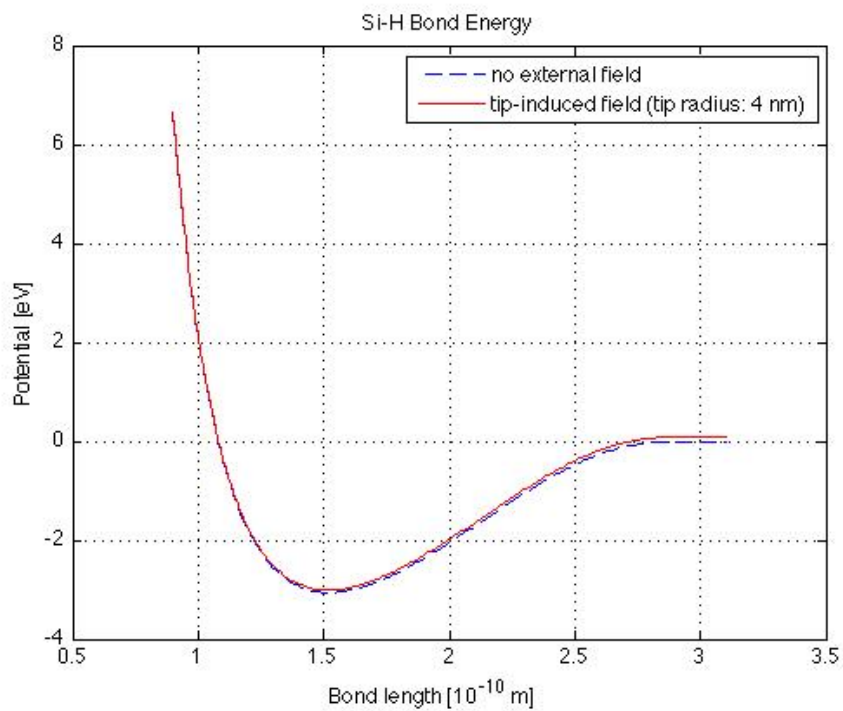
Figure 3.10: Si-H bond energy for anti-aligned bond dipole moment and tip-induced field.

Chapter 4

Field Ion Microscopy

4.1 Historical Overview

The field ion microscope (FIM) is a lensless point-projection microscope that has the capability of resolving individual atoms on the surface of tips terminating in a sharp apex. [76] It was in 1955, considerably ahead of other microscopy techniques, that Müller and Bahadur first observed individual tungsten atoms on the surface of a tungsten tip with an FIM by cooling the tip to 78 K and employing helium as the imaging gas. Müller had invented the FIM four years earlier as an improvement over the field emission microscope (FEM) with regard to spatial resolution. [77] The FEM was developed in 1936, and with it, the handling of large fields such as those required by field emission and field ionization, became possible. [78] While field emission had been observed before, it was only with the advent of field emission microscopy that the behavior of field emitters was fully elucidated. [79]

Field emission is the oldest surface science technique. The first experiments investigating field emission could be viewed as dating back to the time of the Enlightenment. Studies of field emission from metal tips were conducted in the eighteenth century by Johann Heinrich Winkler. Given that by today's standards the vacuum he employed was poor, the phenomena he observed would be more appropriately described as field-enhanced gas discharges.

In the early decades of the twentieth century Julius Edgar Lilienfeld came across field emission while exploring ways to improve his X-ray tubes. He used metal tips for his cathodes and also carefully degassed all metallic parts of his tubes by electron bombardment (procedure utilized in modern UHV technique). At the same time, Franz Rother was performing measurements of the electron current between two electrodes (including field emission tips) reproducibly spaced apart at various distances ranging from hundreds down to 20 nm. He discussed the current-voltage characteristics he obtained in his habilitation.

The pre-quantum-mechanical theoretical explanation of both thermionic and field emission is attributed to W. Schottky. For field emission he hypothesized that under the influence

of the external field a more or less complete bending-down of the rim of the potential trough at the surface occurred. From this he derived an equation for the lowering of the potential wall at the surface by an external field, known as the Schottky image defect.

The difficulties experimentalists were confronted with at the time were non-ideal vacuum conditions leading to emission caused by positive ion bombardment, as well as current fluctuations.

Shortly after Schottky's paper on 'cold and hot electron discharges' Fowler and Nordheim put forward their quantum mechanical theory of field emission. Experimental confirmation of the Fowler-Nordheim theory did follow right away as experimentalists continued research along former lines. It was not until Gustav Hertz assumed directorship of the Siemens Laboratory II in Berlin that experiments on field emission were revived. One of his doctoral students who studied field emission, Erwin W. Müller wrote his dissertation on the energy distribution of the field-emitted electrons in 1936 and published related investigations which eventually led to the creation of the field emission microscope.[*]

4.2   Field Emission

Field emission, as a method of extracting electrons from a solid material, differs from thermionic emission and the photoelectric effect in that, unlike the latter, for which the energy necessary to release the electrons is supplied by phonons or photons, it arises as a result of the surface potential barrier reduction caused by an external electric field. [80]

In the absence of an applied electric field an electron current density given by $j = env$, where n is the electron density, e the electron charge, and v the electron velocity, impinges on the inner surface of a metal. For electrons near the Fermi level an appropriate estimate for j would be about $10^{12} \mathrm{A \cdot cm^{-2}}$. Only a small fraction of this current can escape from the metal, that is, the electrons with sufficient normal energy to overcome the surface tunneling barrier (work function), ϕ. Outside the metal an emitted electron experiences an image force due to the attraction of the induced positive charge. This causes the step-like barrier to take on a softer shape by rounding off the top corner. [80]

In an applied electric field F_0, the potential for an electron located a distance x away from the metal surface takes the form:

$$V(x) = E_F + \phi - eFx - \frac{e^2}{4x} \approx E_F + \phi - eFx - \frac{3.6}{x},$$

---

[*]Last five paragraphs are based on reference [79].

where the energies are in eV, the fields in V/Å, and the distances in Å. The critical distance x_c is defined such that $V(x_c) = 0$. The effective work function is the maximum height attained by $V(x)$ under the influence of an applied field:

$$\phi_{\text{eff}} = \phi - e^{3/2}F^{1/2} \approx \phi - 3.8F^{1/2}.$$

The barrier width Δx for electrons at the Fermi level is given by:

$$\Delta x = \left[\left(\frac{\phi}{eF} \right)^2 - \frac{e}{F} \right]^{1/2}.$$

Tunneling through a barrier occurs when the position uncertainty Δx is on the order of the barrier width. Therefore, given that $\Delta p \approx (2m\phi)^{1/2}$, an estimate for the applied field necessary to produce emission can be obtained using the Heisenberg uncertainty principle, $\Delta x \cdot \Delta p \approx \hbar$, to be $(2m\phi^3)^{1/2}/\hbar e$, which is about 5×10^7 V/cm for $\phi \approx 4.5$ eV. For $F_0 < 10^7$ V/cm the barrier can be considered opaque to the electrons. [78]
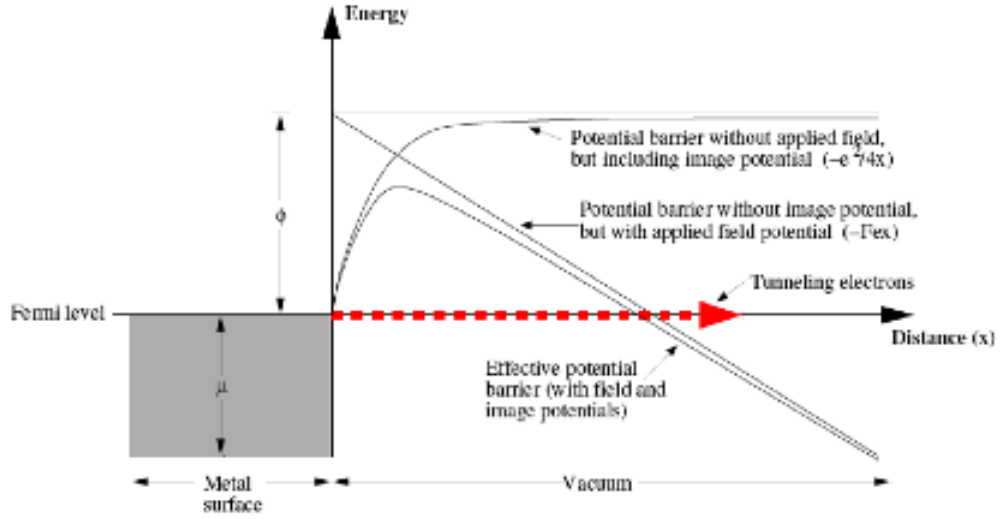
Figure 4.1: Potential diagram for electrons at a metal surface (μ represents the Fermi level). The figure displays: the potential barrier in zero field both in the absence and rounded by the image potential $-e^2/4x$, the triangular barrier produced by the applied field , $-eFx$, and the triangular barrier smoothed out and reduced by the image potential. [10]

Fowler and Nordheim were the first to obtain an expression for the field-emitted current density by integrating the barrier-penetration probability over the distribution of energy for the incident electrons. The Fowler-Nordheim model is predicated on the following assumptions [12]:

A1 the temperature of the metal is 0 K,

A2 the free-electron approximation applies inside the metal,

A3 the surface is smooth and planar,

A4 the potential barrier consists of an image force potential and a potential induced by the applied field.

The barrier-penetration probability, $D(E_x)$, for a free electron gas was calculated by the Kramers-Wentzel-Brillouin method and is given by:

$$D(E_x) = \exp\left[-2 \int_{x_1}^{x_2} \left(\frac{2m}{\hbar^2}\right)^{1/2} [V(x) - E_x]^{1/2} \, dx\right],$$

where E_x is the component of the energy normal to the surface. The tunneling current for a given function $D(E_x)$ is

$$J = \frac{2e}{h^3} \int dp_y \int dp_z \int \frac{p_x}{m} D(E_x) f(p) \, dp_x,$$

where $f(p) = 1/\{1 + exp[(E - E_F)/k_B T]\}$ is the Fermi-Dirac momentum distribution.

In the zero temperature limit and including a first order image corection the equation governing field emission is:

$$J = \frac{e^3}{2\pi h} \frac{(E_F/\phi)^{1/2}}{\alpha^2 (E_F + \phi)} F^2 \exp\left[-\frac{4}{3} \frac{\pi\sqrt{8m}}{eh} \frac{\phi^{3/2}\alpha}{F}\right],$$

where $\alpha = \alpha(F, \phi)$ is a non-dimensional, slowly-varying image correction term, which under practical conditions is 10 to 20% less than unity. Expressed in A/cm^2 the equation above takes the form:

$$J = 6.2 \times 10^{-6} \frac{(E_F/\phi)^{1/2}}{\alpha^2 (E_F + \phi)} F^2 \exp\left[-6.8 \times 10^7 \frac{\phi^{3/2}\alpha}{F}\right].$$

While there is an overlap between the thermionic and tunneling emission regimes such that electrons are emitted both over and through the barrier, the temperature dependence of field emission is weak at moderate temperatures: the current density at room temperatures deviates from the ideal zero-temperature value only by a few percent (about 5% when the temperature increases from liquid nitrogen to room temperature).

Field emission can be employed as an invaluable tool in assessing tip sharpness. For this purpose Fowler-Nordheim plots are use in which the the variation in emission current I with applied voltage V is plotted in the form of $ln(I/V^2)$ versus $1/V$. This leads to a linear plot with a slope proportional to $\phi^{3/2}/F$.

Since the field near a charged conductor is inversely proportional to the radius of curvature of its surface, the electric field at the apex of a tip can be related to the applied voltage as follows:

$$F = \frac{V}{\kappa r},$$

where κ is the field reduction factor. Therefore the relationship between $ln(I/V^2)$ and $1/V$ is given by:

$$ln\frac{I}{V^2} = ln\left[a6.2 \times 10^{-6}\frac{(E_F/\phi)^{1/2}}{\alpha^2(E_F+\phi)(\kappa r)^2} - 6.8 \times 10^7\frac{\phi^{3/2}\alpha\kappa r}{V}\right],$$

expressed in units of A, V, cm^2, eV and cm.

Within an accuracy of a factor of 2 the following formulas can be used to relate the tip field to the applied voltage for the hyperboloidal and paraboloidal approximations, respectively:

$$F = \frac{2V}{rln(4D/r)},$$

$$F = \frac{2V}{2D/r},$$

where r is the tip radius and D is the cathode-anode spacing. Both formulas are valid only for $r \ll D$. However, tips are usually modeled as a cone with a hemispherical tip end of radius r. [80]

In extracting the radius from Fowler-Nordheim plots an average value for the workfunction ϕ can be used, the image forces acting during the tunneling process can be ignored by setting α to 1, and κ can be taken to be about 5 for most common tip geometries with characteristic radii of at least 100 nm, while for extremely sharp tips it can reach values as high as 35. [10]

4.3   Field Emission Microscopy

The field emission microscope, invented by Müller in 1937, is the precursor of the field ion microscope. It is a surprisingly simple instrument made up of a vacuum tube comprising a sharp metallic tip as a sample located a few centimeters (about 10 cm, usually) away from a fluorescent screen. The sample is usually mounted on a filament that can be resistively heated. The fluorescent screen allows the variations in the current density across the field emitted beam to be observed visually. In the configuration above the fluorescent screen would be grounded and a voltage of roughly 1.5 to 3.0 kV would be applied to the emitter. [12]

The image formed on the fluorescent screen is essentially obtained by radial projection of the electrons leaving the emitter surface. The magnification is given by:

$$M = \frac{R'}{\beta R},$$

where R' is the emitter-screen distance, R the emitter radius, and β, the image compression factor, is a constant that depends on the tube geometry and typically has a value of about 1.5 for conventional tip geometries. Typical values for the magnification are about 10^5. [78]

As the emission current is an exponential function of $\phi^{3/2}/F$, the field emission image is sensitive to variations in both the work function and the electric fields across the emitter surface. While the field strength varies across the surface because of variations in the local radius of curvature, a function of the tip shape, on the one hand, and variations in the local topography such as protrusions, on the other, the dominant contrast mechanism in the field-emission image is due to the local work function. The work function depends on the local electronic structure of the surface and hence on the crystallographic orientation of a particular emission area on the tip. Field-emission images can also indicate the presence of adsorbates on the emitter surface by causing a disruption to the local work function in their vicinity via a local redistribution of charge and creation of a dipole. [78]
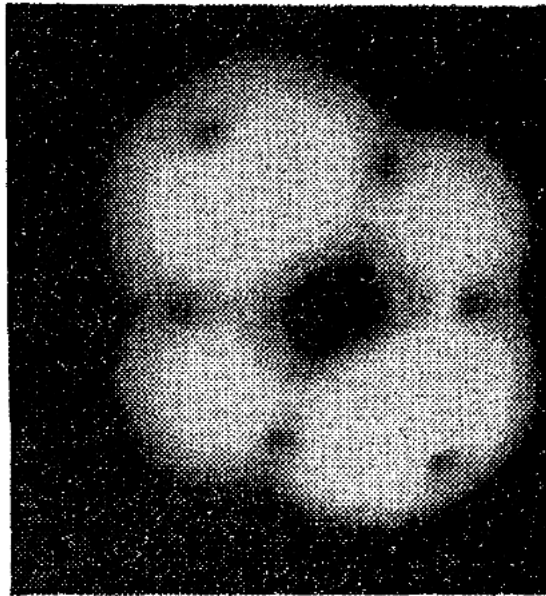

Figure 4.2: Field-emission micrograph of a clean monocrystalline tungsten emitter in low current density, 25 A/cm^2, steady state field emission. The central dark region corresponds to the (110) crystal orientation. [11]

While the absolute work function corresponds to the energy difference between the Fermi

energy and vacuum level and is thus a bulk property, the experimentally measured work function is anisotropic. The anisotropy arises because the experimental work function in fact represents the energy required to move an electron over the surface potential barrier to some point just outside the surface. The value of this work function is affected by the change of the electrostatic potential through the effective dipole distribution at the surface, the strength of which depends on how the electron charge density falls to zero outside the surface. Close-packed surfaces exhibit a slow decay of electron density, which tends to increase the work function, while higher-index planes exhibit a greater spreading of the electron cloud which tends to decrease the work function. In the former case the conduction electron cloud spreads outwards beyond the ion cores giving rise to an inward-oriented dipole (negative side outward), while in the latter the conduction electron cloud becomes denser between the ion cores generating an outward-oriented dipole (positive side outward). [78]

The electrons in a field ion microscope originate mostly from the vicinity of the Fermi level and consequently possess a fairly large kinetic energy which translates into a large transverse velocity component. Additionally, the Heisenberg uncertainty principle imposes a limit on the localization of electrons with finite transverse momenta. Therefore, the two effects limiting the resolution of field emission microscopes are: the spread of transverse momenta of the emitted electrons and the diffraction of electrons passing through the emitter surface. Generally the field emission microscope cannot yield images with lateral resolution higher than 20 to 25 Å. Cooling the emitter does not significantly reduce the lateral velocity of the field-emitted electrons, because electrons are fermions. While for sharp protrusion resolution of up to 10 Å can be attained the field emission microscope cannot resolve atomic detail. [10]

As with other surface science techniques ultra-high vacuum is required for maintaining the surface under investigation free of contaminants for the duration of the experiments. Field emission microscopy has been useful in the study of adsorption phenomena and also in the measurement of work functions for individual crystal planes.

4.4   Field Ion Microscope [†]

The realization that using imaging particles more massive than electrons would substantially increase the resolution of the field emission microscope lead to the invention of the field ion microscope. There had been previous attempts in field emission microscopy to obtain images by field-desorbing adsorbed atoms or molecules upon the application of a positive bias to the emitter. Their success was hindered by the difficulty of replenishing the

---

[†]Based on references: [10, 12, 78]

layer of adsorbed molecules at an appropriate rate.

In 1951, Müller experimented with a slightly modified field emission microscope setup equipped with a palladium tube in order to fill the vacuum tube with hydrogen to a pressure of a few mTorr. Hydrogen was initially chosen solely because of its low sputtering efficiency. So field ion microscopy began when a high positive voltage was applied to the emitter of conventional field emission microscope in the presence of a low pressure of hydrogen. The magnitude of the applied voltage was several times higher in a field ion microscope than was required for field emission as hydrogen requires an image field of about 2.2 V/Å.

The first ion microscopes were not able to resolve individual atoms the attainable resolutions being limited in the 5 to 10 Å range. It was only a few years later, in 1956, when the capability of cooling down the tip was incorporated into the setup and hydrogen was replaced by helium that low temperature images revealed the arrangement of individual atoms on the surface of the emitter with a resolution of 2 to 3 Å. Gas pressures in the range from 10^{-5} to 10^{-3} Torr are employed to ensure that the mean free path does not become too short so that ion-gas atom interactions do not affect the resolution. The achievable resolution increases with decreasing tip temperature. Also, tip mounting assemblies and image intensification schemes that permit the application of a wide range of voltages enable the examination of tips having large radii which may prove advantageous in some cases.

The first field ion microscopes were constructed of Pyrex glasses and lacked image intensification devices. Currently however, almost all such microscopes reside in stainless steel chambers and are made with ultra-high-vacuum components. It is also common to apply a positive voltage to the tip and to have the other electrode grounded. Using a channel plate as an image intensification device renders it possible to use imaging gas pressures as low as 10^{-5} Torr.

In 1954, Inghram and Gomer found that the fundamental process underlying field ion microscopy was field ionization. Drawing on data they obtained from mass spectrometric analysis of the image-forming ions they showed that in the very strong field near the tip surface gas molecules could become ionized without necessarily adsorbing onto the surface. They eliminated the possibility that ion tunneling may be involved because hydrogen and deuterium exhibited similar ionization characteristics. They also observed that with increasing field strength the initially sharply peaked energy distribution of the emitted ions broadened towards the low-energy side which lead them to conclude that ionization was occurring at increasing distances from the tip in higher fields. While Oppenheimer performed detailed quantum mechanical calculations indicating that in a field of about 2 V/Å the electron in a hydrogen atom could tunnel out of the atom and into vacuum, as early as 1928,

it was Inghram and Gomer who first initiated the accepted theory of field ionization near a metal surface, based on the WKB method.

In the absence of an electric field an electron bound to the nucleus of a free atom resides in a potential well of finite width. In order to remove the electron from the well and thus ionize the atom an energy I, equivalent to the ionization energy of the atom is required. In a high electric field the potential barrier is lowered and the electron can tunnel out of the atom. In the vicinity of a conducting surface an additional lowering of the potential barrier occurs owing to image forces which attract the electron to the image of the ion-electron dipole in the conductor. If the atom comes too close to the surface the electron energy level in the atom falls below the Fermi level in the conductor and the tunneling probability is greatly reduced. This is the case because at low temperature almost all the electronic levels below the Fermi level are occupied, leaving few states for the electron to tunnel into. On the other hand, at a critical distance x_c, where the electron energy level matches the Fermi level in the conductor, tunneling will readily occur.

The dependence of the critical distance on I and ϕ is given by the relation:

$$eFx_c \approx I' - \phi - e^2/4x_c + 0.5(\alpha_a - \alpha_i)F^2 \approx I - \phi,$$

where α_a and α_i are respectively the polarizabilities of the atom and the ensuing ion and I' is the effective ionization energy of the atom at x_c. The critical distance is found to lie in the 4 to 8 Å range. However, in such close proximity to the tip surface such a model is overly simplistic.

In the WKB approximation the barrier-penetration probability of an electron is given by:

$$D = exp\left[-\left(\frac{2m}{\hbar^2}\right)^{1/2}\int_{x_1}^{x_2}(V(x) - E)^{1/2}dx\right],$$

where m is the electron mass, $V(x)$ and E the potential energy and the total energy of the electron, respectively. Müller and Badahur showed that the differential ionization probability for the potential, $V(x)$, given below is very strongly field dependent and increases sharply toward the surface of the tip as the short range image forces become important.

The potential energy of the electron at a distance x from the conducting surface is approximately of the form:

$$V(x) = -\frac{e^2}{|x_i - x|} + Fex - \frac{e^2}{4x} + \frac{e^2}{x_i + x},$$

where the first term represents the Coulomb interaction with the positive ion at a distance x_i from the emitter, the potential of the electron in the applied field, and the third and fourth
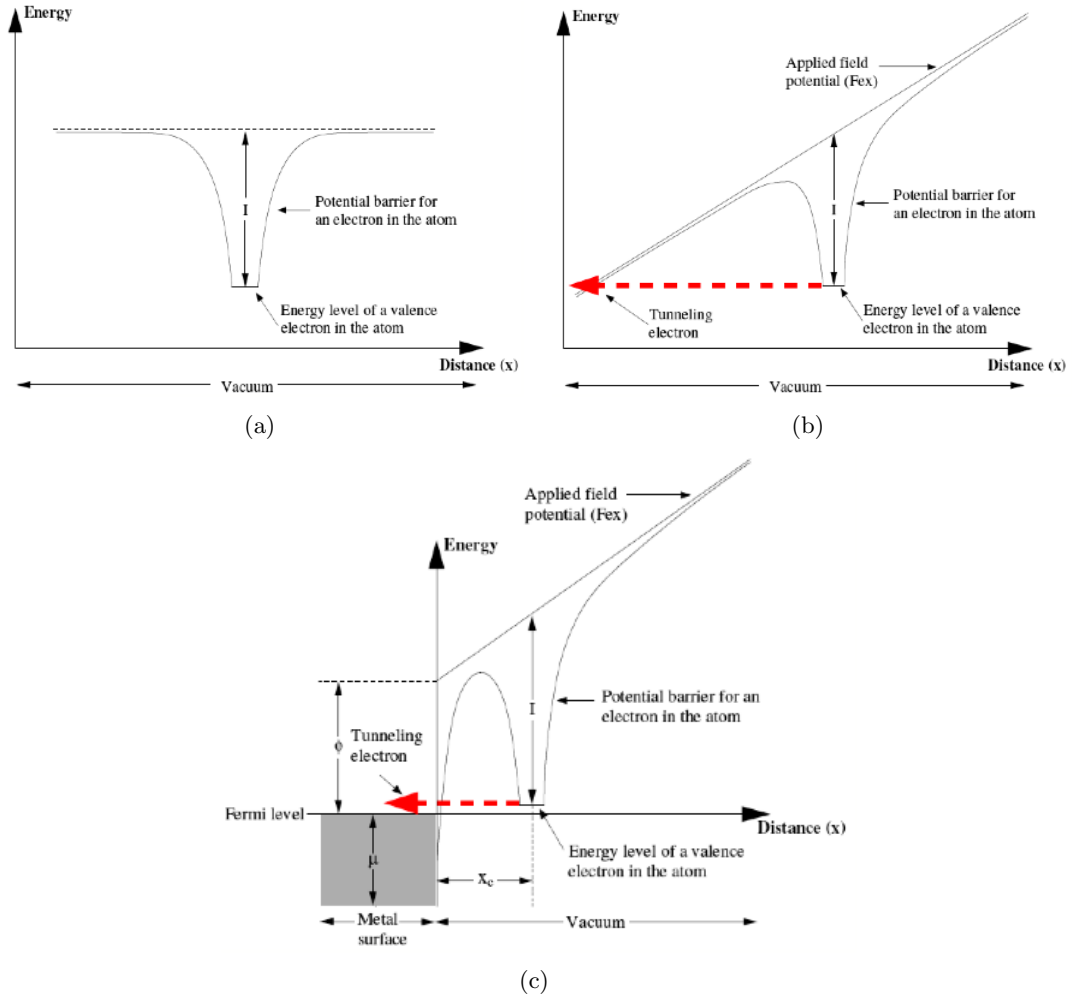
Figure 4.3: Potential energy diagrams for an electron in field ionization; (a) potential for a bound electron in zero field (b) potential in a field F and (c) potential in an applied field in the vicinity of conductor of work function ϕ and Fermi level μ. [10]

terms are the image potentials of the electron and ion, respectively. The field strength for which the sharpest and clearest images are obtained is called the best image field (BIF) and the applied voltage giving rise to it is called the best imaging voltage (BIV). In addition to the imaging gas employed, the BIF also depends on a number of other factors such as: barrier penetration probability, variation of the field across the tip surface, the field adsorption of imaging gas atoms to the surface, the hopping motion of the image gas atoms above the tip surface, and thermal accommodation of the imaging gas atoms to the temperature of the tip.

The strong non-uniform field at the surface of the tip affects the rate of arrival of the gas molecules at the tip: it exceeds the value of the simple kinetic gas flux, $p/(2\pi MkT)^{1/2}$, by a factor which increases slowly with field strength. This is due to the fact that gas atoms

are polarized, and are attracted to the tip surface by a polarization force, $\alpha F dF/dx$. The complicated tip geometry at the atomic level renders the evaluation of the enhancement factor mentioned above very difficult. Experimental evidence has shown that the dominant gas flow comes from flux of low-hopping gas atoms along the shank, a scenario even harder to model theoretically. The threshold field at which ionization starts to take place rises with temperature which implies that the temperature of the tip affects the ionization probability by influencing the velocity distribution of the gas atoms before ionization.

In field ion microscopy the best lateral resolution is achieved if the tip is cooled down to low temperature. Upon arrival at the tip surface under the influence of the electric field the imaging gas atoms have kinetic energy equal to the sum of the thermal energy, which is the thermal energy of the vacuum chamber, and the polarization energy, $1/2\alpha F^2$. The polarization energy is estimated to be on the order of 0.15 eV, 5 times greater than the thermal energy. The substantial improvement in the field ion image resolution upon cooling the tip to 20 K indicates that the kinetic energy of the ions can be reduced by thermal accommodation to the tip and that most image-forming ions have been almost fully thermally accommodated. The coefficient of accommodation a quantifies the exact energy exchange between an incident gas atom and the tip surface. The impact energies characteristic of the field ion microscopy are generally much lower than the binding energies of the tip atoms. Experimentally-derived values of a for helium on clean surfaces are only about a few percent and increase as the ratio of the gas atom mass to surface atom mass decreases. It has also been found that a exhibits a slight dependence on the surface temperature.

Thermal accommodation occurs through a process of hopping: there is a small probability that a gas atom will be ionized on its first pass through the ionization zone above the tip apex and a smaller one still that it will be ionized on its second one, after reflection from the surface. In fact it has been shown that impinging atoms that ultimately escape do so either after the first or second collisions or after a much larger number of collision during which time the atom becomes accommodated to the surface. Whether a reflected atom escapes or becomes trapped between the tip surface and the ionization zone, or into a field adsorption site, depends both on the kinetic energy after reflection and on the direction in which it is reflected. Field induced condensation of imaging gas atoms into a layer coating the apex surface can occur if for a low surface temperature the hopping height of accommodated atoms is below the ionization region.

The average temperature of a gas atom after n hoppings is given by:

$$T_n = (T_0 - T_s)(1 - a)^n + T_s,$$

where T_0 is the initial temperature of the gas atoms and T_s is the temperature of the rebounding atoms if already in thermodynamic equilibrium with the surface. It was found

that it takes over 50 hoppings to cool down the gas temperature below room temperature, and over 100 ones to cool down the gas to the tip temperature if the tip is kept at 20 K.

At best image field most of the imaging ions are formed within a spatial disk of thickness 0.2 to 0.3 Å and of diameter of about 2 Å located about 4 Å above surface atoms in protruding positions. The size of the disk, while not known very accurately, depends on the overlapping integral of the atomic wavefunctions of the image gas atom and of the surface atom. These imaging ions originate from well-accommodated image gas atoms. As the applied voltage is increased above the best image voltage the ionization disks rapidly gain in thickness. As a consequence poorly-accommodated atoms become more likely to undergo ionization which leads to the imaging ions possessing a larger lateral velocity component and their yielding field ion images of lower resolution.

The overall flux of image forming ions produced within the ionization zone is estimated to be about 1000 to 10000 atoms per second. Image contrast arises as a result of the varying ionization rates across the tip surface. Enhancements in the ionization rate can be attributed to effects such as increases in the electronic transition rates and changes in the tip gas supply, both of which are difficult to isolate. Modest variations in contrast can be easily explained on the basis of variations in surface potentials above tip atoms. However, based on the experimental observations of Sweeney and Tsong (in contradiction to previous studies), the high contrast observed in field ion images was ascribed to the fact that field adsorption of helium and neon greatly enhances field ionization rates.

Finally, the image formation mechanism underlying the operation of a field ion microscope can be briefly summarized as comprising the following steps:

1. the inhomogeneous electric field above the tip polarizes the gas atoms,

2. the gas atoms are attracted and accelerated towards the tip surface,

3. the gas atoms thermally accommodate to the tip by random hopping,

4. the gas atoms with low enough kinetic energy remain in the region of high ionization probability,

5. field ionization occurs in a narrow zone at a critical distance away from the tip apex where the atomic level matches the Fermi level of the tip,

6. the positive ions are repelled along nearly radial field lines towards the fluorescent screen.

4.5 FIM Imaging of STM Tips [‡]

The field ion image arises as a result of a geometrical projection of the crystal lattice. Specifically, field ion images can be represented approximately by stereographical projections of nearly hemispherical tips. Therefore identification of crystal planes is done routinely by comparison of such projections with the experimentally derived field ion micrographs.
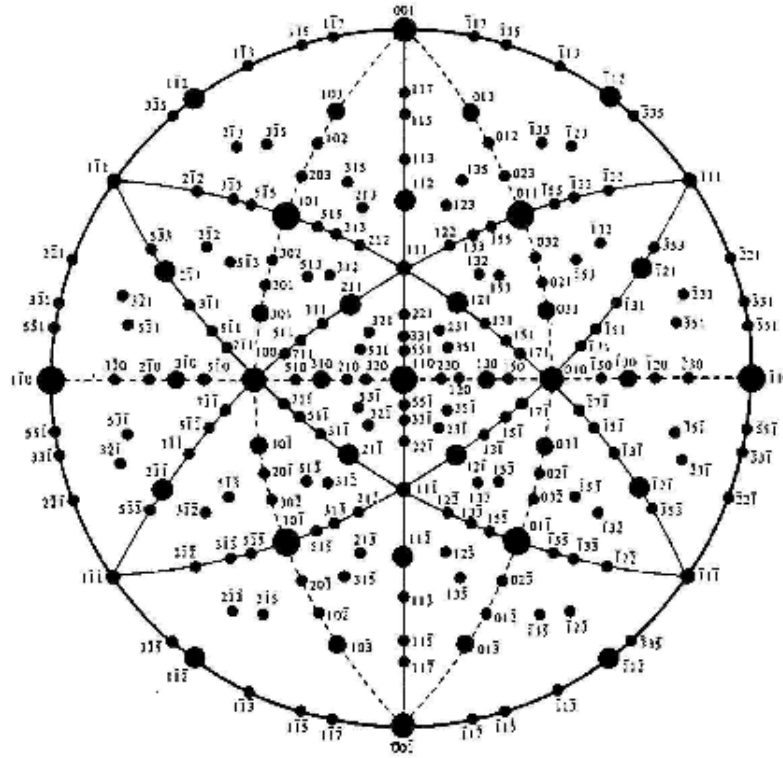
Figure 4.4: Stereographic projection map of a (110) oriented cubic crystal. The facet sizes correspond approximately to those of field ion image of a bcc crystal. [12]

Tips are not truly hemispherical but consist of facets of varying sizes, with the relative sizes of these facets being roughly proportional to the inverse of the density of atomic packing on the plane. Therefore, the magnification across the tip surface is not uniform owing to variations of the electric field in the vicinity of surface atoms pertaining to different crystal planes. Variations in the work function of the surface, which is crystal plane dependent, as well as small changes in the local radius of curvature are also responsible for this non-uniformity. In tungsten, Drechsler and Wolf reported differences in local radii of more than factor of 2. It is also worth pointing out that a fraction of the surface atoms contribute to the image depending on the local density of atomic packing. Only atoms in

---

[‡]Based on references: [10, 12, 78]

63

more protruding positions on the tip surface, such as atoms at step edges, atoms in loosely packed high index planes, as well as clusters and single atoms on flat planes, can be imaged in field ion microscopy. The field is not intense enough for in-plane atoms for them to be imaged because of the higher coordination number of these atoms.

Müller and Young devised a convenient method for estimating the field strength in field ion emission mode. Previously the determination of the field strength was performed in field emission mode by measuring the field emission current density and using Fowler-Nordheim theory. This determination was only accurate to ± 15 %. Müller and Young's approach is predicated on the fact that there is a field strength for which the field ion microscope yields a 'best field ion image', an image that exhibits the best spatial resolution and image contrast. It was found that such a field can be agreed upon consistently to about ± 1 % by different observers. The best image fields for He, Ne, Ar, and H_2 were found to be 4.4, 3.8, 2.2, and 2.2 V/Å, respectively. Field ion energy distribution measurements have verified the accuracy of this method to about ± 5 %.

The determination of the field distribution across the surface of the tip constitutes an extremely complicated problem because of the presence of lattice steps. Such a determination is important in the quantitative interpretation of many field emission experiments, and in calculating ion trajectories in ion probe analysis. Unfortunately, no reliable calculations have been developed that could describe the field distribution above the tip surface.
The structure of a field ion micrograph, while capturing the combined effects of work function, field strength, and curvature variations, can be simply interpreted as follows: the concentric rings correspond to the edge atoms of crystal planes while each set of concentric rings belongs to a crystallographic orientation.

Field ion micrographs enable us to asses the radii of curvature of the imaged tips using the ring counting method developed by Drechsler and Wolf and Múller. In fact the average local radius between any two identifiable planes can be found by counting the number of rings between them. Given two planes (h, k, l) and (h', k', l'), the angle θ between the two crystallographic poles, for a cubic lattice, is given by:

$$cos\alpha = \frac{hh' + kk' + ll'}{(h^2 + k^2 + l^2)^{1/2}(h'^2 + k'^2 + l'^2)^{1/2}}$$

Each ring around the crystallographic pole represents a lattice step. The following formula relates the average local radius of curvature R and the interlayer spacing, s:

$$ns = R(1 - cos\theta).$$

For a cubic lattice, the step height of the (h, k, l) plane is:

$$s = \frac{a}{\delta(h^2 + k^2 + l^2)^{1/2}},$$

where a is the lattice constant, and $\delta = 1$ for a simple cubic lattice. For the bcc lattice

$$\delta = \begin{cases} 1, & \text{if } h+k+l \text{ is even} \\ 2, & \text{if } h+k+l \text{ is odd} \end{cases}$$

For tips made of metals that have the bcc lattice structure, such as tungsten, the average tip radius can be calculated by multiplying the number of plane rings from the (011) plane to the center of the (121) plane by 16.
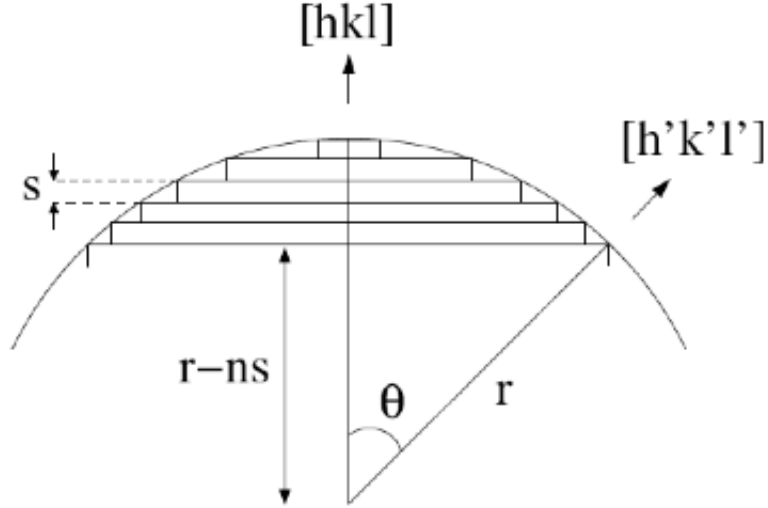
Figure 4.5: Illustration of the ring counting method whereby the local average radius of curvature, R, between two crystallographic poles (h, k, l) and (h', k', l') can be calculated based on geometric considerations. [10]

The resolution of the field ion microscope refers to the smallest distance between two surface atoms that the microscope can still resolve as distinct atoms. Apart from the interaction between the field-ions and gas atoms, which is negligible at appropriate values of the imaging gas pressure, there are a number of other factors which limit the resolution of the field ion microscope, such as [78]:

F1 the extent to which the spatial modulation of the electric field within the ionization zone mimics the underlying atomic structure producing it (this depends on the overlap of tip atom and gas atom wavefunctions),

F2 the extent to which the spatial modulation of the electric field within the ionization zone translates into a corresponding modulation of the emitted field ion current density,

F3 the extent to which the spatial modulation of the field ion density is preserved in the process of transmission from the field ion emitter to the screen.

The first factor is an intrinsic limitation of the technique and cannot be improved. It is intimately linked to the arrangement of atoms in the underlying crystal plane. It is for this reason that small tip radii as well as small facets are more conducive to obtaining high resolution images.

The second factor is favorable to good resolution as the local field strength correlates well to the ionization probability.

The third factor encompasses such aspects as: diffraction effects and the attendant spread in transverse momentum, and the kinetic energy of the imaging ions prior to ionization, which determines the magnitude of the initial tangential velocity of the imaging ions.

The increase in the spot size due to diffraction effects constitutes a consequence of the Heisenberg Uncertainty Principle, according to which the lateral momentum of a particle confined to a small spatial region can only imprecisely be known. The transverse velocity of a particle confined within a distance δ_d above the surface of the tip is about $\hbar/2m\delta_d$. The corresponding resolution takes the form: $[2\hbar r_{tip}/(2meV)^{1/2}]^{1/2}$.
The initial tangential velocity, v_t, of the ions also causes a loss in resolution. The resolution, δ_t, in this case is estimated by assuming that just before ionization the imaging gas atoms are governed by the Maxwell-Boltzmann velocity distribution corresponding to an effective temperature T very close to the tip temperature:

$$\delta_t = 4r_{tip}\beta \left(\frac{E_t}{eV} \right)^{1/2},$$

where E_t is the energy corresponding to the velocity v_t and β accounts for the fact that field ions en route to the screen deviate slightly from the radial trajectories associated with the idealized case of a perfectly hemispherical tip .

Hence, due to the statistical nature of the effects described above, the contributions to the overall resolution add vectorially to give:

$$\delta = \left[\delta_0^2 + \frac{2\hbar\beta r_{tip}}{(2meV)^{1/2}} + \frac{16\beta^2 r_{tip}^2 E_t}{eV} \right]^{1/2},$$

where δ_0 is the resolution limited by the ionization disk and can be approximated to be on the order of an image gas atom radius.

4.6 Field Evaporation

The surface of an electrochemically etched tungsten tip is not smooth and can contain asperities as well as contaminating adsorbates. While macroscopically the field over the surface of the tip can be considered reasonably uniform, at the atomic scale local non-uniformities (enhancements) in the field, occurring at such protrusions, become considerable enough to cause the field evaporation of protruding surface atoms at sufficiently high applied voltages. [78]

Thus, field evaporation (known as field desorption when referring to the analogous process for adsorbed species) consists in the emission of lattice atoms or adsorbates from a surface in the form of ions when the fields reach typical values of a few volts per angstrom. It ensures that the application of appropriate voltages to a conducting surface removes asperities in a self-regulating fashion so as to create a smooth surface over which the image magnification can be viewed close to uniform. [12] Field-evaporated surfaces therefore produce field ion images with fewer distortions as their smoothness improves their ability to radially project field ions. Apart from this field evaporation also constitutes an effective way to create a clean tip by removal of contaminants from the tip apex. In fact, given that field evaporation occurs in a regular fashion, layers of surface atoms can be successively stripped away to remove lattice defects and shape the apex. Of course, removal of atomic layers by field evaporation does affect the radius of the tip, usually resulting in blunting.

It is also noteworthy that in atom probe field ion microscopy it is field evaporation by controlled pulses that enables the chemical analysis of surface atoms and surface layers. The charge-to-mass ratios of the ions are inferred from their flight times and thus chemical identification is rendered possible. [76]

Two theoretical models have been employed most successfully in investigating field evaporation: the image-hump model and the charge-exchange model. According to the image-hump model field evaporation is a thermally activated process whereby a metal ion of charge n overcomes a potential barrier known as Shottky saddle. The potential curve for an ion is obtained as the superposition of the potential of the applied field, $-neFx$, and the image potential of the resulting ion, $-(ne)^2/4x$. The maximum of this potential curve occurs at $-(ne)^{3/2}F^{1/2}$. [12]

In this model the energetics of field evaporation can be derived by considering the following several aspects. In the absence of a field the minimum in the potential energy of an atom corresponds to Λ, the sublimation energy of the atom. Such an energy needs to be expended to remove the atom to free space. Once in the gas phase, the energy needed to

ionize an atom is $\sum_n I_n$, where n is the charge of the ion and I_n is the nth ionization energy of the atom. As the n electrons return to the metal an energy $n\phi_0$ is recovered, where ϕ_0 is the work function of the metal. Therefore in the absence of a field the energy needed for field evaporation would be:

$$Q_0 = \Lambda + \sum_n I_n - n\phi_0$$

Most commonly the atomic crosses the ionic potential perturbed before the maximum and in this case the activation energy for field evaporation is given by:

$$Q = Q_0 - (ne)^{3/2} F^{1/2}$$

In this model ionization is viewed as a gradual process occurring during the evaporation process.

In the charge-exchange model field evaporation is treated as a charge rearrangement process, a transition from an atomic $A + M$ state to an ionic $A^{n+} + M^{n-}$ state. At a very large distance from the surface the ionic curve is higher in energy than the atomic one by $\sum_n I_n - n\phi_0$. [81] The applied field can only slightly lower the atomic curve via the polarization binding while the ionic curve is greatly reduced by $-neFx$. For a field of appropriate strength the two will intersect at an equilibrium distance x_c. Field evaporation occurs when as a result of thermal vibration the surface atom undergoes an electronic transition beyond x_c where the atomic potential energy becomes higher than the ionic potential energy. Thereafter the ion is accelerated away from the surface.

Comparing the evaporation fields for forming n-fold charged ions, Brandon found that for most metals the evaporation fields for doubly charged ions were significantly lower than for singly charged ones. For some highly refractory metals, such as W and Ta, n was found to be as high as 3 or 4. For instance, the formation of W^{3+} requires the lowest field, 5.2 eV.

While there is no solid experimental evidence it is expected that at very low temperatures the potential barrier in field desorption would be more easily overcome by tunneling than by thermal activation. The threshold temperature at tunneling and thermal activation become equally probable was estimated to be as high as 400 K for light atoms (Be) and in the teens for heavier ones. This regime would be identified by the temperature independence of the field evaporation rate. [12] Emerging theories of field evaporation are predicated on self-consistent density functional calculations. While such complicated calculations can yield information about the microscopic forces acting on the surface layer, the electronic charge distribution, and the formation of surface electronic resonances, they often give results in poor agreement with experimental observations.
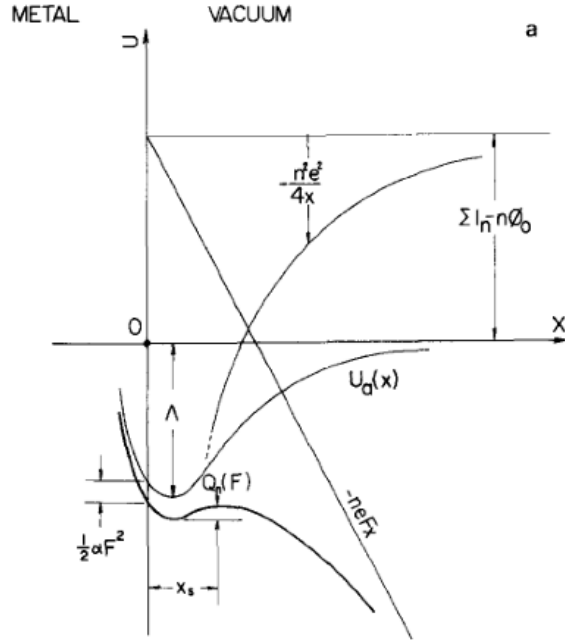
Figure 4.6: Potential energy diagram of a surface atom and ion near a metal for the image-hump model. Under the influence of an applied field an atom comes off the surface and eventually approaches the ionic curve to undergo field evaporation. [13]

4.7 Nitrogen Etching

While field evaporation can be employed for the removal of the oxide layer and other contaminants from the apex of a tip, this process inevitably results in increasing the radius of curvature of the tip, that is, in tip blunting. Nitrogen etching on the other hand relies on the spatially controlled field-assisted reaction of nitrogen atoms with tungsten tip atoms and can be utilized to sharpen the apex of a polycrystalline tungsten tip.

Nitrogen etching of a polycrystalline tungsten tip was first reported in an FIM study by Rezeq et al in 2006. [14] In their experiment the tip was cooled to about 100 K and all the requisite steps were taken to obtain an FIM image of the apex at which point nitrogen was leaked in. As nitrogen can only penetrate the ionizing barrier in low field regions, it preferentially reacts with peripheral tungsten atoms located on the shank of the tip. In the approach presented in the paper by Rezeq et al, a constant pressure of nitrogen (8.4×10^{-8} Torr) was maintained while the applied voltage was gradually reduced while still ensuring a high enough field at the apex to preclude nitrogen etching. Therefore etching progresses along the shank towards the apex of the tip with decreasing imaging voltage, eventually leading to tip sharpening. The difference in ionization potentials between the imaging helium and nitrogen gases render it possible for this process to be monitored in FIM. The rate of bias reduction is important in obtaining a tip with the desired aspect ratio.
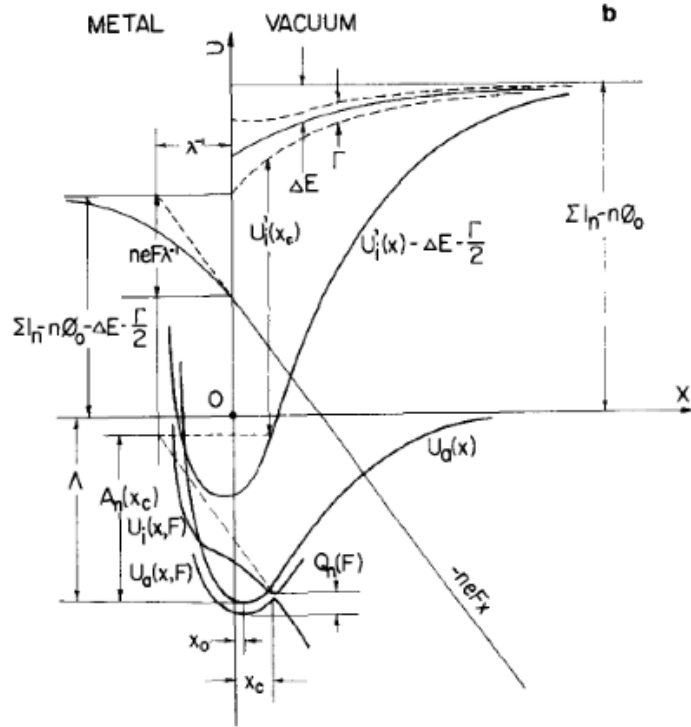
Figure 4.7: Potential energy diagram for the charge-exchange model. U_a represents the atomic potential energy curve in the absence of the applied electric field and U_i the ionic state. The ionic curve is greatly reduced under the influence of the electric field and intersects the atomic curve at an equilibrium distance x_c. This model takes into account the lowering of the ionization energy term by energy level shifts and broadening effects (ΔE, Γ), as well as field penetration effects (λ^{-1}). [13]

The proposed etching mechanism proceeds as follows: under the influence of the electric field the nitrogen molecule adsorbs onto the periphery of the apex where the field is lower and dissociates; nitrogen adsorption engenders the formation of atomic-scale protrusions on the tip; and finally atom removal by field evaporation occurs as a result of the field enhancement in the vicinity of the protrusion.
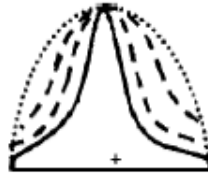
Figure 4.8: Successive tip sharpening stages during nitrogen etching (indicated by the dashed lines); outermost dotted line corresponds to initial tip shape. [14]
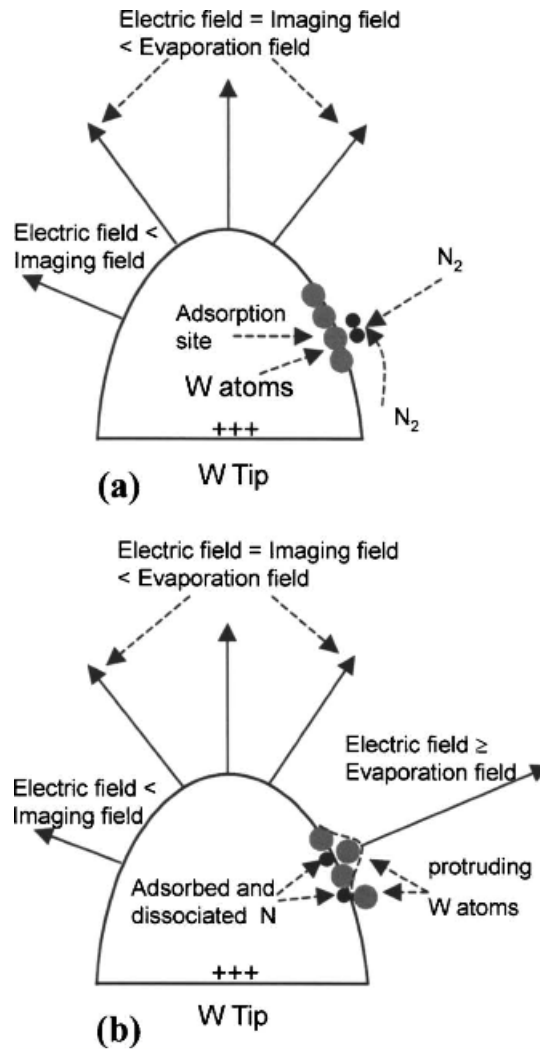

Figure 4.9: Distribution of the electric field on the surface of an FIM tip under imaging conditions: (a) Illustrates that nitrogen adsorption occurs on shank where the field is lower; (b) Field enhancement occurs at a nitrogen adsorption site where an atomic-scale protrusion is created. [14]

Chapter 5

Ultra-High Vacuum System

5.1 Ultra-High Vacuum - Overview [*]

Vacuum technology is the science of vacuum production (by nearly complete removal of gases from a chamber), measurement and manipulation. Its importance lies in the wide range of other technologies it has rendered possible, such as the production of integrated circuits and particle accelerators in high energy physics research.

The development of vacuum technology is closely linked to that of vacuum pumps. Otto von Guericke was the first to successfully modify the design of water pumps for pumping air directly. Pumps with pistons and valves based on Guerickes design lasted until the late nineteenth century having undergone various improvements over the years. By 1910, after a brief return to the more mechanically primitive concept of liquid mercury piston pumps, rotary mechanical pumps were fully developed and very similar to present day designs.

The kinetic theoretical idea of employing the molecular drag effect to pump gases originated in the early 1900s but the full potential of vapor jet pumps was only realized 20 to 25 years later. These pumps exhibited much higher pumping speeds at low pressure and were thus better suited for high vacuum creation.

Just as in the case the vapor jet pumps, the success of molecular pumps was foiled by the absence of suitable technology. Therefore from the first mention of molecular pumps in 1912 it took 45 to 50 years for the development of the high-speed rotating machinery required to produce a reliable device.

While many of the phenomena underlying the operation of ion-getter and sputter-ion pumps had been understood for a long time, they have only been used extensively starting with the 1950s. Gettering pumps rely on a pumping mechanism whereby gases undergo

---

[*]Based on references: [82, 83]

a chemical transformation to combine into a solid while sputtering ion pumps produce pumping action by ionizing gases in order to drive them into a solid surface where they are captured. Their advent is associated with the development of ultra-high vacuum techniques.

Vacuum technology comprises a number of categories of vacuum regimes corresponding to different pressure ranges:

1 Rough Vacuum

Rough vacuum covers a range from 10^2 to 10^{-2} Torr and in this case gas molecules interact with each other in the manner of a viscous fluid. Rough vacuum pumps act as fluid flow pumps as the gases are considered to be in viscous flow, ie there is momentum transfer between particles and the molecular mean free path is much less than the dimensions of channel cross dimensions. The pump-down time is determined by the chamber volume and the pump speed. Rotary vane pumps and scroll pumps can be utilized to achieve rough vacuum.

2 High Vacuum

The high vacuum regime lies between $10-2$ and $10-8$ Torr and is dominated by molecule-chamber wall collisions. The gases are in molecular flow, ie the molecules move randomly, independently of each other as the molecular mean free path (5.1 × 10^3 cm at 10^{-6} Torr) far exceeds the dimensions of the chamber. The molecular density at 10^{-6} Torr is about 10^{10} molecules/cm^3, a considerable improvement over rough vacuum. Under these conditions, assuming a unity condensation coefficient (probability that an impinging particle will be accommodated on the surface), it takes about 2 seconds to attain a coverage of one monolayer of gas molecules.

The pumps required to evacuate gases in molecular flow are statistical capture pumps and therefore do not function by sucking the gases out of the system. They are secondary pumps and need either backing or periodic regeneration by a rough vacuum pump. In this regime the factors influencing the pumping speed are the surface area and material type of the chamber as well as the pump speed.

3 Ultra-High Vacuum

The ultra-high vacuum regime lies within the pressure range from 10^{-8} to 10^{-11} Torr. In this regime the rate of impingement of residual gas molecules upon the surfaces within the vacuum chamber is negligible on the relevant time scales of the experiments. Therefore the most important applications of ultra-high vacuum are related to the requirement of maintaining the cleanliness of the surfaces under study. At a pressure of 10^{-10} Torr it may take up to several hours for a monolayer of contaminants to adsorb onto the surface.

In ultra-high vacuum conditions the rate at which gases enter the system volume (the gas load) by phenomena such as outgassing, diffusion or permeation plays a very im-

portant role in determining the pumpdown time and the ultimate pressure.

The number density of molecules within the chamber is directly proportional to the total gas evolution rate and inversely proportional to the pumping speed. Very high pumping speeds and low gas evolution rates are therefore required to achieve ultra-high vacuum. However, very high pumping speeds are essentially impossible to obtain. As most of the gases at this level of vacuum originate from the walls and surfaces by desorbing off, diffusing out of or permeating through the vessel materials and by being released from the pumps, ultra-high vacuum is attained by reducing leakage and outgassing rates by appropriate surface treatments. Below 10^{-10} Torr the primary source of gas is hydrogen.

While the production of pressures as low as perhaps 10^{-12} Torr dates back to the 1920s the ability to measure them arose only with the invention of the Bayard-Alpert gauge in 1950. [84] Prior to its invention the inability to measure pressures below 10^{-8} Torr using a conventional hot cathode ion gauge was not viewed as a limit on gauge sensitivity but as one on the pumping speeds of diffusion pumps in operation at the time. In the 1930s it was shown that the most significant factor limiting pressure measurements was the X-ray limit, a gauge-design dependent phenomenon. The operating principle of the hot cathode ionization gauge is electron impact ionization. A heated filament (cathode) located axially within a positively charged wire grid (anode) emits a steady flow of electrons. The electrons accelerated past the grid collide with gas molecules to produce ions which are collected by the ion collector. The rate at which ions are formed is directly proportional to the density of molecules within the gauge below 10^{-3} Torr. X-rays are produced when the thermionically emitted electrons strike the grid. The X-rays impinging on the collector photoelectrically eject electrons from it. The measuring circuit cannot discriminate between the photoelectron current and the ion current and yields an erroneous pressure measurement based on the total current. The design of the Bayard-Alpert gauge minimizes the X-ray effect by placing an ultrafine ion collector wire axially within the grid structure and the hot filament outside the grid.

5.2 System Description

The ultrahigh vacuum system employed in the experiments is a customized multi-chamber system dedicated to the investigation of physical and chemical properties of silicon surfaces. The system comprises a load lock, a preparation chamber, an STM chamber, and an FIM chamber.

5.2.1 The Load Lock

The load lock is located above the preparation chamber and is equipped with a vertical magnetically coupled linear/rotary sample transfer drive. A turbomolecular pump backed

by a dry, oil-free diaphragm pump evacuates the load lock to pressures below the sensitivity range of the convectron gauge, that is, below 10^{-4} Torr. Prior to venting the load lock for sample introduction the gate valve separating the turbomolecular pump from it is closed and the chamber is filled with high purity nitrogen to atmospheric pressure. Once the sample is in, the load lock is roughed out by the diaphragm pump to a pressure of 2 to 3 Torr whereafter the gate valve to the turbomolecular pump is opened. Sample transfer to preparation chamber occurs half an hour after the gauge reading bottoms out.

5.2.2   The Preparation Chamber

Sample preparation takes place inside the preparation chamber. It is pumped by an ion pump and a titanium sublimation pump. The pressure is monitored using a Bayard-Alpert hot cathode ionization gauge. The base pressure (pressure reached when the pumping speed equals the gas load) lies within the range 9 - 15×10^{-11} Torr. The chamber is equipped with two variable leak valves (one of which is used for leaking in hydrogen to the desired pressure during the hydrogen termination procedure), a hydrogen cracking filament and a single bellows XYZ manipulator which affords precise control over the movement of the sample as well as its rotational orientation about the Z axis. The Z axis runs through the center of the bellows and it is the motion along this axis that permits sample transfer from the preparation chamber into the STM chamber. The sample holder is equipped with contacts that allow the resistive heating of the sample.

5.2.3   The Scanning Tunneling Microscope Chamber

The STM chamber houses an Omicron STM-1. It is pumped by an ion pump and a titanium sublimation pump. The pressure gauge within this chamber is a cold cathode ionization gauge of the inverted magnetron design. This design best limits the number of discontinuities in the exponential current vs pressure characteristic. The gas density/pressure determination is based on the measurement of the electrical current resulting from the collection of the positive ions created inside the gauge. However, unlike in the hot cathode gauge, in the cold cathode gauge ionization is caused by a circulating electron plasma trapped by crossed electric and magnetic fields. The main advantages of cold cathode gauges consists in the absence of the filament which leads to lower outgassing rates, a lower susceptibility to large pressure bursts and virtually no effect on the dosing gas composition. The base pressure reached inside this chamber is about 4.5×10^{-11} Torr. The chamber is equipped with two variable leak valves for dosing experiments as well as a manually operated, amagnetically coupled device that enables motion in the X, Y, Z axes, known as a wobble stick. It transmits simple hand movements through the vacuum wall such that its end is able to reach various positions in an action cone. The wobble stick in this system terminates in pincer grips used to attach and detach samples when transferring them from the preparation chamber to the STM chamber. Inside the chamber a carousel for sample storage is also

located.

5.2.4 The Field Ion Microscope Chamber

The FIM chamber is located above the STM chamber and is continuously pumped by a turbomolecular pump. The base pressure attained in this chamber is 4 - 5 $\times 10^{-10}$ Torr. It is equipped with three leak valves to control the admission of helium, nitrogen and other gases into the chamber, a residual gas analyzer, a linear motion feedthrough terminating in copper contacts for resistively annealing the tip, as well as a vertical magnetically coupled linear/rotary transfer drive terminating in a tip holder. The chamber also houses a microchannel plate and a phophorus screen positioned in front of the view port for obtaining field ion images. In the FIM configuration the linear/rotary transfer drive is almost entirely retracted with the tip facing the MCP 5 cm away from it.

5.2.5 The Pumps [†]

Diaphragm Pumps

Diaphragm pumps fall into the category of positive displacement coarse vacuum pumps. They do not contain any liquids either as lubricants or as motive fluids which eliminates the possibility of oil backmigration and thus hydrocarbon contamination. The chief advantage of these pumps is the complete separation of the driving mechanism from the pumping spaces where the gas flows. Diaphragm pumps are very similar to piston pumps. Within a cycle the motion of the piston attached to a diaphragm causes the volume of the pumping chamber to increase, drawing gas in, and subsequently decrease, expelling the gas. The leaf valves at the inlet and at the exhaust are actuated by pumped gas pressure differences. Therefore, when gas pressures fall below the actuation threshold of the valves the pumping action ceases. Depending on their design (number of pistons) such pumps can achieve ultimate pressures of a few Torr.

Turbomolecular Pumps

Turbomolecular pumps are essentially axial-flow compressors designed for pumping rarefied gases. Just like axial-flow compressors, turbomolecular pumps consist of alternating bladed rotors and stators. The basic pumping mechanism employs rotor/stator pairs to successively compress gas to the level of fore-vacuum pressure at the exhaust. Turbomolecular pumps can be viewed as momentum transfer devices whose rotating inclined blades impart momentum to the gas molecules in order to accelerate them in the downstream direction. The speed of the blades has to be comparable to the thermal speed of the gas in order that such pumps be effective. However this requirement does not constitute a drawback as the symmetric design ensures balanced forces. Stators have the function of redirecting, straightening or

---

[†]Based on reference [82]

adjusting the flow to enhance the efficiency of the following rotor. Under molecular flow conditions randomizing chambers could, in principle, replace rotors however, that would result in an impractical device. The high discharge pressures achieved by turbomolecular pumps have rendered possible the use of small, oil-free diaphragm pumps as backing pumps. Other advantages include effective pumping for all gases (hydrogen provides the ultimate pressure limitation), good response to transient overloads (inlet stages may be affected while lower ones would still be functioning properly), production of many degrees of vacuum and considerable facility of operation.

The Ion Pumps

The ion pump was invented in the late 1950s at Varian Associates and operates on the principle of the Penning cold-cathode discharge, first observed in 1937. It is a type of capture pump, namely it traps the pumped ion molecules within the pump body. It has no moving parts (no lubrication is required) and therefore is vibration and contamination free. A significant advantage is that a bake-out regenerates the ion pump to the initial conditions. In its most common configuration it comprises an array of cylindrical anode cells placed between parallel cathode plates made of titanium, and a magnet. A cloud of spiraling electrons confined within the anode cells by an electric field and a coaxial magnetic field (1000 - 2000 G) ionizes residual gas molecules by collision. The resulting ions accelerate out of the anode cells towards the cathode plates where they either react with the titanium or are buried. Upon reaching the cathode plates the gas molecules also sputter some titanium atoms onto nearby surfaces thereby producing a gettering film and cause the release of secondary electrons which are incorporated into the electron cloud inside the anode cells. The sputtering rate depends on the ratio of the mass of the impinging molecules to the mass of the cathode material. For hydrogen the sputtering rate of titanium is negligible. Unlike other ions, hydrogen ions diffuse deep into the material beyond just a few atomic layers below the surface and are permanently trapped there. In the diode configuration a positive voltage (3 - 7 kV) is applied to the anode whereas in the triode one the voltage polarity is modified so that the anode array is grounded and the cathode plates, which are in this case constructed of titanium strips, operate at negative voltage. The latter configuration shifts the balance of sputtering, ion burial and re-emission such that stable noble gas pumping can be maintained thus reducing the risk of argon instability. This is achieved by increasing the effect of the neutral atoms reflected from the cathode due to grazing incidence angles which favor a higher reflection probability as well as sputtering yield. The argon instability occurs when argon, a chemically neutral gas pumped by burial only, is re-emitted by sputtering action. The resulting pressure rise in turn causes more sputtering and thus more argon re-emission leading to pressure bursts of up to 10^{-4} Torr at which point the electrical discharge changes mode and the argon gets slowly pumped to other areas of the pump. Later on the discharge reverts to the initial mode and the pressure falls back rapidly to the system base

pressure. The operating pressure of ion pumps is in the range below 10^{-5} Torr and the pumping speed depends on the pressure. The maximum pumping speed is reached at about 10^{-7} Torr. The base pressure is only limited by the desorption rate of trapped molecules.

The Titanium Sublimation Pumps

The titanium sublimation pumps (TSP) in our vacuum system are mounted inside the ion pumps. They are simple in both construction and operation and consist of filaments of a molybdenum-titanium alloy which preferentially sublimate titanium. To produce pumping action the filaments are heated electrically by passing a 48 A current through them until titanium sublimates from their surface into the vacuum. The fresh titanium deposits onto the nearby areas and forms a thin layer of stable compounds with the getterable gas atoms and molecules that strike the surface. Inert gases cannot be pumped by chemical gettering. The pumping speed is maximum when a monolayer of titanium is maintained on the pumping surface. However, in a UHV environment a complete film of fresh titanium takes time to reach saturation, therefore periodic sublimation should be employed for efficient use of the filaments. Typically a monolayer of titanium is evaporated in about 2 minutes. The pumping speed of TSPs depends on such factors as system temperature, the conductance of the system, the gas species as well as the area/geometry of the system. The location of TSP filaments within a system is essential; they should be mounted such that titanium can deposit on a large area outside the line-of-sight to samples or anything titanium may damage. Also, filaments must be thoroughly degassed prior to operation in order to reduce the amount of gas released when the sublimator is heated.

Chapter 6

Experimental Procedure

6.1   Sample Preparation

Once the sample holder bearing the silicon crystal is inside the preparation chamber the sample holder outgassing procedure starts: for several hours (usually overnight) the sample is resistively heated to about 600° C, below the silicon oxide, SiO_2, sublimation temperature (the oxide layer protects the crystal from contamination). When the pressure in the chamber recovers the sample is allowed to cool for about an hour whereafter the sample is repeatedly flashed for about 5 seconds at gradually increasing temperatures up to 1200° C in order that the pressure in the chamber not exceed 10^{-9} Torr during any of the subsequent flashes. If a pressure burst above 10^{-9} Torr should occur the flash should be aborted. The goal is to further degas both the holder and the sample such that the pressure stays below 5×10^{-10} Torr during a 5 second flash at 1200° C. The hydrogen cracking filament is at this point also degassed for about 20 minutes. As a precaution the sample is turned away from the filament. Having thus ensured that contaminants would not be released during the actual hydrogen termination procedure one finds the current settings required for the sample to go through the following temperature cycle: 1200° C for 5 seconds, cooling down to 290° - 300° C and remaining at this temperature for two minutes. This is done because during the termination procedure the glow from the hydrogen cracking filament renders infrared pyrometer temperature readings unreliable. Following the determination of the current settings hydrogen is leaked into the chamber to 10^{-6} Torr and the filament is turned on. The sample is left facing the filament for about 2 minutes and then it is flashed to 1200° C for 5 seconds, allowed to cool down to 290° - 300° C and maintained at this temperature for 2 minutes. As soon as the 2 minutes are up both the current source and the filament are turned off and the leak valve is closed. When the sample has cooled down and the base pressure has gone down considerably, the sample can be transferred to the STM chamber.

6.2 Tip Electrochemical Etching Procedure

The scanning probes employed in the experiments presented in this thesis are tungsten tips obtained by electrochemical etching. Prior to etching the wire is thoroughly cleaned with ethanol and subsequently dried with compressed nitrogen. The tip etching station/apparatus basically consists of an electrolytic cell. The polycrystalline tungsten wire of diameter 0.8 mm and a stainless steel counterelectrode (cathode) are dipped into an electrolyte, in this case an aqueous solution of NaOH 1 - 2 M. The wire is mounted on a translation stage for precise control over the length of wire immersed in the solution. For etching, a circuit is used to apply a dc voltage of about 4 - 10 V to the tungsten wire. Tips are usually pre-etched for about one minute with a larger fraction of the tip being immersed in the solution so as to remove the oxide layer. An etching current on the order of a few mA is established between the two electrodes, with the etching being confined about the air-electrolyte interface portion of the wire. The overall electrochemical reaction is:

$$\text{Cathode: } 6H_2O + 6e^- \rightarrow 3H_2(g) + 6OH^-$$

$$\text{Anode: } W(s) + 8OH^- \rightarrow WO_4^{2-} + 4H_2O + 6e^-$$

$$W(s) + 2OH^- + 2H_2O \rightarrow WO_4^{2-} + 3H_2(g)$$
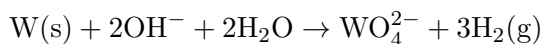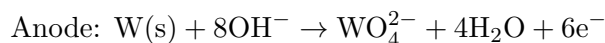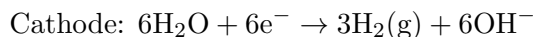
The etching takes about 10 - 15 minutes. At the liquid-air interface about the immersed tip the liquid rises to form a concave meniscus due to surface energetics. It is to this region that the etching is confined. The shape of the meniscus plays an important role in determining the aspect ratio as well as the shape of the tip. The meniscus should be monitored during the etching process so as not to drop too much. The underlying process is known as anodic dissolution of the electrode. It proceeds at different rates along the immersed section of the tip because of the existence of a concentration gradient: the concentration of the hydroxide anions, OH^-, is higher in the bulk solution and decreases towards the top of the meniscus. It is also noteworthy that under gravity the tungstate anions, WO_4^{2-}, which would otherwise hinder the process, flow down. As a result of the gradient the etching rate is higher in the bulk where the tip is to be formed. [28, 85] Therefore necking occurs and the immersed portion of the wire drops off when its weight exceeds the tensile strength supporting it. It is essential that cutoff take place immediately after the lower portion drops off. Thus, the electrochemical etching circuit applying voltage to the tip is designed to have a fast cutoff time, that is, to respond as fast as possible to the change (drop) in current density at the time of drop off by turning the circuit off. [85] The sooner the etching current breaks off the more likely the tip end will be sharper.

Hydroxide anions are consumed during etching, so for the etching process to remain effective the electrolyte concentration should be maintained at the appropriate level by regularly changing the solution. As the weight of the wire affects the drop off it is best that its length be only a few mm. Also, a cylindrical glass shell enclosing the tip and placed between the two electrodes protects the meniscus from the perturbing effect of the bubbling hydrogen.

After etching the tip is coated in a layer of oxide, WO_3, and other organic contaminants which are removed in vacuum, in the FIM chamber by annealing the tip to bright orange, about 800° C. At this temperature the following reaction takes place to form volatile WO_2:

$$2WO_3 + W \rightarrow 3WO_2 \uparrow .$$

6.3   Tip Electron Bombardment Technique

After having been annealed the tip is turned towards the linear motion feedthrough equipped with a tungsten filament. The filament is appropriately degassed such that the increase in chamber pressure is marginal, on the order of a few nTorr. Thereafter the filament is brought within 3 - 5 mm of the tip. A positive voltage of 500 V is applied to the tip and the current running through the filament is gradually increased to approximately 1.2 A. The goal is to have the electrons thermionically emitted from the incandescent wire bombard the tip and thus remove contaminants.

If the pressure should rise above 1×10^{-7} Torr the filament current should be immediately shut off. It usually requires several attempts to attain the desired current setting.

Once the pressure stays below 1×10^{-7} Torr the procedure above should be performed repeatedly, sustaining the current setting for about 20 - 30 seconds each time, until the increase in chamber pressure during electron bombardment is minimized.

6.4   Field Emission

The tip is transferred to the STM chamber and placed in the scanner for this procedure as field emission will occur into the sample. Using coarse approach the tip is brought as close as possible to the sample; the approach speed is progressively lowered as the tip moves closer to the sample in order to prevent tip crashes. The reflection of the tip in the sample is a good way of estimating the tip sample separation. When the tip is very close to the sample the approach parameters are set (40 pA for the set point current and -2.0 V for the

sample bias) and auto-approach is started. After the tip has landed it is retracted about 10 coarse steps from the sample, which is approximately 3 microns.

The negative voltage applied to the tip using a high voltage power supply is gradually increased while monitoring the sample current on an oscilloscope. The aim is to achieve a stable field emission current of about 100 nA. For a reasonably sharp tip the magnitude of the voltage required should not exceed 500 V. Initially, significant fluctuation in the emission current, indicative of remnant tip contamination, can be observed but with time the emission characteristics may improve and therefore the voltage should be changed accordingly so as to maintain the desired emission current. Steady emission current indicates that the tip is clean and ready to use.

It has been observed that for noticeable improvements in tip imaging characteristics the field emission current should be sustained for a time frame on the order of a few hours. Sometimes poorly imaging tips have considerably improved after field-emitting overnight. A stable field emission signal and a lowering of the voltage required to extract a certain current constitute hallmarks of a promising tip with superior imaging characteristics in terms of reliability and image sharpness.

6.5   Field Ion Imaging

After the tip is properly aligned for field ion imaging in the FIM chamber the voltage applied to the phosphor screen is set to about +2400 V, and the voltage drop across the microchannel plate is set to about 1400 V such that the front plate is at negative bias and the back one is grounded, in order to obtain the desired gain.

At this point the residual gas analyzer mass spectrometer is turned on to monitor the gas content and gas partial pressures while helium is leaked into the chamber to about 5×10^{-6} Torr via the variable leak valve. To ensure that field ion imaging does not contaminate the tip, helium is passed through a liquid-nitrogen-cooled cryotrap and the gas line itself is pumped overnight with a turbomolecular pump.

When the imaging gas pressure has reached the desired value a high voltage power supply is used to gradually increase the positive bias applied to the tip. Initially contaminants are field desorbed from the tip in a series of bright bursts. As soon as the crystal is exposed one can resort to careful field evaporation if the field-ion image exhibits undesirable non-uniformities and protrusions. Thereafter the best image voltage is sought to better assess the structure of the apex.
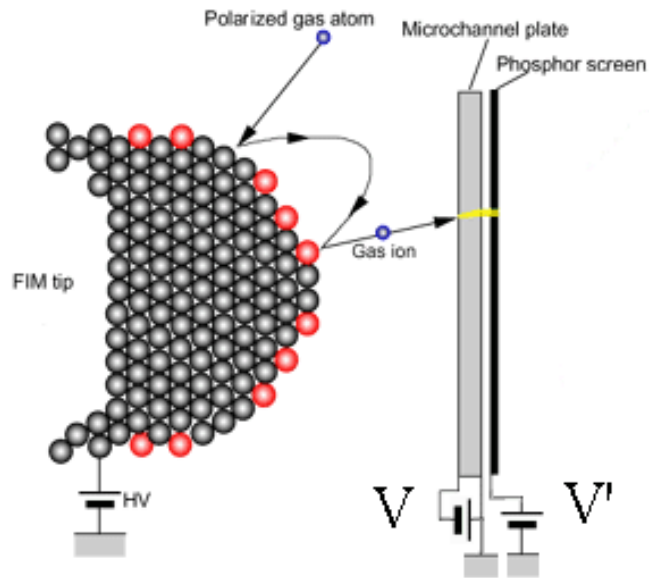
Figure 6.1: Schematic diagram of an FIM. The front of the microchannel plate is negatively-biased at $V \approx -1400$ V, while the back is grounded, and the phosphor screen is positively-biased at $V' \approx 2400$ V. (Adapted from [15])
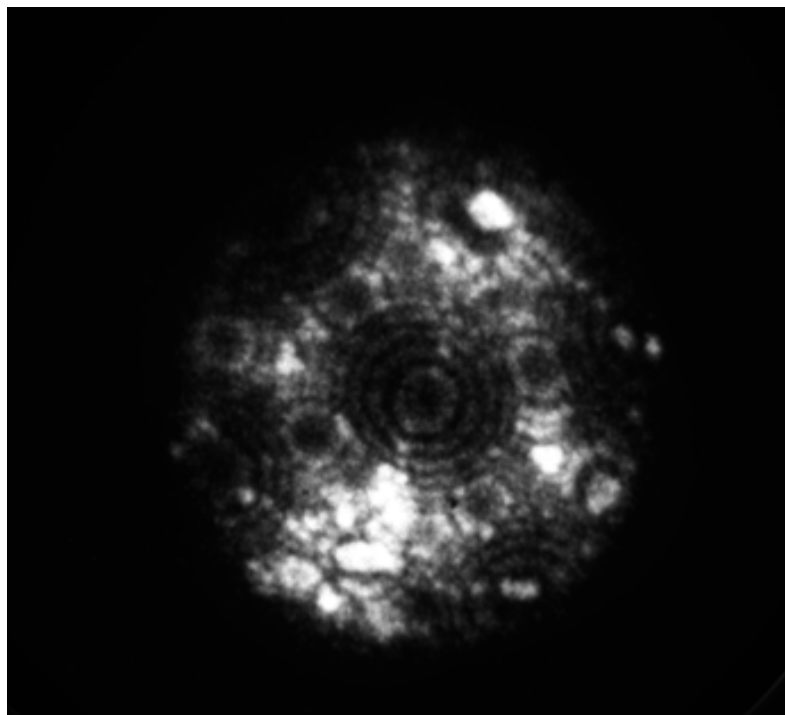

Figure 6.2: Averaged field-ion image of a (110) oriented bcc tungsten tip apex at room temperature.

Chapter 7

# Scanning Tunneling Microscopy Data

This chapter presents a collection of typical scanning tunneling images obtained in the course of the preliminary attempts at hydrogen desorption from H:Si(100)-(2 × 1) performed in this study.

Initially, once the tip has come successfully (without crashing) into tunneling contact with the sample, and unless the tip yields high resolution images in a stable fashion from the outset, one resorts to harsher, tip-conditioning scanning parameters such as set point currents in the 150 - 300 pA range and voltage biases in the 3.0 - 5.0 V range in order to improve the imaging characteristics of the tip. Typical parameters that ensure a safe approach are low set point currents of about 40 pA and voltage biases of about 2.5 V. As soon as the scanning tip becomes reasonably stable and before proceeding to hydrogen desorption one usually seeks to ascertain the quality of the sample under investigation by collecting images of larger areas (about 100 × 100 nm) at various voltage biases and various locations within the scanning range. The 80 × 80 nm grayscale micrographs of medium As-doped, n-type H:Si(100)-(2 × 1) in Figure 7.1 illustrate such images. In occupied state imaging one cannot always unequivocally identify dangling bonds, which appear as bright spots, as other features may image very similarly. However, in unoccupied state imaging dangling bonds exhibit dark halos around their central bright spots and can therefore be easily identified with certainty. In Figure 7.1 a comparison between images (a) and (b) reveals which bright spots are in fact dangling bonds. The area in Figure 7.1 comprises two terraces separated by a monatomic step approximately along the diagonal of the image. Generally steps can serve as useful reference features for locating smaller features within the scanned area. As can be seen, the dimer rows of the two terraces are perpendicular to each other. The sample in Figure 7.1 also exhibits dimer vacancies, which image as dark spots (depressions), indicative of low levels of nickel-contamination.

Attempts at desorption were performed both by applying current and voltage pulses as

well as using feedback-controlled lithography (FCL), both of which require high currents. While in the first technique the duration of the pulse is preset as are the other parameters, in FCL both the tunneling current and the tip position are monitored during patterning and the desorption parameters are maintained until a desorption event occurs. A desorption event (the sudden increase in the local density of states due to depassivation) is easily detectable through the response of the feedback loop which acts to reestablish the set point value and thus the desorption parameters can be stopped. [86] Typical values for the desorption current used in this study are about 1 nA, while typical voltage biases are about 2 - 3 V. The images in Figure 7.2 are 40×40 nm grayscale STM migrographs of medium As-doped, n-type H:Si(100)-(2 × 1). Image (a) was collected before hydrogen desorption attempts using FCL were made and image (b) shows the dangling bonds created as a result of those attempts. Red dots indicate the approximate locations where desorption current and voltage parameters were applied. As can be seen, while at all sites the same desorption parameters were employed multiple as well as single dangling bonds resulted and one attempt was not successful.

Finally, Figure 7.3, an occupied state, 80×80 nm grayscale STM micrograph of medium B-doped, p-type H:Si(100)-(2 × 1), captures a fortuitous event, namely spontaneous tip-induced hydrogen desorption. While the mechanism causing such an event is unknown, it is speculated that a temporary atomic rearrangement of the tip apex as well as the adsorption of a molecule onto it may catalytically favor hydrogen desorption. The desorption of the hydrogen line in the upper part of the image occurred only during part of a line scan as the length of the line demonstrates, thus indicating the unstable nature of the responsible apex configuration.
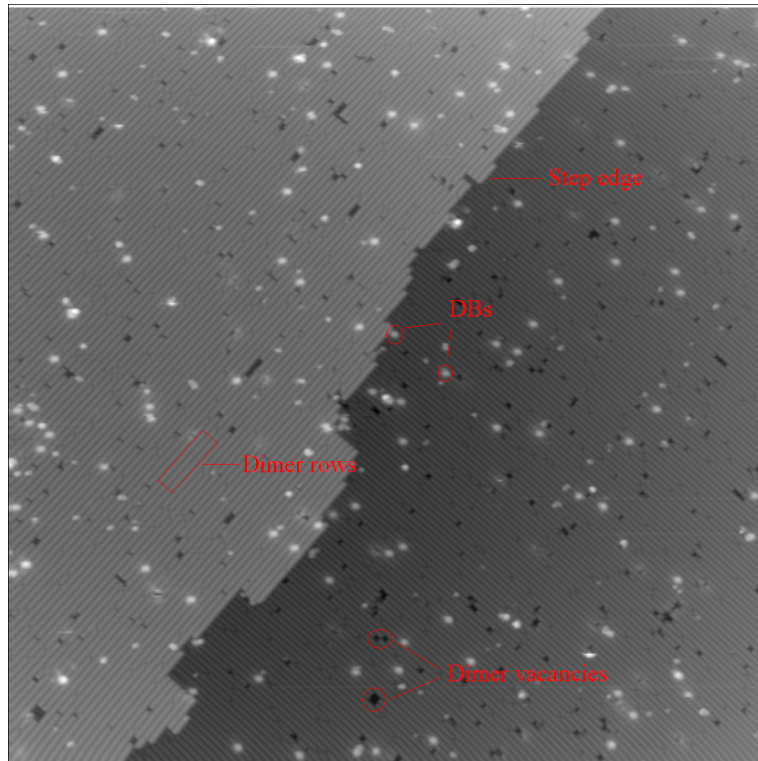
(a)
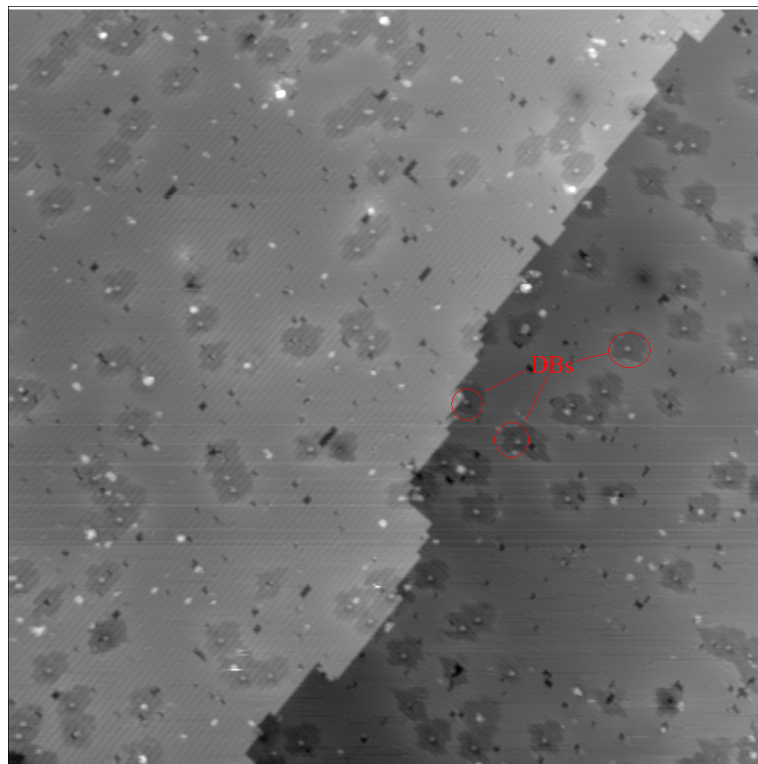
(b)

Figure 7.1: 80×80 nm grayscale STM micrographs of medium As-doped, n-type H:Si(100)-(2 × 1) in: (a) occupied state imaging (−3.0 V, 100 pA), (b) unoccupied state imaging (2.0 V, 80 pA). In (a) DBs appear as bright spots while in (b) DBs also exhibit dark halos around them.
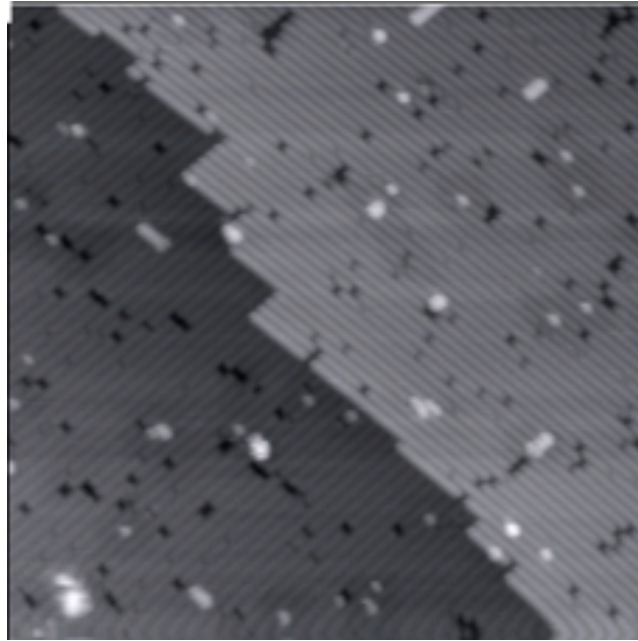
(a)
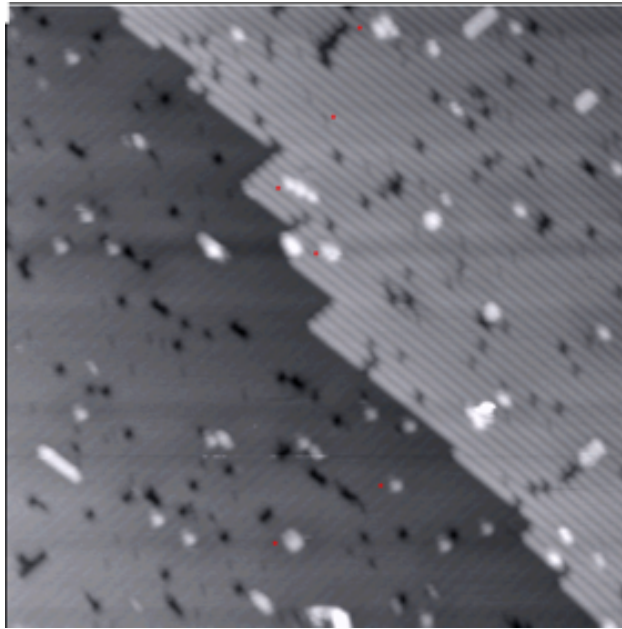
(b)

Figure 7.2: 40×40 nm grayscale STM migrographs of medium As-doped, n-type H:Si(100)-(2×1) in: (a) unoccupied state imaging (2.5 V, 80 pA), (b) occupied state imaging (-2.7 V, 110 pA). The red dots in (b) indicate DBs created by the application of 1 nA current pulses, the average duration of which was about 0.7 s.
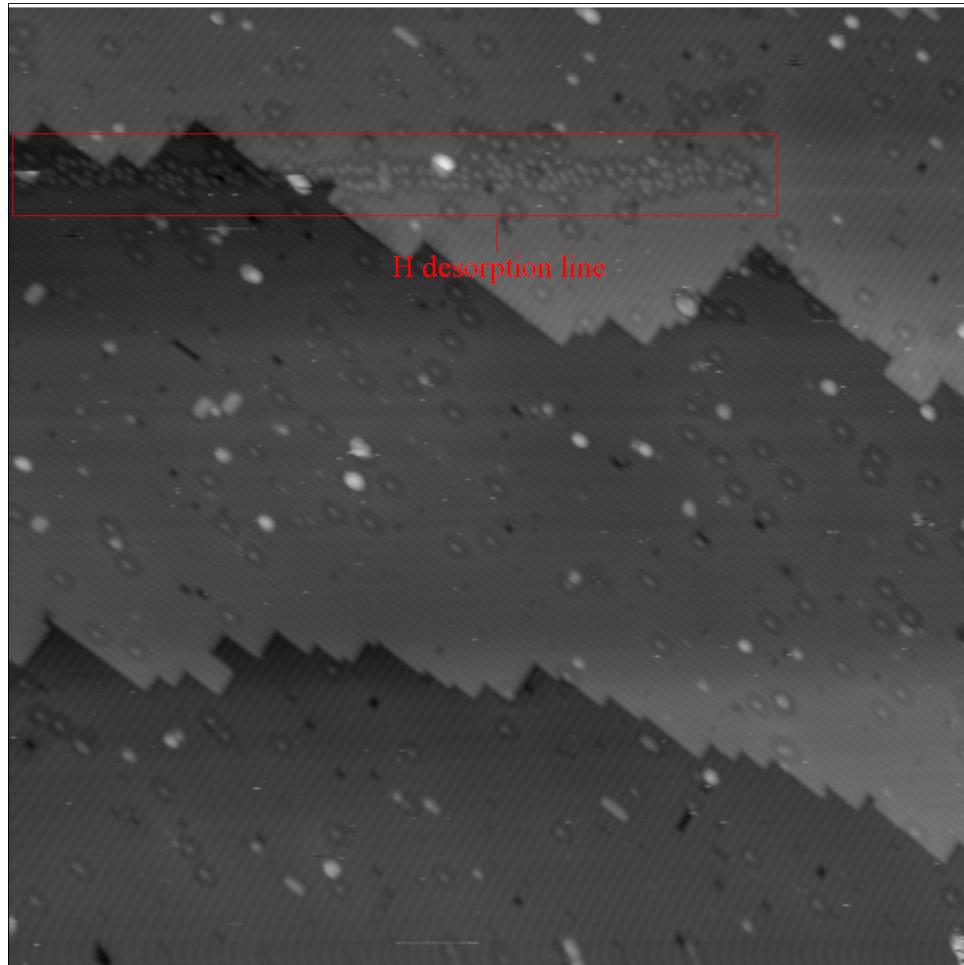
Figure 7.3: Occupied state (−3.0 V, 80 pA), 80×80 nm grayscale STM micrograph of medium B-doped, p-type H:Si(100)-(2 × 1). The row of DBs in the upper part of the image was spontaneously created by the tip.

Chapter 8

Concluding Remarks

The aim of this thesis is to provide an overview of the topics pertinent to the STM nanopatterning of H:Si(100)-(2 × 1) as it relates to the long-term endeavor of studying and fabricating computational nanodevices based on the QCA scheme.

The preceding chapters have presented the STM technique and how FIM can enhance the probability of obtaining robust and reliable scanning probes, as well as important related aspects such as the UHV technique and the components of the apparatus employed. A description of the properties of silicon crystals, their surface reconstructions and the changes they undergo when hydrogen-terminated has also been laid out together with the known mechanisms whereby hydrogen desorption can occur in STM. Additionally, calculations involving finite element analysis and numerical solutions to Morse-like potentials have been carried out to ascertain the effect of tip induced fields on the Si-H bond and thus on its dissociation mechanism.

In the course of this study initial attempts have been made at dangling bond creation on H:Si(100)-(2 × 1) using STM tips the apex structures of which were investigated/modified in the FIM in order to test the experimental setup. It remains for subsequent investigators to pursue these techniques with a view to firmly establishing procedures for routinely obtaining reliable scanning tips in order to fabricate and study the properties of atomic quantum cellular automata and thus pave the way for proof-of-concept implementations of novel computational architectures.

Bibliography

[1] C. S. Lent and P. D. Tougaw. A device architecture for computing with quantum dots. *Proceedings of the IEEE*, 85(4):541–557, apr 1997.

[2] M. B. Haider, J. L. Pitters, G. A. DiLabio, L. Livadaru, J. Y. Mutus, and R. A. Wolkow. Controlled coupling and occupation of silicon atomic quantum dots at room temperature. *Phys. Rev. Lett.*, 102(4):46805, 2009.

[3] C. Bai. *Scanning tunneling microscopy and its applications*, volume 32. Springer Verlag, 2000.

[4] http://www.chem.ufl.edu/~itl/2045_s99/lectures/lec_10.html, June 2011.

[5] Mahboubeh Hortamani. Theory of Adsorption, Diffusion and Spinpolarization of Mn on Si(001) and Si(111) Substrates. Master's thesis, Freie Universität Berlin, Berlin, Germany, 2006.

[6] Hanne. Neergaard Waltenburg and John T. Yates. Surface Chemistry of Silicon. *Chemical Reviews*, 95(5):1589–1673, 1995.

[7] J. J. Boland. Role of bond-strain in the chemistry of hydrogen on the Si(100) surface. *Surface science*, 261(1-3):17–28, 1992.

[8] T. C. Shen and P. Avouris. Electron stimulated desorption induced by the scanning tunneling microscope. *Surface Science*, 390(1-3):35–44, 1997.

[9] R. Jaquet and W. H. Miller. Quantum mechanical rate constants via path integrals: diffusion of hydrogen atoms on a tungsten (100) surface. *The Journal of Physical Chemistry*, 89(11):2139–2144, 1985.

[10] Anne-Sophie Lucier. Preparation and Characterization of Tungsten Tips Suitable for Molecular Electronics Studies. Master's thesis, McGill University, Montréal, Québec, 2004.

[11] J. K. Trolan, J. P. Barbour, E. E. Martin, and W. P. Dyke. Electron emission from a lattice step on clean tungsten. *Phys. Rev.*, 100(6):1646–1649, Dec 1955.

[12] T. T. Tsong. *Atom-Probe Field Ion Microscopy*, volume 1. Cambridge University Press, Cambridge, UK, 1990.

[13] T. T. Tsong. Field ion image formation. *Surface Science*, 70(1):211–233, 1978.

[14] M. Rezeq, J. Pitters, and R. Wolkow. Tungsten nanotip fabrication by spatially controlled field-assisted reaction with nitrogen. *The Journal of Chemical Physics*, 124:204716, 2006.

[15] http://www.nims.go.jp/apfim/gif/FIMschematic.gif, June 2011.

[16] R. A. Wolkow. Controlled Molecular Adsorption on Silicon: Laying a Foundation for Molecular Devices. *Annual Review of Physical Chemistry*, 50(1):413–441, 1999.

[17] W. Porod. Quantum-dot Devices and Quantum-dot Cellular Automata. *Journal of the Franklin Institute*, 334(5-6):1147–1175, 1997. Visions of Nonlinear Mechanics in the 21st Century.

[18] P. M. Albrecht, L. B. Ruppalt, and J. Lyding. UHV-STM Nanofabrication on Silicon. In *Scanning Probe Microscopy - Electrical and Electromechanical Phenomena at the Nanoscale*, volume 2. Springer, 2007.

[19] G. Binnig, H. Rohrer, Ch. Gerber, and E. Weibel. 7×7 reconstruction on si(111) resolved in real space. *Phys. Rev. Lett.*, 50(2):120–123, Jan 1983.

[20] R. M. Tromp, R. J. Hamers, and J. E. Demuth. Si(001) dimer structure observed with scanning tunneling microscopy. *Phys. Rev. Lett.*, 55(12):1303–1306, Sep 1985.

[21] R. A. Wolkow. A variable temperature scanning tunneling microscope for use in ultrahigh vacuum. *Rev. Sci. Instrum.*, 63(9):4049–4052, May 1992.

[22] J. W. Lyding, T. C. Shen, J. S. Hubacek, J. R. Tucker, and G. C. Abeln. Nanoscale patterning and oxidation of H-passivated Si(100)-2 $\times$ 1 surfaces with an ultrahigh vacuum scanning tunneling microscope. *Applied Physics Letters*, 64(15):2010–2012, 1994.

[23] M. A. Walsh and M. C. Hersam. Atomic-scale templates patterned by ultrahigh vacuum scanning tunneling microscopy on silicon. *Annual Review of Physical Chemistry*, 60:193–216, 2009.

[24] G. Binnig, H. Rohrer, Ch. Gerber, and E. Weibel. Tunneling through a controllable vacuum gap. *Phys. Appl. Lett.*, 40(2):178–180, 1982.

[25] Gerd Binnig and Heinrich Röhrer. Scanning tunneling microscopy - from birth to adolescence. In Tore Frängsmyr and Gösta Ekspång, editors, *Nobel Lectures, Physics 1981-1990*, pages 389–400. World Scientific Publishing Co., Singapore, 1993.

[26] W. A. Thompson and S. F. Hanrahan. Thermal drive apparatus for direct vacuum tunneling experiments. *Review of Scientific Instruments*, 47:1303, 1976.

[27] R. Young, J. Ward, and F. Scire. The topografiner: an instrument for measuring surface microtopography. *Review of Scientific Instruments*, 43(7):999–1011, 1972.

[28] C. J. Chen. *Introduction to scanning tunneling microscopy*. Oxford University Press, USA, 1993.

[29] K. W. Hipps. Scanning Tunneling Spectroscopy - A Chapter in "Handbook of Applied Solid State Spectroscopy". `www.wsu.edu/~hipps/pdf_files/specchapteronline.pdf`, May 2011.

[30] P. Niedermann, R. Emch, and P. Descouts. Simple piezoelectric translation device. *Review of Scientific Instruments*, 59(2):368–369, 1988.

[31] A. R. Smith, S. Gwo, and C. K. Shih. A new high-resolution two-dimensional micropositioning device for scanning probe microscopy applications. *Review of Scientific Instruments*, 65(10):3216–3219, 1994.

[32] P. K. Hansma and Tersoff J. Scanning tunneling microscopy. *J. Appl. Phys.*, 61:R1–R24, 1986.

[33] A. D. Gottlieb and L. Wesoloski. Bardeen's tunnelling theory as applied to scanning tunnelling microscopy: a technical guide to the traditional interpretation. *Nanotechnology*, 17(8):R57–R65, 2006.

[34] J. Tersoff. Anomalous Corrugations in Scanning Tunneling Microscopy: Imaging of Individual States. *Phys. Rev. Lett.*, 57(4):440–443, Jul 1986.

[35] N. D. Lang, A. Yacoby, and Y. Imry. Theory of a single-atom point source for electrons. *Phys. Rev. Lett.*, 63(14):1499–1502, Oct 1989.

[36] H. M. Zhang, J. B. Gustafsson, and L. S. O. Johansson. Surface atomic structure of Ag/Si(111)-$\sqrt{3} \times \sqrt{3}$. *Phys. Rev. B*, 74(20):201304, Nov 2006.

[37] J. E. Demuth, R. J. Hamers, R. M. Tromp, and M. E. Welland. . *IBM J. Res. Dev.*, 30:396, 1986.

[38] A. N. Saxena. *Invention of integrated circuits: untold important facts*. World Scientific Pub Co Inc, 2009.

[39] J. B. Pendry. *Low energy electron diffraction: the theory and its application to determination of surface structure*. Academic Press, 1974.

[40] D. Haneman. Surfaces of silicon. *Rep. Prog. Phys.*, 50:1045–1086, 1987.

[41] R. E. Schlier and H. E. Farnsworth. Structure and adsorption characteristics of clean surfaces of germanium and silicon. *The Journal of Chemical Physics*, 30:917, 1959.

[42] R. J. Hamers, R. M. Tromp, and J. E. Demuth. Scanning tunneling microscopy of Si(001). *Phys. Rev. B*, 34(8):5343–5357, Oct 1986.

[43] J. A. Kubby and J. J. Boland. Scanning tunneling microscopy of semiconductor surfaces. *Surface science reports*, 26(3-6):61–204, 1996.

[44] C. Kittel and P. McEuen. *Introduction to solid state physics*, volume 4. Wiley New York, 1986.

[45] J. A. Appelbaum, G. A. Baraff, and D. R. Hamann. Si(100) surface reconstruction: Spectroscopic selection of a structural model. *Phys. Rev. Lett.*, 35(11):729–732, Sep 1975.

[46] J. A. Appelbaum, G. A. Baraff, and D. R. Hamann. The Si(100) surface. III. Surface reconstruction. *Physical Review B*, 14(2):588, 1976.

[47] J. A. Appelbaum, G. A. Baraff, and D. R. Hamann. The Si(100) surface - further studies of the pairing model. *Physical Review B*, 15(4):2408–2412, 1977.

[48] J. A. Appelbaum and D. R. Hamann. Theory of reconstruction-induced subsurface strain - application to Si(100). *Surface Science*, 74(1):21–33, 1978.

[49] D. J. Chadi. Atomic and electronic structures of reconstructed Si(100) surfaces. *Phys. Rev. Lett.*, 43(1):43–47, 1979.

[50] R. A. Wolkow. Direct observation of an increase in buckled dimers on Si(001) at low temperature. *Phys. Rev. Lett.*, 68(17):2636–2639, Apr 1992.

[51] K. Sagisaka, D. Fujita, and G. Kido. Phase Manipulation between c (4 $\times$ 2) and p (2 $\times$ 2) on the Si(100) Surface at 4.2 K. *Phys. Rev. Lett.*, 91(14):146103, 2003.

[52] G. S. Hwang. A channel for dimer flipping on the Si(001) surface. *Surface science*, 465(3):L789–L793, 2000.

[53] A. Ramstad, G. Brocks, and P. J. Kelly. Theoretical study of the Si(100) surface reconstruction. *Physical Review B*, 51(20):14504, 1995.

[54] J. E. Northrup and M. L. Cohen. Reconstruction Mechanism and Surface-State Dispersion for Si(111)-(2 $\times$ 1). *Phys. Rev. Lett.*, 49(18):1349–1352, 1982.

[55] K. Takayanagi, Y. Tanishiro, M. Takahashi, and S. Takahashi. Structural analysis of Si(111)-7 $\times$ 7 by UHV-transmission electron diffraction and microscopy. *J. Vac. Sci. Technol. A*, 3(3):1502–1506, 1985.

[56] H. Ibach and J. E. Rowe. Hydrogen adsorption and surface structures of silicon. *Surface Science*, 43(2):481–492, 1974.

[57] T. Sakurai and H. D. Hagstrum. Interplay of the monohydride phase and a newly discovered dihydride phase in chemisorption of H on Si(100)-2 × 1. *Physical Review B*, 14(4):1593, 1976.

[58] Y. J. Chabal and K. Raghavachari. New ordered structure for the H-saturated Si(100) surface: the (3 × 1) phase. *Phys. Rev. Lett.*, 54(10):1055–1058, 1985.

[59] I. W. Lyo and Ph. Avouris. Field-induced nanometer-to atomic-scale manipulation of silicon surfaces with the STM. *Science*, 253(5016):173, 1991.

[60] M. Aono, A Kobayashi, F. Grey, H. Uchida, and D-H. Huang. Tip-Sample Interactions in the Scanning Tunneling Microscope for Atomic-Scale Structure Fabrication. *Japanese Journal of Applied Physics*, 32(Part 1, No. 3B):1470–1477, 1993.

[61] R. S. Becker, G. S. Higashi, Y. J. Chabal, and A. J. Becker. Atomic-scale conversion of clean si(111):h-1 × 1 to si(111)-2 × 1 by electron-stimulated desorption. *Phys. Rev. Lett.*, 65(15):1917–1920, Oct 1990.

[62] J. J. Boland. The importance of structure and bonding in semiconductor surface chemistry: hydrogen on the Si(111)-7 × 7 surface. *Surface Science*, 244(1-2):1 – 14, 1991.

[63] D. H. Huang and Y. Yamamoto. Atomic Manipulation of Hydrogen on Hydrogen-Terminated Silicon Surfaces with Scanning Tunneling Microscope. *Atomic Force Microscopy/Scanning Tunneling Microscopy 3*, pages 49–64, 2002.

[64] T. C. Shen, C. Wang, G. C. Abeln, J. R. Tucker, J. W. Lyding, P. Avouris, and R. E. Walkup. Atomic-scale desorption through electronic and vibrational excitation mechanisms. *Science*, 268(5217):1590, 1995.

[65] E. T. Foley, A. F. Kam, J. W. Lyding, and Ph. Avouris. Cryogenic UHV-STM Study of Hydrogen and Deuterium Desorption from Si(100). *Phys. Rev. Lett.*, 80(6):1336–1339, Feb 1998.

[66] P. Guyot-Sionnest, P. Dumas, Y. J. Chabal, and G. S. Higashi. Lifetime of an adsorbate-substrate vibration: H on Si(111). *Phys. Rev. Lett.*, 64(18):2156–2159, Apr 1990.

[67] K. Stokbro, C. Thirstrup, M. Sakurai, U. Quaade, B. Y. K. Hu, F. Perez-Murano, and F. Grey. STM-induced hydrogen desorption via a hole resonance. *Phys. Rev. Lett.*, 80(12):2618–2621, 1998.

[68] C. Thirstrup, M. Sakurai, T. Nakayama, and K. Stokbro. Temperature suppression of STM-induced desorption of hydrogen on Si(100) surfaces. *Surface Science*, 424(2-3):L329 – L334, 1999.

[69] L. Soukiassian, A. J. Mayne, M. Carbone, and G. Dujardin. Atomic-scale desorption of H atoms from the Si(100)-2 × 1: H surface: Inelastic electron interactions. *Phys. Rev. B*, 68:035303–035307, 2003.

[70] T. T. Tsong. Effects of an electric field in atomic manipulations. *Phys. Rev. B*, 44(24):13703–13710, Dec 1991.

[71] I-H. Tan, G. L. Snider, L. D. Chang, and E. L. Hu. A self-consistent solution of Schrödinger–Poisson equations using a nonuniform mesh. *J. Appl. Phys.*, 68(8):4071–4076, 1990.

[72] D Kohen, J. C. Tully, and F. H. Stillinger. Modeling the interaction of hydrogen with silicon surfaces. *Surface Science*, 397(1-3):225–236, 1998.

[73] G. Lucovsky, R. J. Nemanich, J. Bernholc, J. Whitten, C. Wang, B. Davidson, M. Williams, D. Lee, C. Bjorkman, and Z. Jing. Fundamental Studies of Defect Generation in Amorphous Silicon Alloys Grown by Remote Plasma-Enhanced Chemical-Vapor Deposition - Annual Subcontract Report, 1 September 1990 – 31 January 1991. Technical Report NREL/TP–451-4852, North Carolina State University, Raleigh, North Carolina, January 1993.

[74] H. C. Akpati, P. Nordlander, L. Lou, and Ph. Avouris. The effects of an external electric field on the adatom-surface bond: H and Al adsorbed on Si(111) . *Surface Science*, 372(1-3):9–20, 1997.

[75] B. N. J. Persson and Ph. Avouris. The effects of the electric field in the STM on excitation localization. Implications for local bond breaking. *Chemical Physics Letters*, 242(4-5):483–489, 1995.

[76] D. N. Seidman. Perspective: From field-ion microscopy of single atoms to atom-probe tomography: A journey:Atom-probe tomography[Rev. Sci. Instrum.[bold 78], 031101 (2007)]. *Review of Scientific Instruments*, 78:030901, 2007.

[77] A. J. Melmed. Recollections of Erwin Müller's laboratory: the development of FIM (1951-1956). *Applied Surface Science*, 94:17–25, 1996.

[78] J. J. Hren and S. Ranganathan. *Field-Ion Microscopy*. Plenum Press, USA, 1968.

[79] C. Kleint. On the early history of field emission including attempts of tunneling spectroscopy. *Progress in Surface Science*, 42(1-4):101–115, 1993.

[80] Vu Thien Binh, N. Garcia, and S.T. Purcell. Electron Field Emission from Atom-Sources: Fabrication, Properties, and Applications of Nanotips. volume 95 of *Advances in Imaging and Electron Physics*, pages 63 – 82, 82a, 82b, 83–153. Elsevier, 1996.

[81] T. T. Tsong. Measurement of the Polarizabilities and Field Evaporation Rates of Individual Tungsten Atoms. *The Journal of Chemical Physics*, 54:4205, 1971.

[82] M. H. Hablanian. *High-vacuum technology: a practical guide*. CRC, 1997.

[83] G. L. Weissler. Methods of experimental physics. Volume 14. Vacuum physics and technology. 1979.

[84] P. A. Redhead. History of ultrahigh vacuum pressure measurements. *Journal of Vacuum Science & Technology A: Vacuum, Surfaces, and Films*, 12(4):904–914, 1994.

[85] J. P. Ibe, P. P. Bey Jr., S. L. Brandow, R. A. Brizzolara, N. A. Burnham, D. P. DiLella, K. P. Lee, C. R. K. Marrian, and R. J. Colton. On the electrochemical etching of tips for scanning tunneling microscopy. *Journal of Vacuum Science & Technology A: Vacuum, Surfaces, and Films*, 8(4):3570–3575, 1990.

[86] M. C. Hersam, N. P. Guisinger, and J. W. Lyding. Isolating, imaging, and electrically characterizing individual organic molecules on the Si(100) surface with the scanning tunneling microscope. *The 46th international symposium of the american vacuum society*, 18(4):1349–1353, 2000.